

FREE-SPACE SWITCHING FOR OPTICAL FIBRE NETWORKS

A dissertation submitted for the
degree of Doctor of Philosophy
at the University of Cambridge



Stephen Thomas Warr
Christ's College, Cambridge

July 1996

Declaration

This dissertation contains the results of research undertaken by the author between October 1992 and December 1995 at the Engineering Department of Cambridge University. Except for the experiment described in chapter 4 (pages 64-73) which is the result of a collaboration between the author and Mr M.C. Parker, no part of this dissertation is the result of work done in collaboration with others. The contents have not been submitted, in whole or in part, for any other University degree or diploma.

Stephen Thomas Warr
Cambridge, July 1996

Contents

CHAPTER 1	
Introduction	1
CHAPTER 2	
Dynamic Holography with Ferroelectric Liquid Crystals	6
2.1 Free-Space Diffraction-Propagation Theory	7
2.1.1 Coherent sources and Gaussian fields	8
2.2 Holographic Replay	10
2.2.1 Optical transformation properties of a positive lens	11
2.2.2 The Fourier flat-phase condition	13
2.3 Ferroelectric Liquid Crystal Spatial Light Modulators	13
2.3.1 Ferroelectric molecular dynamics	14
2.3.2 Surface-stabilised FLC pixel structures	17
2.3.3 Backplane SLM pixel circuitry	19
2.4 Computer Generated Holograms	20
2.4.1 Binary phase-only modulation with ferroelectric liquid crystals	20
CHAPTER 3	
The Polarisation Insensitive One to Any Optical Interconnect	24
3.1 Polarisation Insensitive Ferroelectric Operation	24
3.1.1 Polarisation analysis	25
3.1.2 Experimental verification of polarisation independence	29

3.2	The One-to-Any Single-Mode Fibre Switch	32
3.2.1	Experimental 1-to-2 fibre switch	33
3.2.2	Experimental 1-to-15 fibre switch	34
3.3	Diffraction Efficiency Limitations of FLC Switches.....	42
3.3.1	Inversion symmetry from binary phase holograms	43
3.3.2	Effects of hologram pixellation and dead-space	44
3.4	Crosstalk	50
3.4.1	Replay phase-profiles and the overlap integral	51
3.4.2	Experimental crosstalk measurement	54
3.5	Discussion	57
CHAPTER 4		
A Holographically Tuneable Wavelength Switch for $\lambda = 1.55\mu\text{m}$		61
4.1	Diffraction WDM Components	62
4.1.1	Ferroelectric liquid crystals as dynamic gratings.....	63
4.2	The Wavelength Switch Architecture.....	64
4.2.1	Experimental wavelength switching.....	68
4.2.2	Insertion loss performance.....	73
4.3	Optical Simulation of the Wavelength Switch	74
4.4	Use of a 1-Dimensional SLM	77
4.4.1	Experimental performance of a 1-dimensional SLM.....	78
4.5	Discussion	80
CHAPTER 5		
A Single-Stage, Single-Mode Holographic Interconnect		82
5.0.1	Free-space crossbar structures	82
5.1	The Holographic Crossbar with Passive Fan-In	83
5.1.1	$1/N$ Scalability limitation	85
5.2	The Scalable Holographic Crossbar with Active Fan-In	89
5.2.1	Design and optical modelling of an experimental 8×8 crossbar	90
5.3	Microlens Arrays	94

5.3.1	Theory of GRIN lenses	95
5.3.2	Experimental characterisation of GRIN collimators	97
5.3.3	Experimental demonstration of superimposed replay fields.....	102
5.4	Discussion	105
 CHAPTER 6		
Conclusions and Future Work		108
6.1	Conclusions.....	108
6.2	Future Work	111
6.2.1	Devices	111
6.2.2	Hologram asymmetry	112
6.2.3	Systems	114
 BIBLIOGRAPHY		116
 APPENDIX A		
Associated Publications		127
 APPENDIX B		
Glossary		129

List of Figures

2.1	Optical 4- <i>f</i> Gaussian relay.	10
2.2	The conical degrees of freedom of an FLC ‘bulk’ molecule.	14
2.3	The two degrees of freedom of a surface-stabilised FLC molecule.	15
2.4	(a) Bookshelf layer structure.	16
	(b) Chevron layer structure.	16
2.5	The structure of a single transmissive SLM pixel.	18
2.6	The structure of a reflective silicon backplane SLM pixel.	18
2.7	(a) DRAM pixel modulator.	19
	(b) SRAM pixel modulator.	19
2.8	Reconfigurable diffractive optical element.	21
2.9	Orientation of polarisers for phase-only operation.	22
3.1	Polarisation insensitive ferroelectric hologram and replay.	26
3.2	(a) FLC indicatrix: state 1.	27
	(b) FLC indicatrix: state 2.	27
3.3	(a) Replay with polarisers.	31
	(b) Replay without polarisers.	31
3.4	One-to-any fibre switching experiment.	32
3.5	Microscope image of the 4x4 single-mode fibre array.	35
3.6	Single-mode fibre locations.	38
3.7	Photograph of the 1-to-15 experimental setup.	39
3.8	Normalised experimental insertion loss.	40
3.9	Hologram set for the 1-to-15 fibre switch experiment.	41
3.10	Intensity envelope across the replay diffraction-orders.	46
3.11	Theoretical bound on binary hologram efficiency.	49
3.12	Conditions for a replay spot to launch into single-mode fibre.	52

3.13	Gaussian to single-mode fibre coupling efficiencies.	53
3.14	Typical hologram replay wavefront.	53
3.15	Experimental determination of 2DX320 crosstalk performance.	55
3.16	Microscope image of a portion of the 2DX320 SLM.	57
3.17	One-to-any fibre switch: Compact 2- <i>f</i> architecture.	59
4.1	The Littrow mount passive wavelength (de)multiplexer.	63
4.2	Tuneable wavelength switching experiment.	65
4.3	Ray-trace of the principal ray through the WDM switch of figure 4.2.	66
4.4	Typical WDM switch hologram and replay.	67
4.5	(a) Wavelength response of the 2DX320, optimised for $\lambda \simeq 633\text{nm}$	69
	(b) Wavelength response of the 2DX128IR, optimised for $\lambda \simeq 1.5\mu\text{m}$	69
4.6	FLC-SLM tuning response for the experimental WDM switch.	70
4.7	Photograph of the WDM switch experimental setup.	71
4.8	Spectral characteristic of the input diode laser source.	72
4.9	Experimentally filtered output spectra.	72
4.10	(a) CODE V simulation of the exit pupil wavefront.	75
	(b) CODE V simulation of the output spot intensity profile.	75
4.11	Operating parameters for commonly used lens designs.	76
4.12	Suppression of the zero-order replay by a high-tilt FLC-SLM.	79
5.1	Dilated crossbar structure created from multiple one-to-any sub-blocks.	83
5.2	A single-pass holographic crossbar structure.	84
5.3	(a) Insertion loss scalability of the passive fan-in FLC-SLM crossbar.	87
	(b) Optimum design parameters versus number of crossbar inputs.	87
5.4	A double-pass holographic crossbar structure for single-mode fibres.	89
5.5	(a) CODE V ray-trace of an 8x8 single-mode optical crossbar at $\lambda = 1.55\mu\text{m}$	91
	(b) CODE V simulation of the worst-case exit pupil wavefront.	91
5.6	Selfoc GRIN index profile and lens geometry.	96
5.7	Mechanical drawing cross-section of the custom fibre-GRIN collimators.	98
5.8	(a) Beam profile emerging from a fibre-GRIN collimator at 25mm.	100
	(b) Beam profile in the plane of minimum beam radius at 225mm.	100
	(c) Distortion of the collimator beam profile at 300mm.	100
5.9	Evolution of the Gaussian wavefront emerging from a fibre-GRIN collimator.	101

3.13	Gaussian to single-mode fibre coupling efficiencies.	53
3.14	Typical hologram replay wavefront.	53
3.15	Experimental determination of 2DX320 crosstalk performance.	55
3.16	Microscope image of a portion of the 2DX320 SLM.	57
3.17	One-to-any fibre switch: Compact 2- <i>f</i> architecture.	59
4.1	The Littrow mount passive wavelength (de)multiplexer.	63
4.2	Tuneable wavelength switching experiment.	65
4.3	Ray-trace of the principal ray through the WDM switch of figure 4.2.	66
4.4	Typical WDM switch hologram and replay.	67
4.5	(a) Wavelength response of the 2DX320, optimised for $\lambda \simeq 633\text{nm}$	69
	(b) Wavelength response of the 2DX128IR, optimised for $\lambda \simeq 1.5\mu\text{m}$	69
4.6	FLC-SLM tuning response for the experimental WDM switch.	70
4.7	Photograph of the WDM switch experimental setup.	71
4.8	Spectral characteristic of the input diode laser source.	72
4.9	Experimentally filtered output spectra.	72
4.10	(a) CODE V simulation of the exit pupil wavefront.	75
	(b) CODE V simulation of the output spot intensity profile.	75
4.11	Operating parameters for commonly used lens designs.	76
4.12	Suppression of the zero-order replay by a high-tilt FLC-SLM.	79
5.1	Dilated crossbar structure created from multiple one-to-any sub-blocks.	83
5.2	A single-pass holographic crossbar structure.	84
5.3	(a) Insertion loss scalability of the passive fan-in FLC-SLM crossbar.	87
	(b) Optimum design parameters versus number of crossbar inputs.	87
5.4	A double-pass holographic crossbar structure for single-mode fibres.	89
5.5	(a) CODE V ray-trace of an 8x8 single-mode optical crossbar at $\lambda = 1.55\mu\text{m}$	91
	(b) CODE V simulation of the worst-case exit pupil wavefront.	91
5.6	Selfoc GRIN index profile and lens geometry.	96
5.7	Mechanical drawing cross-section of the custom fibre-GRIN collimators.	98
5.8	(a) Beam profile emerging from a fibre-GRIN collimator at 25mm.	100
	(b) Beam profile in the plane of minimum beam radius at 225mm.	100
	(c) Distortion of the collimator beam profile at 300mm.	100
5.9	Evolution of the Gaussian wavefront emerging from a fibre-GRIN collimator.	101

5.10	An experimental fibre-to-camera crossbar configuration.	102
5.11	The array of Gaussian input beams and associated sub-hologram patterns.	103
5.12	(a) Camera image of the four optically superimposed replay fields.	104
	(b) Line profiles of each replay and the corresponding diffraction-limits.	104
5.13	Required size of crossbar holograms.	106
6.1	Prototyping design for silicon backplane compatible 1-D SLM structures.	111
6.2	Typical holographic loss versus number of phase levels (no dead-space).	113
6.3	(a) Normal ferroelectric molecular orientations: Binary states.	113
	(b) Relaxed antiferroelectric molecular orientation: Third state.	113
6.4	(a) Compact tuneable wavelength filter using GRIN lenses.	115
	(b) Compact dilated crossbar using GRIN lenses.	115

Summary

The problems of point-to-point communication have essentially been solved by advances in semiconductor laser and optical fibre technologies. Direct optical signal amplification has also become possible in recent years using Erbium-doped fibres [1], and uninterrupted glass fibre lengths of over 6000km are now being installed [2]. But the technologies used for signal routing have yet to catch up with the huge potential bandwidths that optical fibres offer.

The research outlined in this dissertation relates to the optical implementation of free-space routing architectures for communication networks. These systems potentially allow hundreds or even thousands of signals to be optically routed through each other in a compact 3-dimensional volume, incurring very little crosstalk. This is achieved by the use of programmable computer-generated holograms (CGHs) displayed on a ferroelectric liquid crystal (FLC) spatial light modulator (SLM). The SLM provides fast 2-dimensional binary modulation of coherent light and acts as a dynamically reconfigurable diffraction pattern. The dissertation outlines the optical design and implementation of three such free-space switching architectures, where the SLM is used to deflect input signals to the required outputs in a bandwidth independent 'optically-transparent' manner. Experimental investigations of a broadband 1-to-15 fibre selector switch, a tuneable wavelength filter, and the initial experimental characterisation of a full N -to- M fibre crossbar switch are presented.

These transparent switches offer a more compatible approach for routing high bandwidth optical signals than existing electronic switch designs. The target applications for this FLC-SLM technology are reconfigurationally un-intensive operations involving very high optical modulation frequencies, where switch failures would be expensive. Applications include circuit-switching of broadband or wavelength-multiplexed data, and network management or restoration. The diffractive nature of CGHs makes them extremely robust in their operation and therefore well suited to the above applications. The dynamic CGH patterns used to perform the routing are shift invariant and do not fail catastrophically if individual SLM pixels stop working. The optical efficiencies and crosstalk noise rejection are only limited by the diffraction efficiencies of the CGH-SLM. Relevant theoretical efficiency limits are derived and compared with experimental measurements. Better than -30dB crosstalk rejection is demonstrated by the 1-to-15 switch, and measurements suggest that less than 6dB insertion loss will be possible in future iterations, even with considerably more fibre ports.

Previous FLC-SLM optical systems have not fully addressed the requirements for optical transparency. In particular, they generally exhibit strong polarisation dependence and encounter problems when re-entering the fibre network from free-space. The switch configurations presented in this dissertation have been enabled by an analysis in chapter 3 which predicts that FLC-CGHs can be used as polarisation insensitive components. In addition, attention is paid in the design of free-space components to determining and meeting the demanding optical field matching requirements of single-mode fibre outputs. The success of the techniques used are experimentally demonstrated as space- and wavelength-switches, and all of the architectures have the property of full reciprocity.

Acknowledgements

The completion of my dissertation would have been impossible, and my time at Cambridge far less enjoyable, without the help and advice of family, colleagues and friends.

I would especially like to thank Tim for general abuse, criticism, more abuse and an almost memorable drunken discussion at Herriot-Watt; Malcolm for his conversational skills in the back of taxis; Aaron for calming the taxi driver; Rob D. for always choosing the same restaurant; Mark H. for his ice-cream; Polina for her advice and the slice of apple crumble; Alex for Monday evenings; Richard G. for dumping me in it with *Marriage of Figaro*; Richard B., Adam W., Celia and Jenny for all the other times at the theatre; James M. for his heart-stopping driving along tiny country roads with *The Orb* at full volume; Russell, Adrian, Steve and Mick for their excellent technical support; EPSRC, OST and POETS for providing resources; Paul Coghlan, Mike Parker, Ian Springle, Dave Kozlowski, Adam Cohen, James Collington, Eddie Pratt, Mark Dames, Tony Davey, Adrian Travis, Steve Latham, Julie Snushall, Martin Birch, Malcolm Naylor, Henry White, F. Zachariasse, Vincent, and anyone else I've forgotten for their help, friendship, or for just not asking too often when I was going to finish.

Special thanks also to Bill Crossland with the help of Caryn Wilkinson for leading the group and providing incredible resources in my chosen field of research, and to Rob Mears my supervisor for his help and support; his occasional but crucial advice; his quantum behaviour near coffee machines; and for never quite making it to the Hot Pot restaurant. Finally, the list wouldn't be complete without the biggest thankyou and a hug to Tania whose love and encouragement has kept me (debatably?) sane during my graduate years.

CHAPTER 1

Introduction

The field of global telecommunications continues to expand at a phenomenal rate and looks set to become the world's largest industry. The arrival of multimedia systems and the rapid integration of the world-wide web into everyday life means that there is an ever increasing demand for bandwidth, and an increased reliance on optoelectronic networks and devices. Research advances in optoelectronics have enabled technologies as diverse as laser printing and compact disc players, as well as enhancing the global telephony and computer networks.

Optical fibres have effectively replaced wires as the information transmission medium, and many countries are installing substantial numbers of single-mode fibre telecommunication links. These fibres are characterised by their high bandwidth capacity and by their low signal dispersion. However, the switching technology used to route these optical signals has remained firmly embedded in the electronic domain. To avoid long 'on-chip' transmission distances, current electronic switching methods concentrate on the use of time-domain routing, involving the allocation and servicing of each input during a particular time slot. But the speed and bandwidth capacity of electronic switches are ultimately limited by the signal skewing effects of capacitive propagation delays. These 'RC' delays, and their associated power dissipation and crosstalk effects, arise because of the need for physical electronic wiring between the switch input and output ports. Light photons do not suffer any equivalent constraints and there are clearly applications where an all-optical or an optically-assisted routing approach could ease the load placed upon electronic switches.

Light operates in an inherently parallel manner and therefore allows high modulation bandwidths to be achieved in comparison to similar electronic architectures. Present optical technology can be used to implement forms of circuit-switched networks, where traffic is

routed from terminal to terminal in the optical domain, regardless of the modulation format. The literature reveals two distinct optical switching approaches. Solid-state optical devices often attempt to mimic some of the switching functions performed by electronic networks; free-space optical devices instead attempt to obtain a much greater advantage over comparable electronic architectures by using the full 3-dimensional capability of light. Solid-state methods include a fibre backplane with D-fibre coupler taps [3], gated optical amplifier arrays [4], electro-optic and semiconductor waveguide matrix switches [5–8], acousto-optic filters [9], and non-linear fibre loops for time-multiplexed switching [10]. Many of these devices are built onto planar waveguide substrates and they therefore still require optical ‘wiring’. The alternative free-space switching is performed simply by ‘pointing’ the input sources of light directly at the output fibres or detectors across a 3-dimensional volume.

Many of the major telecommunication operators are investigating the free-space optical approach. AT&T Bell Laboratories have spent huge resources advancing their FET-SEED technology for optically interconnecting planes of GaAs logic containing monolithically integrated optical modulators and receivers [11,12]. British Telecom have investigated space and wavelength switches as part of the multi-dimensional optical network project (MONET) [13], and Japan’s NTT are demonstrating switches based on liquid crystal displays [14].

Liquid crystal devices are of particular interest because the market for commercial flat-panel displays has driven their development as an emerging mature technology. Ferroelectric liquid crystal (FLC) mixtures are the best suited for optical processing and interconnection applications because of their fast frame rates and large electro-optic modulation. FLC devices are less well developed than the more common display-oriented nematic liquid crystal mixtures. Thus only a handful of FLC spatial light modulators (SLMs) are commercially available, but new devices using silicon VLSI technology for control and electronic interfacing [15–17] are rapidly emerging and these are well suited to free-space interconnection techniques.

- **Chapter 2** outlines the basic implementation of FLC-SLMs as reconfigurable diffractive phase elements, optically arranged to route coherent beams of light across a free-space interconnect. The principle of operation of all diffractive optical switches is to deflect as much signal power as possible from the inputs to the outputs. Suitable phase patterns for achieving arbitrary routing are usually complex grating structures, constrained to only two phase states by the FLC operation. The computer design and

implementation of these binary holograms is well documented (e.g., [18]) and is not presented in any detail here. However, it is important to understand exactly how each holographic recording shapes and deflects the profile of the coherent optical signal passing through it. The phase patterns form holographic replay images, and the relationship between each hologram and its replay is shown to be that of a 2-dimensional spatial Fourier transform with a coordinate origin which coincides with the optic axis of a transform lens. Each Fourier plane hologram is therefore shift invariant and by changing between different display frames, the FLC-SLM may be used to dynamically route a single optical input to any one of many outputs. Once the switch has been configured, the optical data rate is unaffected by the FLC-SLM and is only limited by the modulation speed of the network sources.

- **Chapter 3** describes a method of achieving polarisation independent operation of FLC-SLMs without any adverse effects on the simplicity or performance of the optical system. The result is crucial to the implementation of FLC-SLMs as fibre interconnects and routers because most optical networks do not have any kind of polarisation control. This places dynamic holographic switches in a completely new light and may potentially lead to a large set of previously unknown architectural designs. The polarisation insensitive result is verified experimentally in the chapter using computer-generated holograms displayed on a transmissive FLC device. Building on this foundation, the chapter then describes the design and experimental implementation of an optically transparent dynamic 1-to-15 single-mode fibre router. This is the largest free-space polarisation independent interconnect ever built and it is a significant step towards demonstrating the feasibility of highly-parallel FLC architectures.

Optical switches can be characterised by their noise rejection performance and by the loss penalty associated with sending light through them. FLC-SLMs exhibit excellent noise rejection, but current devices are limited to fairly large insertion losses. The continued development of FLC-SLM technology means that the gap between potential performance and actual experimental measurements is gradually closing, and the remainder of the chapter investigates the theoretical diffraction efficiency limits of all types of FLC-SLM interconnect.

- **Chapter 4** outlines how the normally broadband transmission of FLC-SLMs may be refined to a degree where they are potentially useful in wavelength-division-multiplexed (WDM) networks for wavelength routing and selection. WDM networks provide a

means for more efficient utilisation of optical fibre bandwidths, and although there is vigorous debate on how best to implement WDM, it is generally accepted that optically transparent components will be essential for routing and network configuration. This chapter investigates the design and experimental performance of an FLC-SLM tuneable filter that is capable of isolating a single wavelength channel from a multiplexed stream of wavelength channels. The experiment was primarily intended as a proof-of-principle demonstration to show the advantages of holographic tuning, and to demonstrate for the first time that FLC-SLMs can be successfully operated in the $1.55\mu\text{m}$ telecommunications wavelength band.

The experimental switch matches theoretical predictions by achieving a wavelength selectivity and tuning step of a few nanometres, but is flawed by a very high insertion loss penalty. The chapter describes various enhancements that would reduce the loss to an acceptable level, particularly concentrating on the optimisation of the FLC-SLM using a 1-dimensional pixel array. The chapter also discusses the problems of maintaining aberration-free (single-moded) operation, and highlights the need for careful consideration of the optical design before attempting to construct large interconnection architectures.

- **Chapter 5** describes the design of a single-mode FLC-SLM crossbar architecture for interconnecting large arrays of input and output fibres. An array of dynamic holograms can be used to achieve an arbitrary routing pattern between N inputs and M outputs, and two methods of re-entering the fibre network are considered. Passive fan-in is shown to be limited in its application by an approximately $1/N$ insertion loss relationship, and a \sqrt{N} interconnect volume growth. A new active fan-in architecture is proposed which has a higher initial diffraction loss, but which is shown to have no interconnect-density scaling limitations.

Optical simulation software is used to design a near aberration-free proof-of-principle 8×8 crossbar using active fan-in at $\lambda = 1.55\mu\text{m}$. The design uses two custom optical components: a spherical concave mirror, and an array of micro-lens fibre collimators. The collimators are an essential technology for future free-space switching devices. Graded-index rod lenses with diameters of a few millimetres are suggested as the best means for implementing them, given that the supportable crossbar size depends upon the number of hologram routing pixels that are illuminated per input fibre. The design, iteration and initial experimental characterisation of mechanically rigid graded-index fibre collimators is outlined, and the chapter shows that these components are

suitable for the low-loss 8x8 crossbar prototype. The modular nature of the fibre-lens array assemblies makes them very well suited to the construction of future large-scale diffractive switches with potentially thousands of inputs and outputs.

- **Chapter 6** is a summary of the work presented in this dissertation, and it discusses future prospects and improvements for FLC-SLM fibre interconnects.

CHAPTER 2

Dynamic Holography with Ferroelectric Liquid Crystals

Any device capable of dynamically modulating a beam of light in one- or more usually two-dimensions, may be referred to as a 'spatial light modulator' (SLM). Televisions are SLMs in this broadest definition of the term, because they produce a rapidly updated series of images. However TVs and other cathode ray-tube devices simply radiate light from the screen by phosphor emission and they therefore produce incoherent images. Although some useful optical processing operations can be implemented by systems that use only partially coherent or extended light sources [19], there are severe drawbacks with this approach because of the accumulation of a non-zero optical mean and because of poor noise performance. These result from the optical phase indeterminacy of incoherent light, such that only the intensity of each image is meaningful.

The most useful types of SLMs are non-emissive devices capable of altering the intensity and/or phase of the wavefronts passing through them. The obvious examples of intensity modulators are the liquid crystal displays found on modern laptop computers, in which SLM pixels locally modulate the intensity of a diffuse (incoherent) light source. However, many systems which manipulate optical beams in a more specialised fashion, for example to perform some kind of image filtering or correlation [20, 21], rely on the generation and use of coherent light.

When illuminated by a coherent source, non-emissive SLMs are not only limited to image formation but may instead be configured as programmable diffractive optical elements, e.g., tuneable gratings. In particular, they may also be used to display complex 2-dimensional computer generated holograms (CGHs) [22] and hence be used to dynamically diffract beams of light into arbitrary positions or patterns. In addition, a CGH-SLM device which only

CHAPTER 2

Dynamic Holography with Ferroelectric Liquid Crystals

Any device capable of dynamically modulating a beam of light in one- or more usually two-dimensions, may be referred to as a 'spatial light modulator' (SLM). Televisions are SLMs in this broadest definition of the term, because they produce a rapidly updated series of images. However TVs and other cathode ray-tube devices simply radiate light from the screen by phosphor emission and they therefore produce incoherent images. Although some useful optical processing operations can be implemented by systems that use only partially coherent or extended light sources [19], there are severe drawbacks with this approach because of the accumulation of a non-zero optical mean and because of poor noise performance. These result from the optical phase indeterminacy of incoherent light, such that only the intensity of each image is meaningful.

The most useful types of SLMs are non-emissive devices capable of altering the intensity and/or phase of the wavefronts passing through them. The obvious examples of intensity modulators are the liquid crystal displays found on modern laptop computers, in which SLM pixels locally modulate the intensity of a diffuse (incoherent) light source. However, many systems which manipulate optical beams in a more specialised fashion, for example to perform some kind of image filtering or correlation [20, 21], rely on the generation and use of coherent light.

When illuminated by a coherent source, non-emissive SLMs are not only limited to image formation but may instead be configured as programmable diffractive optical elements, e.g., tuneable gratings. In particular, they may also be used to display complex 2-dimensional computer generated holograms (CGHs) [22] and hence be used to dynamically diffract beams of light into arbitrary positions or patterns. In addition, a CGH-SLM device which only

modulates the phase of the wavefronts passing through it, does not have to block out light in order to form new diffractive image planes. It is therefore inherently more efficient than an intensity-only display and is potentially well suited to situations where the available optical power level is fairly small.

SLMs typically consist of an array of individually controllable pixels. A number of suitable technologies are currently available for displaying CGH diffraction patterns. Acousto-optic [23,24] and magnetically operated SLMs [25,26] offer fast frame speeds but are expensive and difficult to manufacture. These devices tend to have limited numbers of pixels and suffer from low production yields. Alternatively, recent silicon micro-machining technology has led to the development of SLMs based on deformable mirrors [27,28]. However, yields can again be expected to be low and the mechanical nature of these devices leads to a lot of unused space on the device surface and hence relatively poor optical effects. At present, the cheapest, most promising and accessible route to CGH-SLMs are liquid crystal devices of which there are two main categories. Twisted nematic LC-filled SLMs [29] are found in watches, calculators and laptop computer displays. These devices produce continuous greyscale modulation but can only operate up to video frames rates, i.e., about 24 frames per second. Ferroelectric liquid crystal SLMs [30] are limited to binary modulation states when driven in their usual mode of operation, but they potentially operate much faster than nematics, with material switching speeds of the order of $10\mu\text{s}$. They therefore represent the best available compromise between reliability and speed, and they can also be readily configured as phase- or as intensity-modulators.

2.1 Free-Space Diffraction-Propagation Theory

The optical properties of coherent systems are described by rigorous diffraction-propagation theory. However the exact theory of diffraction is highly complex and in order to actually solve the appropriate differential equations, it is usually necessary to make a number of assumptions about the nature of the electromagnetic optical fields involved and the medium in which they are propagating. A formal approach to diffraction theory may be found in books by Goodman [31] or Siegman [32], but in order to introduce free-space propagation of coherent light and the operation and use of CGH-SLMs, some of the basic principles are presented here. Of particular interest are the properties of coherent Gaussian beams and the complex-valued spatial Fourier transform theory of computer generated holograms.

2.1.1 Coherent sources and Gaussian fields

Coherent optical fields in isotropic or nearly isotropic dielectric media such as air or glass, obey Laplace's scalar wave equation:

$$\left(\nabla^2 + k^2\right)\tilde{\epsilon}(x, y, z, t) = 0 \quad (2.1)$$

where the 4-dimensional optical field distribution, $\tilde{\epsilon}(x, y, z, t)$, is a time-harmonic electromagnetic travelling wave. The spatial magnitude and phase of the wavefront may be described by a complex field amplitude distribution, $\tilde{E}(x, y, z)$:

$$\tilde{\epsilon}(x, y, z, t) = \text{Re}\left\{\tilde{E}(x, y, z) \exp\left[j(\omega t - kz)\right]\right\} \quad (2.2)$$

$$\text{and } \tilde{E}(x, y, z) = |\tilde{E}(x, y, z)| \exp\left[j(\phi(x, y, z))\right]$$

where $\phi(x, y, z)$ is the wavefront phase profile and $k (= \frac{2\pi}{\lambda} = \frac{\omega}{c})$ is the wavenumber for wavelength λ . In 1690, Huygen was the first to suggest that propagation of light as described by the scalar wave equation (2.1), may be considered as a process of continuous diffraction. Thus in general, the profile of an optical beam will alter as it propagates. However there do exist a set of stationary solutions to (2.1) which have optical field profiles which change in size as they propagate in free-space along the z -axis, but have distribution patterns which remain unaltered.

These 'eigenmodes' can be conveniently described by the orthogonal Hermite-Gaussian polynomials [32]. Only the lowest-order field mode, denoted by TEM_{00} , is of interest here. This mode has a rotationally symmetric spherical-Gaussian profile and is the fundamental field mode emitted by most laser cavities. Optical communication networks with long fibre distances and high data rates are exclusively limited to the use of single-mode fibres to avoid multi-path dispersion. The field mode emitted from a perpendicularly cleaved single-mode fibre is also a TEM_{00} Gaussian. This mode therefore represents the most probable beam profile to be found in any coherent optical system and it can be assumed that free-space optical switch architectures must also be designed to manipulate Gaussian beams.

In any z -plane, a transverse TEM_{00} Gaussian field distribution may be described in terms of an instantaneous beam radius w , and a phase wavefront curvature R . w is defined as the radius at which the electric field amplitude falls to $\frac{1}{e}$ of its peak value or the radius

at which the Gaussian intensity falls to $\frac{1}{e^2}$ of the peak intensity.[†] The spherical wavefront radius of curvature R is defined to have a positive value for a diverging beam, tending to infinity, and a negative value for a converging beam. The propagation of a Gaussian field in 3-dimensions is nearly an exact solution of the scalar wave equation and is described by:

$$\tilde{E}(x, y, z) = \tilde{Q}(z) \exp \left[\frac{-jk(x^2 + y^2)}{2} \tilde{Q}(z) \right] \quad (2.3)$$

$$\text{where } \tilde{Q}(z) = \frac{1}{R(z)} - \frac{j\lambda}{\pi w^2(z)}$$

$\tilde{Q}(z)$ determines how the wavefront evolves as the transverse field propagates. After normalisation of equation (2.3), the transverse beam intensity in any z -plane is of the form:

$$I(x, y, z) = \frac{2}{\pi w^2(z)} \exp \left[-2 \frac{x^2 + y^2}{w^2(z)} \right] \quad (2.4)$$

In contrast to geometric ray optics which predict that converging rays are focused to an infinitesimally small spot, physical Gaussian beams propagate to and from a Gaussian 'waist' position. At this waist, the wavefront is flat and the beam radius reaches a finite global minimum value w_o , such that:

$$w(z) = w_o \sqrt{1 + \left(\frac{\lambda z}{\pi w_o^2} \right)^2}, \quad R(z) = z \left(1 + \left(\frac{\pi w_o^2}{\lambda z} \right)^2 \right), \quad \frac{dw}{dz} = \frac{w(z)}{R(z)} \quad (2.5)$$

where z has the value of zero at the waist position. Simple Gaussian beams are very well-behaved because they exhibit ray-like propagation away from the vicinity of waists, and approach an asymptotic value of beam divergence which is inversely related to the value of w_o . Thus to produce a highly 'collimated' Gaussian beam, the waist diameter must be much larger than the wavelength λ . Alternatively, a rapidly divergent beam will be produced from the $a \simeq 5 \mu\text{m}$ core radius of a cleaved single-mode communications fibre. In this case, the beam waist coincides with the fibre end and has an extent determined by the fibre V -number:

$$w_o = a \left(0.65 + \frac{1.619}{V^{1.5}} + \frac{2.879}{V^6} \right) \quad \text{where} \quad V = \frac{2\pi a}{\lambda} NA \quad (2.6)$$

V is proportional to the fibre numerical aperture (NA) and is always less than 2.4 for a single-

[†]Some texts (e.g., Snyder and Love [33]) define Gaussian beam widths differently, but they generally use a different symbol in their representation.

mode fibre. Equation (2.6) is the most commonly used approximation for the Gaussian spot size in step-index single-mode fibres [34]. Other approximations are discussed in [35].

2.2 Holographic Replay

In order to achieve useful optical processing, the Gaussian free-space wavefront must be modified and diffracted by some form of holographic recording. The simplest architecture for viewing the replay fields resulting from the display of dynamic computer generated holograms on an SLM, is the 4- f Gaussian relay shown in figure 2.1.

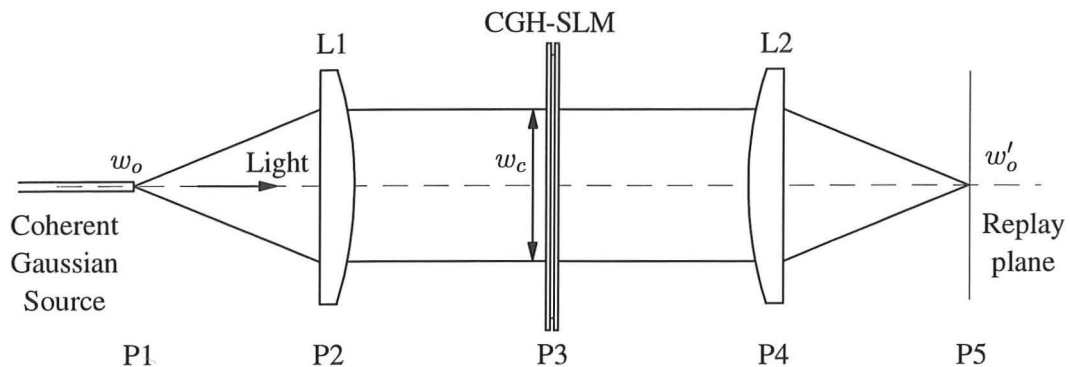


Figure 2.1: Optical 4- f Gaussian relay.

The operation of this symmetrical relay is as follows. In plane P1, coherent light enters the system in the form of a divergent Gaussian beam. This beam profile may be the emitted field from a single-mode fibre-pigtailed laser; the direct output from a semiconductor laser cavity; or may be generated as the result of coherent diffraction through a small spatial filter pinhole. The source is aligned along the z optic axis of the system and the light beam propagates forward until it reaches plane P2, where it is collimated by lens L1. This lens must be arranged in an infinite conjugate ratio configuration, such that plane P1 is exactly one focal distance f , in front of P2. Ignoring the SLM in plane P3 for the moment, the collimated beam propagates a further distance $2f$ and arrives in plane P4, at the back of lens L2. Provided there is no significant aperturing of the Gaussian field, the arguments of symmetry and reversibility imply that the light will arrive in output plane P5 with an identical profile to that in plane P1. With the optics of the relay correctly aligned, Gaussian waists exist in planes P1 and P5 such that $w_o = w'_o$. The positive lenses also create a new

larger waist in plane P3. In practice however, the high degree of collimation actually ensures that the Gaussian phase wavefront is essentially flat in *any* plane between lenses L1 and L2, and not just flat in plane P3.

2.2.1 Optical transformation properties of a positive lens

Inclusion of the CGH-SLM in plane P3 of figure 2.1, has the effect of modifying the collimated wavefront using the phase transmittance function of the hologram, $CGH(x, y)$. To evaluate the field at P5 due to diffraction from the CGH, it is necessary to examine what happens when the altered Gaussian wavefront is refracted by a positive lens of focal length f . By definition, an ideal lens converts a plane wave into a spherical wave. An aberration-free lens therefore simply introduces a spatial parabolic phase-shift onto the incident wavefront. The aperture of lens L2 is finite and may be represented by a complex pupil function $p(x, y)$:

$$p(x, y) = \begin{cases} \exp\left[-\frac{jk}{2f}(x^2 + y^2)\right] & \text{Inside the lens aperture,} \\ 0 & \text{elsewhere.} \end{cases} \quad (2.7)$$

A method of performing the desired propagation of the CGH-modified wavefront through the lens is provided by Fresnel's 'paraxial' version of the scalar wave equation (2.1). Fresnel's equation is based on the assumption that the z dependence of $\tilde{e}(x, y, z, t)$ will be insubstantial compared with the forward phase motion of the harmonic wave as given by $\exp[-jkz]$. Hence $\frac{\partial^2}{\partial z^2} \tilde{E}(x, y, z) \Rightarrow 0$. This approximation is valid for Gaussian beams and other optical fields which do not have significant power travelling in highly deviated directions relative to the z -axis.

The Fresnel integral (2.8) is a paraxial solution to the scalar wave equation. Within the limits of the paraxial approximation, it relates a known field distribution $\tilde{E}(x_o, y_o)$ in a plane $z = 0$, to the optical field $\tilde{E}(x, y)$ that will be produced after propagation of the wavefront through an arbitrary distance z in free-space:

$$\tilde{E}(x, y) \simeq \iint_{-\infty}^{\infty} K(x, y, z; x_o, y_o) \tilde{E}(x_o, y_o) dx_o dy_o \quad (2.8)$$

where $K(x, y, z; x_o, y_o)$ is the 'Kernel' or transfer function of free-space propagation:

$$K(x, y, z; x_o, y_o) = \frac{\exp \left[jk \left(z + \frac{x^2 + y^2}{2z} \right) \right]}{j\lambda z} \exp \left[jk \left(\frac{x_o^2 + y_o^2}{2z} - \frac{xx_o + yy_o}{z} \right) \right] \quad (2.9)$$

Equations (2.8) and (2.9) represent multiplication of the input field by a propagator function, followed by integration over the entire extent of the field. (x_o, y_o) are the coordinates in the plane $z = 0$ and (x, y) are the coordinates after the wavefront has been propagated. Combination and rearrangement of these equations lead to the more convenient and recognisable form of a 2-dimensional Fourier transform:

$$\tilde{E}(x, y) = S_\phi(x, y) \iint_{-\infty}^{\infty} \left\{ \tilde{E}(x_o, y_o) \exp \left[jk \left(\frac{x_o^2 + y_o^2}{2z} \right) \right] \right\} \exp \left[-\frac{jk}{z}(xx_o + yy_o) \right] dx_o dy_o \quad (2.10)$$

where the $S_\phi(x, y)$ term outside the integral only affects the final size and wavefront curvature of the resultant field. Temporarily neglecting the effect of propagation from the SLM to the back of the second lens (see figure 2.1), the wavefront incident on L2 may be represented by a flat Gaussian field multiplied by the CGH transmittance function. This is then further multiplied by the lens pupil function:

$$\tilde{E}(x_o, y_o) = G(w_c) \times CGH(x_o, y_o) \times p(x_o, y_o) \quad (2.11)$$

When the propagating field reaches the focal plane of lens L2 where $z = f$, the quadratic phase term of eqn. (2.10) exactly cancels the pupil function. In addition, the Gaussian illumination term can be moved outside the integral, resulting in a convolution between the output plane Gaussian, waist radius w'_o ($= w_o$), and the Fourier transform of the hologram transmittance function:

$$\begin{aligned} \tilde{E}(x, y) &= \mathfrak{F} \left[G(w_c) \right] * S_\phi(x, y) \iint_{L2} CGH(x_o, y_o) \exp \left[-j(u x_o + v y_o) \right] dx_o dy_o \\ &= G(w'_o) * \left\{ S_\phi(x, y) \mathfrak{F} \left[CGH(x_o, y_o) \right] \right\} \end{aligned} \quad (2.12)$$

where $*$ represents convolution, $\mathfrak{F}[\]$ is the Fourier transform operator, $G(w'_o)$ is a Gaussian waist of radius w'_o , and (u, v) are a scaled coordinate system for the transform. The absolute

z -axis phase change contained in $S_\phi(x, y)$ can also be ignored, leaving:

$$S_\phi(x, y) = \frac{\exp\left[\frac{jk}{2f}(x^2 + y^2)\right]}{\lambda f} \quad \text{and} \quad u = \frac{kx}{f}, \quad v = \frac{ky}{f} \quad (2.13)$$

2.2.2 The Fourier flat-phase condition

In addition to the resultant replay plane intensity- and phase-profiles calculated from the complex-valued spatial Fourier transform of the hologram function, equation (2.13) predicts that there is also a residual spherical wavefront curvature from $S_\phi(x, y)$. If equation (2.10) is used a second time to take account of propagation from the CGH to the back of L2, and provided this distance is set to exactly one focal length f , on repeating the analysis it is found that the spherical curvature term disappears [31]. Hence we are left with a simple Fourier transform relationship between the CGH transmittance function and the field it produces in output plane P5. This is the Fourier 'flat-phase' condition, obtained by configuration of the optical system as a 4- f structure:

$$\tilde{E}(x, y) = \frac{1}{\lambda f} G(w'_o) * \mathfrak{F}\left[CGH(x_o, y_o)\right] \quad (2.14)$$

The simple form of equation (2.14) and the discrete nature of the SLM pixels, makes evaluation of the hologram replay field exceptionally well suited to computer-based numerical fast Fourier transform (FFT) algorithms [36]. To obtain maximum light efficiency, the SLM pixels should only modulate the phase of the incident Gaussian beam and not the intensity. Hence the hologram transmittance $CGH(x_o, y_o)$ will typically be complex and may be represented as a discrete function $CGH(X_m, Y_n)$:

$$CGH(X_m, Y_n) = \exp\left[j\Phi(X_m, Y_n)\right] \quad (2.15)$$

where (X_m, Y_n) are the discrete pixel coordinates and the function Φ represents the phase retardations of each pixel.

2.3 Ferroelectric Liquid Crystal Spatial Light Modulators

Molecularly aligned ferroelectric liquid crystals (FLCs) exhibit electro-optic effects which alter the polarisation state of the light transmitted through them. Typically these FLC

materials are arranged as the dielectric of a capacitor with transparent electrodes, and when used between crossed plane-polarisers arranged around the device, FLC-SLMs can be configured to modulate either the intensity or the phase of the incident light.

The need for fast high-contrast displays has driven the development of FLC devices as intensity modulators [37], but the realisation that a simple re-orientation of the polarisers produces phase-only modulation was a relatively recent discovery [38, 39]. The use of FLC-SLMs as programmable diffractive elements has many applications to coherent optical systems such as dynamic holography [40, 41], optical beam steering [42, 43], wavelength selection [44], and image processing [16, 45].

2.3.1 Ferroelectric molecular dynamics

Ferroelectric properties are exhibited by liquid crystals in the smectic C* phase. The FLC molecules are organised in layers and are described by a layer normal vector \hat{z} , pointing perpendicularly through all layer boundaries [37]. When the FLC cell is thicker than about $10\mu\text{m}$, the molecules have a high degree of orientational freedom and may be considered to be in a 'bulk' state. The chirality of the molecular structure causes the long axis of each molecule to tilt out from the layer normal by a temperature-dependent average tilt angle θ . Thus each molecule may be modelled as if it was lying along the surface of a cone, with freedom to rotate about the apex, figure 2.2. Within each layer the FLC molecules align in the same tilted direction, given by a molecular director \hat{n} . The resultant dipole moment of each layer produces a local polarisation density \vec{P} at right angles to \hat{n} and \hat{z} .

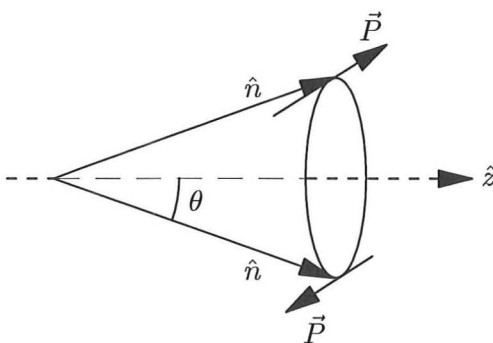


Figure 2.2: The conical degrees of freedom of an FLC 'bulk' molecule.

When an electric field is applied across the cell, \vec{P} follows the field and causes the layer molecules to rotate around an arc of the cone to a position of equilibrium. This lowest energy position depends on the radius of the cone and the magnitude of the applied electric field. Rotation of the director has a corresponding effect on the optical property of the device. Hence by modulating the electric field, the director can be arbitrarily moved around the cone's surface, generating a 'greyscale' sequence of possible molecular positions. However the main drawback with this modulation scheme is that the helical rotation of molecular orientations between layers tends to cancel the net dipole when the applied voltage is small, causing a non-linear switching response.

When FLC materials are confined to thinner cells (typically $2\mu\text{m}$ or less), surface interactions at the cell boundaries dominate the molecular dynamics. In particular, when a textured alignment layer of material is present on both cell surfaces [46], the FLC molecules can be forced to surface-stabilise and align in planes strictly parallel to the cell boundaries. This effectively collapses the cone of allowed director states into a single plane and restricts the average molecular positions \hat{n} , to only two diametrically opposing states, separated by the full cone angle 2θ , figure 2.3.

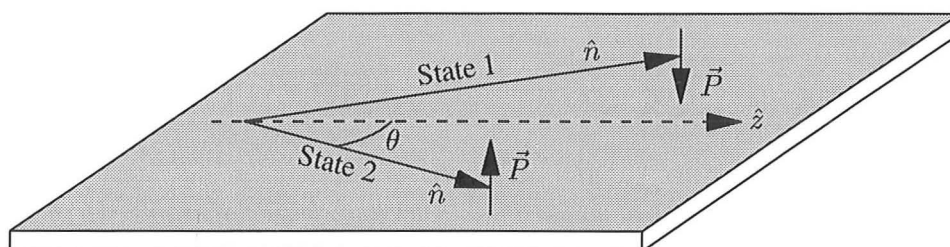


Figure 2.3: The two degrees of freedom of a surface-stabilised FLC molecule.

In contrast to the bulk state where molecules in consecutive FLC layers may have different molecular directors along their respective cones, molecules in surface-stabilised cells all have exactly the same orientation. Due to the strong dipole moment that is now present throughout the entire device, applying an electric field across the thin cell causes the molecules to rapidly 'flip' into the equilibrium state of lowest energy. Reversing the field direction causes them to flip back again.

Although surface-stabilised FLC operation is essentially limited to a binary effect, switching occurs on a relatively short time-scale because of the ferroelectric nature of the interaction between the liquid crystal and the applied field. The binary properties of the majority of FLC modulators means that they can only be used to produce either black-and-white images or 0- and π -phase screens. This limits their performance as programmable diffractive elements but suitable holographic design procedures help to maximise their efficiency under this constraint.

The stabilised molecular geometry described above is known as the 'bookshelf' structure because the molecular layers are aligned perpendicular to the cell boundaries and have the geometry of a row of books, figure 2.4(a). In practice, the molecular pinning forces at the glass surfaces cause the ideal structure to collapse into a chevron, with a sharp layer discontinuity running along the centre of the cell, figure 2.4(b). The chevron form is degenerate because the layers may point in either of two directions. Boundaries between the two forms can sometimes be observed as undesirable 'zig-zag' defects within cells. Although heat and electrical treatment of these devices may temporarily remove the visible defects [47], they are essentially a product of the manufacturing process and will reappear if the applied electric field is too large.



Figure 2.4(a): Bookshelf layer structure.

Figure 2.4(b): Chevron layer structure.

A chevron structure implies that the layer normal \hat{z} , and hence the molecular cone axis, is inclined at an angle to the surface boundaries. However, the presence of surface stabilisation still forces the molecules to lie in surface-parallel planes. Thus the two equilibria states are no longer on diametrically opposed sides of the cone, but rather lie at the ends of a shorter arc of the cone. The chevron structure therefore reduces the effective molecular tilt angle and decreases the magnitude of the electro-optic effect that is observed, but leads to an increased switching speed. FLC switching times (typically $< 15\mu\text{s}$ for 2θ approaching 45° but greater than 10V drive voltage) depend strongly on the effective molecular tilt angle but in reality, actual SLM devices are usually limited by the speed of the driving electronics, rather than by the material viscosity.

2.3.2 *Surface-stabilised FLC pixel structures*

A spatial light modulator typically consists of an array of $M \times N$ individually switchable pixels. Figure 2.5 shows a schematic of a single FLC pixel structure in a transmissive display device. The liquid crystal lies between two glass plates which have been attached to one another using a glue seal around the edges of the glass. The inner sides of the glass are patterned with transparent indium tin oxide (ITO) electrodes and the surface-stabilisation of the FLC molecules is achieved by obliquely evaporated SiO layers or by brushed polymer layers deposited on top of the electrodes. On one glass plate the parallel column electrode stripes run vertically and on the other, row electrodes run horizontally. Each pixel active region is therefore defined by the overlap area of a row and column electrode. Addressing takes place by applying an enabling voltage to a single row and then writing data on all columns. The full frame is addressed by repeating this process down all rows. The inherent bistability of fully surface-stabilised FLC materials means that the data will be retained whilst the other rows are being scanned. The dead-space areas between electrodes are regions which cannot be modulated. These regions decrease the contrast (in intensity operation) or the diffraction efficiency (in phase operation) of the SLM.

The liquid crystal thickness is controlled by spherical or rod-shaped glass spacers scattered between the glass plates. These spacers have an undesirable lensing effect on the light passing through them, but also potentially induce large area liquid crystal defects [48]. In small devices it is sometimes possible to keep the spacers away from the pixels, confined to the glue seal only.

This passive glass-substrate technology is well suited to display applications, but is limited by the density of electrical connection to the ITO electrodes which is required at the glass plate edges. A promising innovation in the development of miniature FLC devices is to construct SLMs directly on the top of CMOS VLSI silicon chips [15]. These devices operate in reflection and each pixel is addressed by a signal applied to an aluminium pad which doubles as the pixel mirror, figure 2.6. The use of CMOS circuitry at each pixel also removes the reliance on full FLC material bistability and enables pixel pitches down to about $25\mu\text{m}$ to be addressed relatively easily.

If the optical-quality aluminium pixel mirror is fabricated as part of the normal CMOS processing, it has to be placed in an area away from the optically irregular pixel drive circuitry. This introduces an unacceptable amount of dead-space and leads to unpredictable

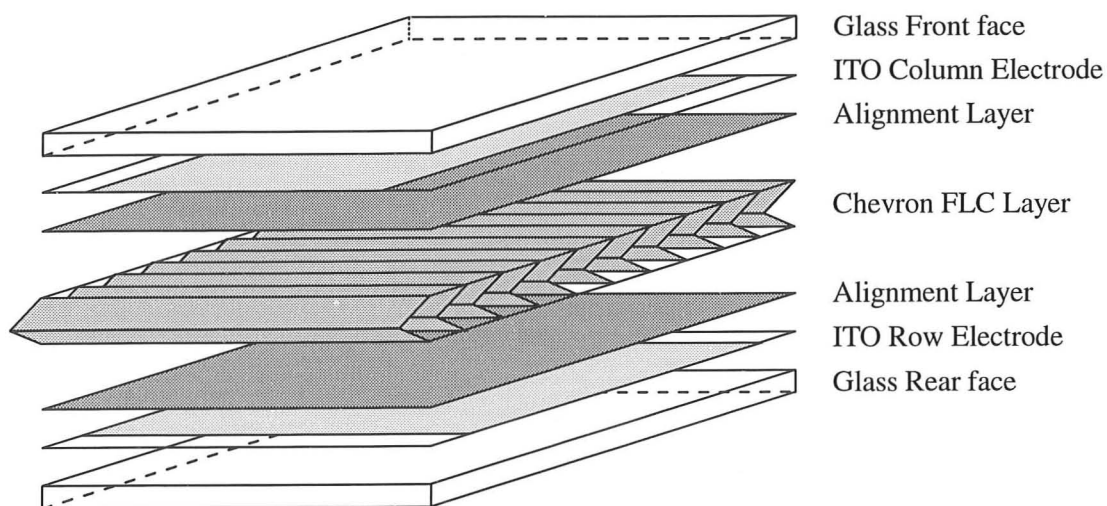


Figure 2.5: The structure of a single transmissive SLM pixel.

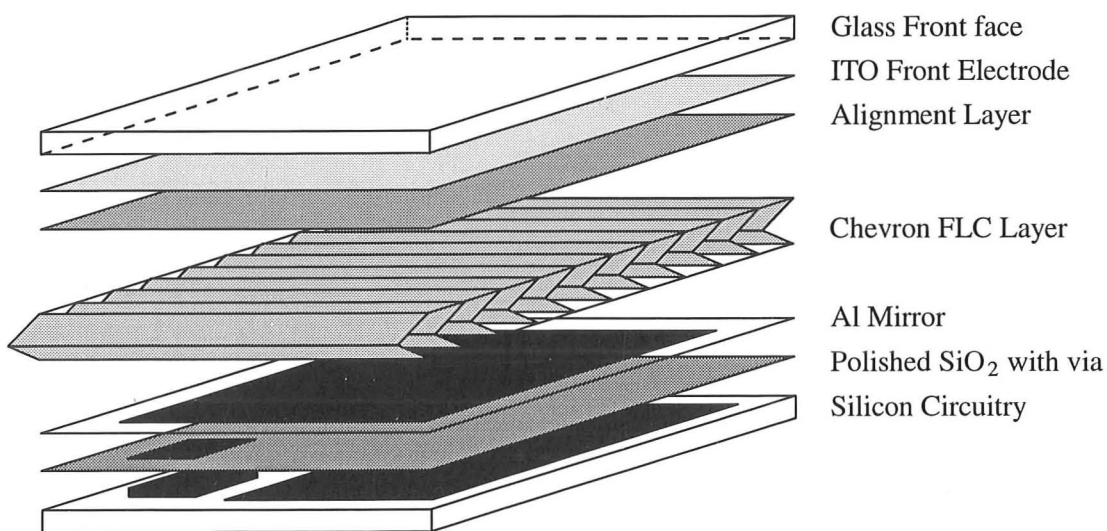


Figure 2.6: The structure of a reflective silicon backplane SLM pixel.

FLC modulation effects above the circuitry. Planarisation of the silicon surface has recently solved these problems [49]. This process involves growing a layer of silicon dioxide over the whole silicon wafer after processing, but before SLM assembly. This layer is then mechanically polished to an optical flatness and vias are etched through to contacts in the underlying circuitry. As the final stage, new aluminium pixel mirrors are evaporated onto the surface.

Using this technique, the pixel dead-space may be decreased to less than 10% and the optical quality is greatly improved. A potentially simpler but as yet unproven alternative to mechanical polishing may be to planarise the CMOS circuitry by spinning a polymer material over it.

2.3.3 Backplane SLM pixel circuitry

The development of CMOS backplane SLMs has important implications for free-space optical architectures because they potentially provide the ability to have high pixel densities in very compact volumes. CMOS devices interface readily with other electronic components and typically operate an order of magnitude faster than their passive transmissive counterparts. The use of silicon circuitry also provides the opportunity for placing some local electronic processing at each pixel to enhance the device functionality.

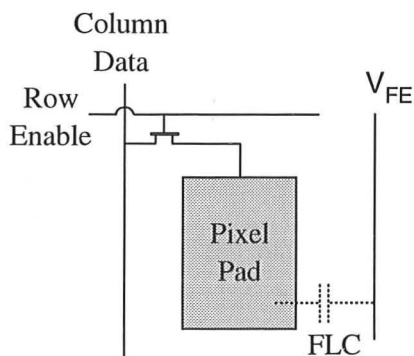


Figure 2.7(a): DRAM pixel modulator.

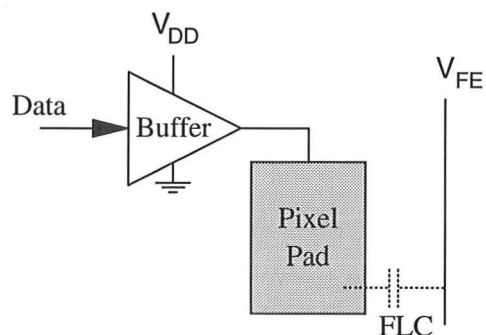


Figure 2.7(b): SRAM pixel modulator.

Essentially backplane SLMs operate as optically-readable memory. Although the integration of photodiodes onto the silicon circuitry also introduces the possibility of optically addressed 'smart pixels' [50], usually we are only concerned with electronic addressing schemes (EASLMs). Two binary storage schemes are well known in conventional silicon

memory technology, and these have been incorporated into EASLM designs. The dynamic-RAM pixel circuitry [15], figure 2.7(a), has a single transistor per pixel and the 1-bit binary memory state is stored as a capacitive charge polarity on the actual mirror contact. The low transistor count in DRAM devices make them easy to miniaturise, but the support electronics must continuously refresh the pixel voltages as they tend to leak charge through parasitic coupling effects. This arises because each pixel can only be latched to the power rails for a finite amount of time and must otherwise remain in a high-impedance state. A faster and more robust approach is the static-RAM cell [17], figure 2.7(b), which has a bistable latch at each pixel. These modulators require more silicon area, but the pixels are effectively continuously connected to a power rail and they thus produce better FLC modulation.

2.4 Computer Generated Holograms

The availability of only two ferroelectric modulation states means that practical holograms displayed on FLC-SLMs are usually a coarsely phase-quantized representation of the sampled 2-dimensional Fourier transform of the desired replay field. Simply thresholding the continuous transform usually results in poor diffraction efficiency because of the high degree of unwanted quantization noise that is introduced. This has led to much interest in more complex methods for reducing quantization noise. Hence the generation of binary phase holograms is very well documented [51–58]. These methods are generally based on iterative fast Fourier transform algorithms and rely on the use of pixels capable of switching through a phase angle of precisely π .

2.4.1 *Binary phase-only modulation with ferroelectric liquid crystals*

A surface-stabilised FLC material exhibits the properties of an optically-active uniaxial crystal. The fast and slow birefringent axes lie in the plane of the device, parallel to the cell surface and perpendicular to the z -axis direction of light transmission. One of the two birefringent axes is usually parallel to the FLC molecular director \hat{n} and the other axis is orthogonal to this. In most FLC materials, linear polarised light aligned along the fast axis of the FLC material will experience the ordinary refractive index n_o . Light aligned parallel to the slow axis will experience the extraordinary index n_e . These birefringent axes rotate about z through the switching angle 2θ as the direction of applied voltage is altered. Each pixel of the display thus acts exactly as an independently controlled waveplate with two stable angular positions.

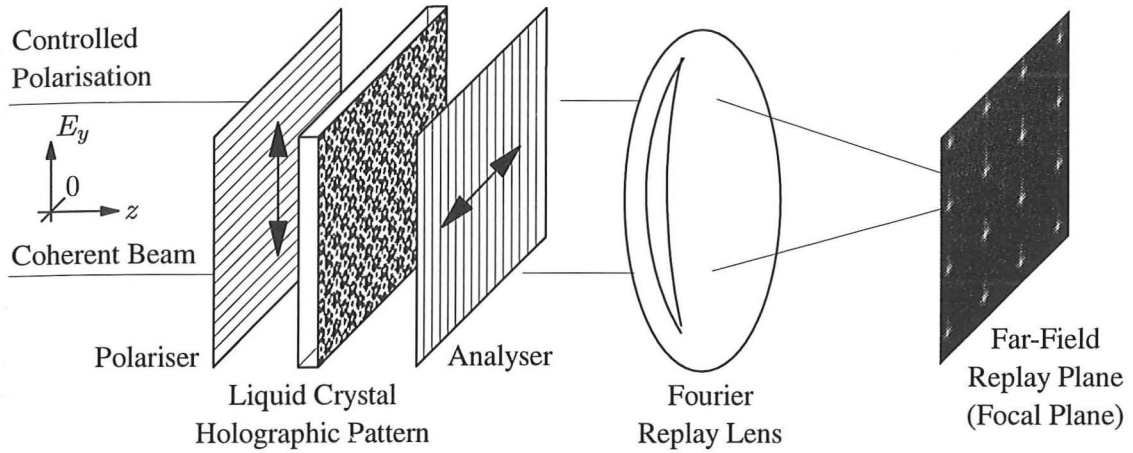


Figure 2.8: Reconfigurable diffractive optical element.[†]

Binary phase-only operation of an FLC-SLM is achieved by placing the device between crossed 90° polarisers, figure 2.8. The input polariser is oriented such that the resultant polarisation direction bisects either the two possible angular positions of n_o , or the two positions of n_e . Each pixel of the display then produces a phase-only change of either 0 or π [39]. Considering a single pixel only, the field produced in figure 2.8 by the first polariser must take the form:

$$\begin{aligned}\tilde{\epsilon}_x(z, t) &= 0, \\ \tilde{\epsilon}_y(z, t) &= E_y \cos(\omega t - kz)\end{aligned}\tag{2.16}$$

where E_y is the field amplitude in the vertical plane. The two liquid crystal states correspond to angular positions of the birefringent axes relative to the input polarisation direction of either $+\theta$ or $-\theta$, figure 2.9. The input light must now be resolved into parallel and perpendicular complex amplitude components along the fast and slow axes:

$$\begin{aligned}\text{Along the fast axis:} & \quad E_f = E_y \cos(\pm\theta) \\ \text{slow axis:} & \quad E_s = E_y \sin(\pm\theta) \exp[jk\Delta nT]\end{aligned}\tag{2.17}$$

where $k\Delta nT$ is the phase retardation experienced by the polarised component which is parallel to the slow axis as it passes through the FLC cell, relative to the orthogonal component which is parallel to the fast axis. Δn is the birefringence of the FLC material defined as $\Delta n = |n_o - n_e|$, and T is the cell thickness. The resulting output field components are

[†] “Holepad” hologram courtesy of T.D. Wilkinson and D.C. O’Brien.

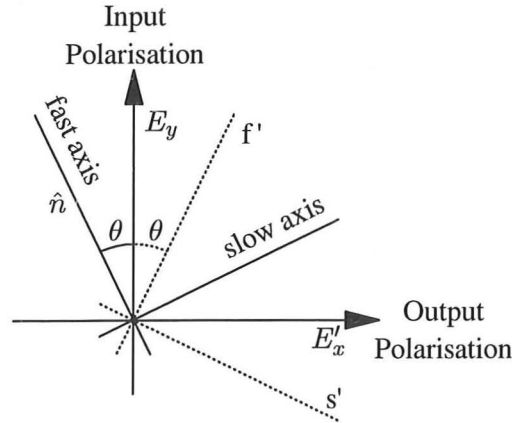


Figure 2.9: Orientation of polarisers for phase-only operation.

then ‘analysed’ by the second polariser. The vertical field component is discarded by this analyser and the complex amplitude of the horizontally polarised output field $\tilde{\epsilon}'$ is:

$$\begin{aligned} E'_x &= \left\{ E_y \sin(\pm\theta) \exp[jk\Delta nT] \right\} \cos(\pm\theta) - \left\{ E_y \cos(\pm\theta) \right\} \sin(\pm\theta) \\ &= \pm \frac{1}{2} E_y \sin 2\theta \left(\exp[jk\Delta nT] - 1 \right) \end{aligned} \quad (2.18)$$

The change in sign of E'_x in (2.18) as the FLC switches between states implies that the required $(0, \pi)$ phase-only modulation has been achieved. Binary phase modulation is always possible, irrespective of the cell thickness and the FLC parameters. In general however, there is a transmission loss associated with each polariser. The first polariser absorbs power during the conversion of the original input light into a vertically polarised state. But ignoring this loss and any other additional efficiency losses that will be present in a real experimental system, a reduced transmission also arises because the vertical polarisation component at the second polariser is discarded. The transmission efficiency of an ideal binary phase FLC-SLM is therefore predicted from the normalised intensity of E'_x :

$$\begin{aligned} T &= \frac{|E'_x|^2}{|E_y|^2} = \frac{1}{4} \sin^2 2\theta \left(2 - 2 \cos(k\Delta nT) \right) \\ &= \sin^2 2\theta \sin^2 \frac{k\Delta nT}{2} \end{aligned} \quad (2.19)$$

From equation (2.19) it can be seen that the transmission loss may be minimised by manufacturing the device with a half-waveplate thickness ($k\Delta nT = \pi$) and by choosing an FLC

material with an effective tilt angle as close to $\theta = 45^\circ$ as possible. Commercially available FLC materials typically have a birefringence of around $\Delta n = 0.18$ at a wavelength of $\lambda = 633\text{nm}$. Thus the glass rod spacers within any FLC device which has been optimised for the visible spectrum, should be just less than $T \simeq 2\mu\text{m}$ wide. Optimising the switching angle is more problematic because it requires the chemical synthesis of new FLC materials. Considerable efforts have been made to develop materials with an effective tilt angle of $\theta = 22.5^\circ$ [59] because this is the condition that produces maximum contrast when the SLM is configured as an intensity modulator. Such materials would only introduce a 3dB power loss in a phase CGH-SLM. However, experimental materials do exist which approach the full 45° tilt, e.g., Chisso CS2004 [60] or [61]. The main disadvantage with these materials is the trade-off between high tilt angle and switching speed.

CHAPTER 3

The Polarisation Insensitive One to Any Optical Interconnect

When attempting to construct single-mode fibre interconnects, it should be noted that the relatively long fibre distances involved in point-to-point optical data transport tend to scramble the polarisation state of the optical signals. Even stress-induced polarisation-preserving fibres become ineffective when the total fibre run is more than about 1km. It must therefore be assumed that the polarisation state within a fibre is random and may even be found to fluctuate unpredictably if a section of the fibre is mechanically disturbed.

If the operation of network routers and interconnects is to remain optically transparent, the components used in the system design must also remain insensitive to polarisation. Any polarisation selective element that is present in the optical path will potentially cause the output data signal power to catastrophically fade as the input polarisation state drifts. In any case, effective polarisers at the $\lambda = 1.55\mu\text{m}$ communication band tend to be prohibitively expensive (e.g., Glan-Thompson cube-splitters) or have very high material absorption losses (e.g., metallic thin film polarisers). Hence to avoid the (possibly very large) power loss associated with the propagation of an arbitrarily polarised light source through a diffractive ferroelectric liquid crystal device, it is highly desirable to make the phase operation of the FLC-SLM completely independent of polarisation.

3.1 Polarisation Insensitive Ferroelectric Operation

The transmission efficiency of a dynamic FLC holographic optical element was derived in equation (2.19). To minimise the optical power loss, the device should be manufactured with

a half-waveplate effective optical thickness and employ an FLC material with a switching angle as close to 90° as possible. O'Callaghan and Handschy [40] realised that provided these two criteria can be met, the fast and slow birefringent axes of the material simply swap positions as the liquid crystal is switched. This causes the input polarisation to be completely rotated into the plane of the analyser, making the effect of this output polariser redundant. Because each pixel now acts as a perfect $(0, \pi)$ binary phase modulator, the input polariser may also be removed. Thus the SLM operates in a polarisation independent way for arbitrary input polarisation states.

Few FLC materials exist that exhibit a switching angle of $2\theta = 90^\circ$, and they are difficult to align in a surface stabilised form. An alternative approach [62] obtains an aggregate electro-optic switching angle of 90° by using two layers of 45° material separated by a fixed $\frac{\lambda}{4}$ -waveplate, but the critical optical alignment between the two pixel-planes that is required with this type of geometry makes it less attractive compared to the shift-invariant diffraction properties of normal FLC holograms.

Until recently it had been assumed that polarisation insensitive operation could not be achieved with the more common smaller switching angle materials and thus the application of FLC-SLM technology to optical fibre switches appeared to be severely limited. This chapter presents a full polarisation analysis and reveals that the accepted view is not in fact true. FLC-SLMs configured as diffractive optical elements are actually inherently insensitive to the polarisation of the light passing through them [63]. This realisation has led to the first demonstration of dynamic polarisation independent single-mode fibre interconnects [64], and also has important implications for a much wider range of optical processing applications.

3.1.1 *Polarisation analysis*

When the polarisers are removed from an FLC-CGH, true phase changes no longer occur at each pixel but rather there are alterations in the light polarisation state passing through the display. The resultant polarisations diffract and interfere as they propagate through a Fourier replay lens in the usual way, figure 3.1.

The intensity of any point in the wavefront incident upon the SLM can be considered as the incoherent sum of orthogonal x - and y -polarised transverse electromagnetic fields. Thus an

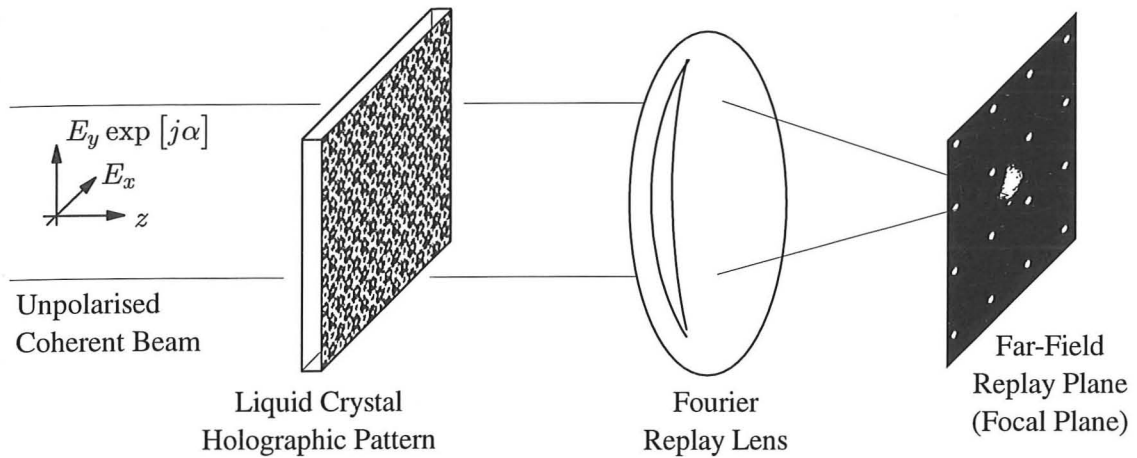


Figure 3.1: Polarisation insensitive ferroelectric hologram and replay.

arbitrary instantaneous polarisation phasor may be expressed in a vectored form:

$$\tilde{E}_{inst} = \begin{pmatrix} E_x \\ E_y \exp[j\alpha] \end{pmatrix} = E_x \mathbf{i} + E_y \exp[j\alpha] \mathbf{j} \quad (3.1)$$

where α in (3.1) describes the phase difference between the orthogonal fields. Only the effect of polarisation is of interest here and so we will ignore the Gaussian profile (which only has a convolution effect on the replay field) and assume that the SLM is illuminated everywhere by a flat wavefront with unity intensity such that $E_x^2 + E_y^2 = 1$. Thus \tilde{E}_{inst} encompasses all states of polarisation, i.e., any direction of linear polarised light is described by the relative magnitudes of E_x and E_y when $\alpha = 0$ or π ; clockwise or anti-clockwise circular polarisation states are achieved when $E_x = E_y$ and $\alpha = \pm \frac{\pi}{2}$; and all other conditions give elliptical states.

Light which is orthogonally polarised along the fast and slow birefringent axes of the FLC material, experiences relative phase retardations as it passes through the SLM given by the Jones matrix \mathbf{J} of propagation [65]. A convenient anti-clockwise rotation matrix \mathbf{R} for conversion to this fast-slow axis coordinate system may also be defined at this point:

$$\mathbf{J} = \begin{pmatrix} \exp[jk\Delta nT] & 0 \\ 0 & 1 \end{pmatrix}, \quad \mathbf{R} = \begin{pmatrix} \cos 2\theta & \sin 2\theta \\ -\sin 2\theta & \cos 2\theta \end{pmatrix} \quad (3.2)$$

where k is the wavenumber, $\Delta n = |n_o - n_e|$ is the birefringence and θ is the FLC molecular tilt angle. The light \tilde{E}_{inst} is perpendicularly incident upon an array of birefringent FLC

pixels such that the \mathbf{k} -vector of propagation points along the z -axis through the FLC surface. Each pixel has a thickness T and will be in one of its two stable states. Let ψ be the angle between the direction of the x -axis and the direction of ordinary refraction, n_o . Because $\tilde{\mathbf{E}}_{inst}$ is an arbitrary state which has only been described in (x, y) coordinates for convenience, without loss of generality, let one of the two values of ψ be zero. The relevant plane through the optical indicatrix is shown as figures 3.2(a) and 3.2(b), corresponding to the two fully-switched pixel states.

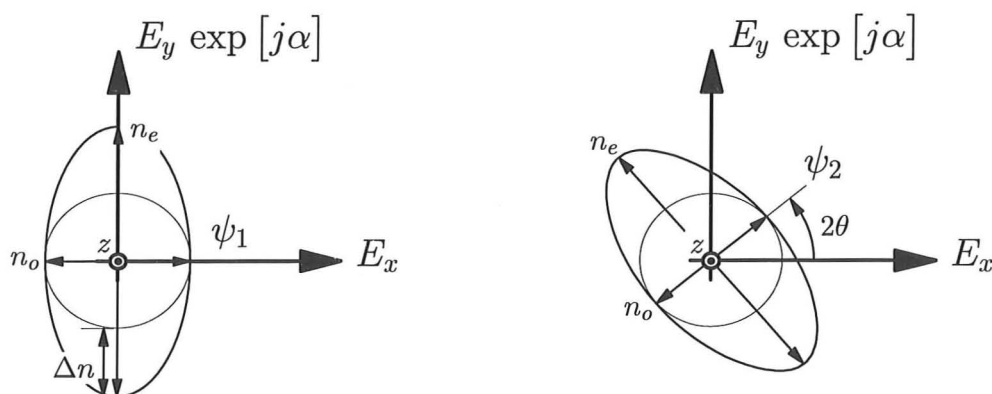


Figure 3.2(a): FLC indicatrix: state 1.

Figure 3.2(b): FLC indicatrix: state 2.

By means of the Jones matrix, the input field may now be propagated through FLC pixels in oppositely switched states, $\psi_1 = 0$ and $\psi_2 = 2\theta$. The two possible polarisation vectors emergent from the pixels and resolved parallel and perpendicular to ψ_2 have the form:

$$\text{With all pixels in state 1: } \tilde{\mathbf{E}}_1 = \mathbf{R}\mathbf{J}\tilde{\mathbf{E}}_{inst} = \begin{pmatrix} c_1 + c_2 \\ c_3 \exp[jk\Delta nT] + c_4 \end{pmatrix} \quad (3.3)$$

$$\text{With all pixels in state 2: } \tilde{\mathbf{E}}_2 = \mathbf{J}\mathbf{R}\tilde{\mathbf{E}}_{inst} = \begin{pmatrix} c_1 + c_2 \exp[jk\Delta nT] \\ c_3 + c_4 \end{pmatrix} \quad (3.4)$$

$$\begin{aligned}
 \text{where } c_1 &= \exp[jk\Delta nT] \cos 2\theta E_x & ; & & c_2 &= \sin 2\theta \exp[j\alpha] E_y \\
 c_3 &= -\sin 2\theta E_x & ; & & c_4 &= \cos 2\theta \exp[j\alpha] E_y
 \end{aligned}$$

From changes to the x - and y -polarisations between states (3.3) and (3.4), it may be seen

that each field component consists of a term (c_2 or c_3) that is modulated through a phase angle of $\exp[jk\Delta nT]$, and a constant offset term (c_1 or c_4) that remains fixed as the pixels switch. In the absence of polarisers, this non-zero mean field value implies that the normalised Fourier transform relationship between the binary hologram pattern and its far-field replay must be modified to include an undiffracted zero-order 'DC spike':

$$\mathfrak{F}\left[a_{dc} + a_{ac}CGH(X_m, Y_n)\right] = a_{dc}\delta(x, y) + a_{ac}r(x, y) \quad (3.5)$$

where $\delta(x, y)$ is a Dirac delta function centred on the optic axis, $CGH(X_m, Y_n)$ is the discrete binary phase hologram transmittance function consisting of ± 1 's appropriately weighted to normalise the optical power, $r(x, y)$ is the Fourier transform replay function of this hologram with a total integrated power of unity, and a_{ac} and a_{dc} are the optical ratios diffracted into the replay field and into the unwanted zero-order respectively, such that $a_{ac}^2 + a_{dc}^2 = 1$.

To calculate the useful replay power efficiency given by a_{ac}^2 , the polarisation components of (3.3) and (3.4) must be rewritten in terms of their mean DC value, superimposed onto a zero-mean AC phase modulation:

$$\tilde{E}_1 = \begin{pmatrix} \mathcal{X}_{dc} + \mathcal{X}_{ac} \\ \mathcal{Y}_{dc} - \mathcal{Y}_{ac} \end{pmatrix} \quad \text{and} \quad \tilde{E}_2 = \begin{pmatrix} \mathcal{X}_{dc} - \mathcal{X}_{ac} \\ \mathcal{Y}_{dc} + \mathcal{Y}_{ac} \end{pmatrix} \quad (3.6)$$

$$\begin{aligned} \text{where } \mathcal{X}_{dc} &= c_1 + \frac{c_2}{2} \left(1 + \exp[jk\Delta nT]\right) & ; & \quad \mathcal{X}_{ac} = \frac{c_2}{2} \left(1 - \exp[jk\Delta nT]\right) \\ \mathcal{Y}_{dc} &= c_4 + \frac{c_3}{2} \left(1 + \exp[jk\Delta nT]\right) & ; & \quad \mathcal{Y}_{ac} = \frac{c_3}{2} \left(1 - \exp[jk\Delta nT]\right) \end{aligned}$$

From Fourier theory, the light power a_{dc}^2 that passes undiffracted through the CGH-SLM and forms the unwanted on-axis replay spot $\delta(x, y)$, is the intensity of the mean complex field amplitude transmitted by the SLM. Therefore a true $(0, \pi)$ phase-only hologram, e.g., with polarisers, will not form a zero-order spot provided that every CGH used by the system is well designed with equal numbers of FLC pixels of each state, $+1$ or -1 . These phase-only holograms have a mean pixel field amplitude of zero but suffer an intensity transmission loss, i.e., $a_{dc} = \sum CGH(X_m, Y_n) = 0$ and $a_{ac}^2 = T \leq 1$. In the absence of polarisers however, the undiffracted on-axis power is derived from the simple mean of the two pixel fields of (3.6):

$$a_{dc}^2 = \left|\frac{1}{2}(\tilde{E}_1 + \tilde{E}_2)\right|^2 \quad (3.7)$$

Since \tilde{E}_{inst} and therefore \tilde{E}_1 and \tilde{E}_2 have been normalised, the non-zero replay power is:

$$a_{ac}^2 = (1 - a_{dc}^2) = \left| \frac{1}{2}(\tilde{E}_1 - \tilde{E}_2) \right|^2 \quad (3.8)$$

and observing the independence of the x - and y -orthogonal polarisations, the proportion of power η_s that is replayed in the desired function $r(x, y)$, is found from (3.6) and (3.8):

$$\eta_s = \frac{a_{ac}^2}{|\tilde{E}_{inst}|^2} = \frac{\left(\left| \frac{1}{2}c_2 \right|^2 + \left| \frac{1}{2}c_3 \right|^2 \right) \times \left| 1 - \exp[jk\Delta nT] \right|^2}{E_x^2 + E_y^2} \quad (3.9)$$

which simplifies somewhat surprisingly into an expression that is completely independent of the original input polarisation variables E_x , E_y and α :

$$\eta_s = \sin^2 2\theta \sin^2 \frac{k\Delta nT}{2} \quad (3.10)$$

Equation (3.10) predicts that in the absence of polarisers, the amount of light that is diffracted by an FLC-CGH is always a constant ratio of the input optical power. Simulations of random and time-variant polarisation states show that the distribution of light away from the zero-order is unaffected by the removal of polarisers and apart from the addition of the central spot, the holograms replay as before. Hence in diffraction, FLC-SLMs are equivalent to pixel arrays of imperfect $(0, \pi)$ phase modulators, and once the zero-order loss (3.10) has been accounted for, the design and analysis of an optical system is the same as it would be for a true 'phase-only' device. In fact the "diffractive phase-efficiency" η_s is identical to the phase-only transmission efficiency T from equation (2.19), only now there is no requirement for a controlled (linear) input polarisation state. Hence it appears that light which would have been absorbed by the system polarisers now simply passes undiffracted into a 'zero-order' spot. More importantly, there is no excess loss or signal fading associated with the initial conversion of an arbitrary polarisation state into a linear one. This result leads to the conclusion that there is no need to use polarisers in any diffractive FLC optical system that is unaffected by a zero-order, although to maximise the system efficiency, the FLC thickness and switching angle still need to be optimised as before.

3.1.2 Experimental verification of polarisation independence

The experimental verification of polarisation independent FLC-SLM operation can be easily performed and contrasted with binary phase-only operation using a simple Gaussian relay.

The SLM used in this experiment was a 2DX128 supplied by THORN EMI CRL. This device is a transmissive SLM with a total usable square aperture of $(28.16\text{mm})^2$, comprising an array of 128×128 passively addressed pixels on a $220\mu\text{m}$ pitch. On both glass surfaces there is an associated $5\mu\text{m}$ dead-space between the ITO electrodes and the device thickness is controlled with $2\mu\text{m}$ spherical spacers which squash slightly to $1.7 - 1.8\mu\text{m}$. This thickness gives the device an optimised operational performance at a wavelength close to 633nm . In conjunction with high quality polymer-sheet polarisers, the SLM as an intensity modulator produces contrast ratios in excess of 100:1 [66], and exhibits excellent phase-only modulation properties. The liquid crystal birefringence is $\Delta n = 0.18$.

For the comparative purposes of this experiment, a testcard hologram was chosen which was already known to produce a clear and distinctive replay field pattern. The experimental Fourier transform replay of this hologram (figure 3.3(a)) is a 4×4 array of spots arranged on a square geometric grid, centred about the optic axis. The binary CGH was generated by means of a simulated annealing algorithm [18, 58]. This algorithm is an iterative procedure which initialises with a random screen of ± 1 binary phase pixels to represent the $(0, \pi)$ hologram. The desired replay field is specified mathematically and is used in a cost function to evaluate the effects of pixel changes to the binary phase screen. Hence the phase pixels are iterated to the final CGH structure as the algorithm progresses.

The CGH was displayed as a static image on the FLC-SLM. It was illuminated with coherent light from a $\lambda = 633\text{nm}$ HeNe laser which had been coupled into a single-mode fibre of core diameter $3.8 \pm 0.5\mu\text{m}$ (rms). The end of this fibre was cleaved and the output divergent beam ($w_o \simeq 2.3\mu\text{m}$) was collimated by a 40mm diameter, 125mm focal length achromatic doublet lens, to form an approximately 22mm ($\frac{1}{e^2}$ intensity) diameter Gaussian beam. After passing through the SLM, the replay field image was formed on the surface of a silicon CCD camera by means of a reversed doublet lens having an effective focal length greater than 125mm . The effect of mismatching the two lenses is only that of a magnification of the image plane to a more convenient viewing diameter.

With crossed polarisers correctly aligned around the SLM to achieve phase-only operation, polarisation changes induced by random micro-bending of the input fibre caused the intensity of the 16 replay spots to fluctuate, fading the output signal almost to zero at times. A similar effect would have been observed if these polarisation changes had originated from the laser itself. After removal of both polarisers, all replay spots immediately appeared at least

2.3dB brighter on the camera due to the elimination of the polarisation conversion and material absorption losses, figure 3.3(b). In addition, the optical quality of the replay field was enhanced because of the removal of some blurring effects associated with non-uniformities in the sheet polariser thicknesses. Micro-bending of the input fibre now had no effect on the experimental replay intensity.

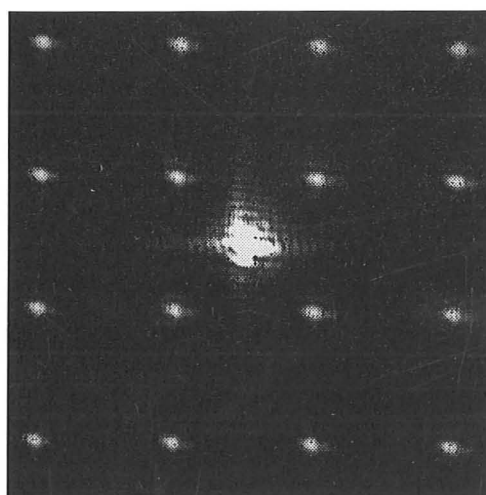
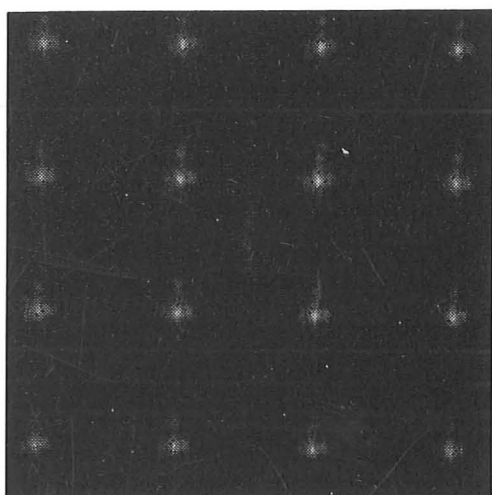


Figure 3.3(a): Replay with polarisers.

Figure 3.3(b): Replay without polarisers.

In the absence of polarisers, the positions of the replay spots were unaltered but an on-axis spot was added to the image as predicted. Due to the SLM having a measured switching angle of only 28° , from equation (3.10) the amount of power in the zero-order is considerably greater than the diffracted power shared into each of the 16 spots. Figures 3.3(a) and 3.3(b) are frame captured images from the CCD at the same fixed camera gain level. In 3.3(b), the zero-order power was more than sufficient to locally saturate part of the CCD array and cause electrical charge leakage crosstalk in the image. As expected, the central spot was observed to have exactly the same Gaussian diameter as the other diffracted spots when the optical power was reduced.

Removal of the first polariser and retaining the analyser gave rise to a zero-order spot, but polarisation changes at the source still affected the output intensity. With the polariser in place but with the analyser removed, there was a variable coupling effect between the power in the central spot and in the diffracted spots. These observations are completely validated

by the theory.

In many systems, the existence of an undiffracted zero-order can simply be ignored, provided the holograms direct light away from the axial position. In these architectures, the zero-order may even serve a useful function and become an indicator of the instantaneous optical power incident on the system, i.e., ignoring any other losses, the zero-order constantly receives a $(1 - \eta_s)$ fraction of the input power. The undiffracted spot may also be used to indicate the position of the optic axis and therefore be used for automatic (and possibly adaptive) system alignment.

3.2 The One-to-Any Single-Mode Fibre Switch

The simplest architecture utilising FLC holograms to dynamically route optical signals between single-mode fibres is shown schematically in figure 3.4. Conceptually this system is similar to a one-to-all single-mode fibre fan-out coupler [67] that has been demonstrated using a fixed etched glass hologram. By replacing the fixed CGH with a FLC device, a one-to-*any* dynamic fibre-switch may be constructed which includes multicast (one-to-several) and broadcast (one-to-all) capability through appropriate CGH design.

The optical signal from the single-mode input fibre is collimated by a lens to give a TEM_{00} beam profile. This fibre is aligned along the optic axis of the system so that the beam passes

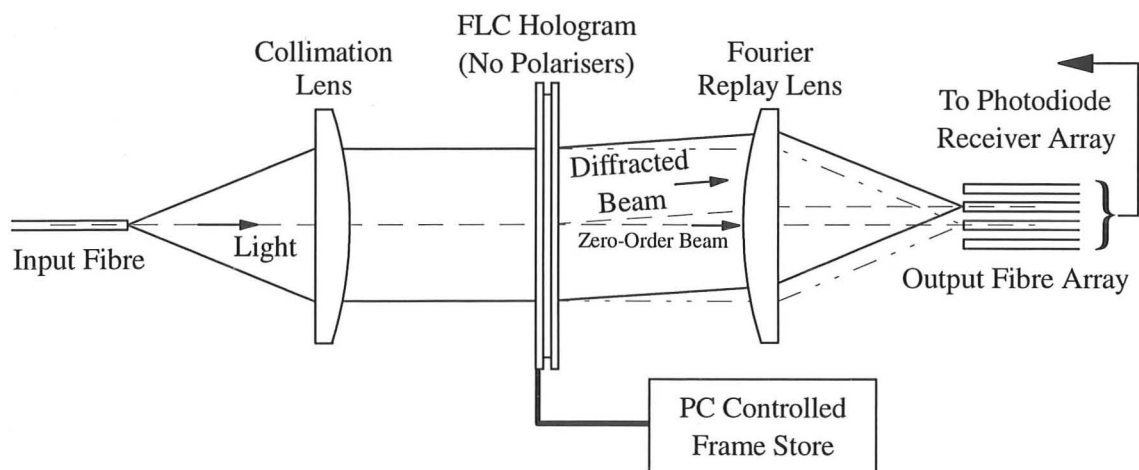


Figure 3.4: One-to-any fibre switching experiment.

perpendicularly through the FLC modulator, which does not have polarisers. The FLC device displays one frame from a set of phase CGHs which have been calculated off-line at an earlier stage and placed in a frame store to be recalled on demand. Ignoring aperture losses and stray glass reflections which can be minimised during the optical design procedure, all of the optical input power arrives at and is distributed around the output plane by the replay lens. The exact distribution of light in this focal plane and therefore the efficiency of the switch, is determined by the far-field replay (the spatial Fourier transform) of the displayed hologram frame. In the absence of lens wavefront aberrations, the Fourier flat-phase condition is met in the replay field by ensuring that the two lenses have the same focal length and that the system is a symmetric $4-f$ relay. Single-mode fibre launch conditions are then satisfied and the FLC device can be used to selectively diffract the optical signal into the output single-mode fibres. These fibres are aligned parallel to the optic axis such that their cleaved faces lie in the replay plane and are preferably arranged in a 2-dimensional array. Which fibre receives the optical signal is determined by the displayed CGH frame.

3.2.1 *Experimental 1-to-2 fibre switch*

An initial proof-of-principle investigation was performed on a 1-to-2 fibre switch. The experimental setup was similar to the one used to generate figure 3.3(b). To match the output spot size to the TEM_{00} fibre mode, the replay lens was replaced by an $f = 125\text{mm}$ achromat lens, identical to the one used for collimation. The CCD camera in the output plane was replaced by two cleaved $\lambda = 633\text{nm}$ single-mode fibres mounted on separate mechanical positioning stages. Both outputs were positioned off-axis to avoid the zero-order and the switch was used to route the input to either, both or neither of the fibre outputs.

The switch exhibited a 13.8dB insertion loss and a -35dB crosstalk isolation between the two output channels. The insertion loss included a fibre-to-fibre coupling efficiency of -3.1dB, which also accounts for reflections and wavefront aberrations from all glass surfaces. The theoretical CGH diffraction efficiency was -4.1dB taking account of all non-zero diffraction-orders and the $5\mu\text{m}$ interstitial dead-space between the square SLM pixels. The remaining 6.6dB loss was due to the amount of undiffracted zero-order generated by this SLM.

The spatial resolution of the SLM hologram display device determines the extent of the replay plane to which the outputs should be confined. This 'first-order' diffraction region

has the same shape as the SLM aperture (i.e., square), is centred on the zero-order axis and is described by:

$$\text{Width of first-order} = \frac{f\lambda}{d}, \quad \text{Holographic replay resolution, } \Delta x_r = \frac{f\lambda}{Nd} \quad (3.11)$$

where d is the SLM pixel pitch, N is the number of pixels across the SLM width and f is the focal length of the replay lens. The holographic replay resolution is the smallest displacement of a replay spot that may be achieved throughout the first-order by display of a different hologram. It is independent of the Gaussian spot diameter.

The number of output channels that can be supported by a one-to-any switch is usually limited by the physical size of the first-order, rather than by the simulated signal-to-noise ratios of the hologram replays. In a symmetric Gaussian relay-based architecture, the design focal length f needed to achieve best utilisation of the hologram, is determined by the fibre mode radius and by the hologram clear aperture:

$$f \simeq \frac{1}{2}D \cot\left(\frac{\lambda}{\pi w_o}\right) \quad (3.12)$$

Equation (3.12) represents the best compromise between adequately illuminating the entire hologram, and retaining as much Gaussian light power as possible through the SLM aperture. The value of the bracketed expression is virtually independent of wavelength for any single-mode fibre. Thus for a given aperture $D = Nd$ and wavelength λ , the number of switch outputs that may be supported within the first-order replay area of equation (3.11) can be increased only by reducing the distance between the outputs, or by improving the space-bandwidth product of the SLM. The first condition implies that it is desirable to pack the output fibres as closely together as possible, although this will also have an effect on the system crosstalk. The latter condition is achieved by increasing the number of SLM pixels and reducing their pitch. Hence it is an important technological advantage that applying a diffractive optics approach in a telecommunications environment ($\lambda = 1.55\mu\text{m}$) automatically creates a replay area, and therefore a switching ability, at least 6 times larger than a similar system designed at shorter visible wavelengths.

3.2.2 Experimental 1-to-15 fibre switch

A much more substantial investigation of a larger 1-to-15 switch has also been performed. The experimental system was based around a Thorn CRL 2DX320 device which is a passively

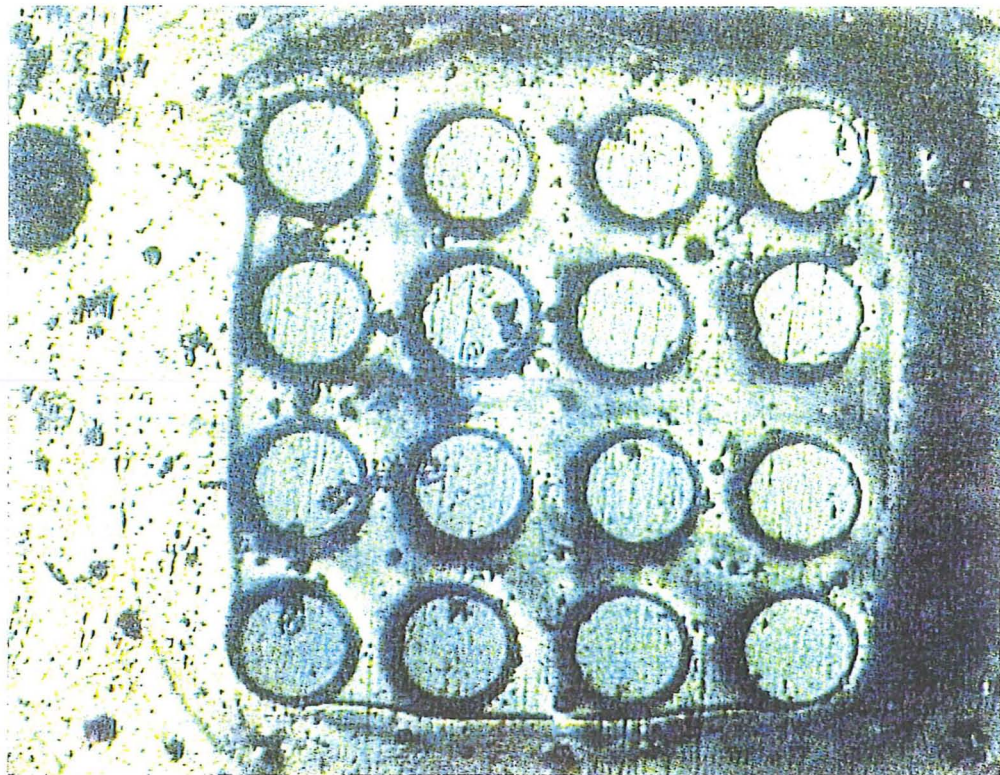


Figure 3.5: Microscope image of the 4x4 single-mode fibre array.

multiplexed transmissive SLM similar to the 2DX128, again relying on the bistability of the liquid crystal with which it has been filled. This more advanced device has 320x320 ferroelectric pixels and has been manufactured with $\simeq 2\mu\text{m}$ spacers, $80\mu\text{m}$ pixel pitch and $5\mu\text{m}$ dead-space gaps. The 2DX320 therefore generates a larger replay field than the 2DX128.

With an increased number of outputs, the use of individual positioning stages for each fibre becomes highly impractical. The outputs must now be mounted in a specially constructed fibre array. The array used here was an experimental component manufactured at British Aerospace's Sowerby Research Centre by drilling slightly tapered holes in a kevlar plate with an excimer laser, then manually inserting cleaved fibre ends [68]. It consists of 16 fibres arranged on a 4x4 square grid with a $200\mu\text{m}$ pitch. These fibres are non-polarising and single-moded at near infrared wavelengths (around $\lambda = 780\text{nm}$), have a $125\mu\text{m}$ glass cladding diameter and a guided-mode field radius of $w_o \simeq 2.8\mu\text{m}$. Figure 3.5 shows the geometry of this array when observed through a microscope. The outer cladding diameters of the fibres can be clearly seen.

The input fibre source was provided by a 0.25mW, 780nm fibre-pigtailed semiconductor laser, amplitude modulated by a square-wave at about 1kHz. The collimation and replay lenses used were identical Spindler & Hoyer achromats with 140mm focal length and 40mm diameter. These lenses illuminated the 25.6mm usable SLM aperture with a 24.7mm diameter ($\frac{1}{e^2}$ intensity) Gaussian beam and produced a 1.36mm first-order replay field. This field size is large enough to cover the entire output fibre array area.

Switching of the optical signal to different outputs was observed using electronic receivers. The trailing fibre ends at the back of the array were extended with fibre splices and light out of the new cleaved fibre ends was collected by an array of lensed BPX65 silicon photodiodes [69]. These photodiode receivers drove an LED array by means of transimpedance amplifiers followed by comparators. Any lit LED indicated that its corresponding output fibre was receiving the optical signal.

In order to locate the replay plane and to correctly position the kevlar plate within this plane, one of the four central array fibres was aligned along the system optic axis and its position was optimised to receive the undiffracted zero-order beam. This fibre was used to calibrate the optical system. With a blank hologram frame on the SLM, a figure of 6dB was obtained as the insertion loss contribution due to the optical surfaces. This experimental value includes optical absorptions, stray glass reflections, Gaussian beam aperturing, the effects of SLM dead-space, the fibre-to-fibre coupling efficiency across the switch, defects on the surfaces of the cleaved array fibres (see figure 3.5), the fibre splice loss, and the fibre-to-photodiode coupling efficiency.

Fibre 10,[†] the axial fibre, was also used for re-alignment of the optics after thermal or mechanical drift — the switch was demonstrated and performed over a period of several weeks and suffered daily environmental thermal cycling. The worst loss of alignment during this period was less than 6 μ m and optimisation of the on-axis fibre launch was used to return all other output fibres to their original positions.

Slight irregularities in the fibre array pitch meant that the 15 remaining fibre locations in the replay plane had to be experimentally determined. This was achieved by rapidly displaying SLM hologram frames to raster scan a replay spot about a 9x9 grid in the expected vicinity of each fibre core. The pitch of this grid was the holographic replay resolution of

[†]Refer to the fibre numbering key of figure 3.6

$\Delta x_r = 4.28\mu\text{m}$ and the search goal was to find a fibre mode of diameter $2w_o \simeq 5.6\mu\text{m}$. Each fibre core location was then determined from the hologram frame that maximised the optical signal reaching the corresponding photodiode receiver. In 2-dimensions, the worst case error between this holographically determined position and the true core location will be $\frac{1}{\sqrt{2}}\Delta x_r$.

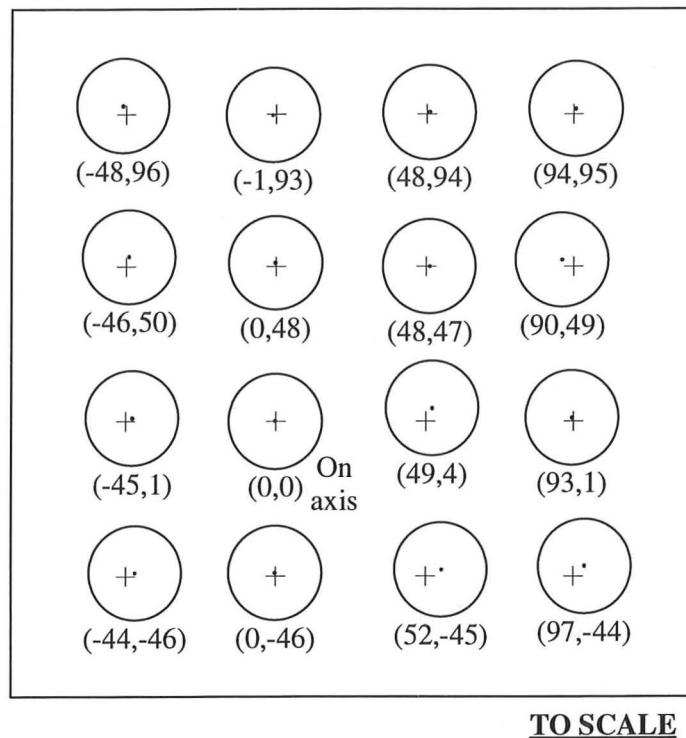
The results of this scanning search, superimposed onto the expected locations given a perfect $200\mu\text{m}$ pitch array, are shown in figure 3.6. These results can be directly compared with the visible positional irregularities in figure 3.5. Although this scanning process is somewhat laborious, future characterisation of fibre arrays could easily be automated by feeding the photodiode signals back to the hologram frame store controller. Once the switch is operational, this technique could also be used as an adaptive method of maintaining a fibre launch in the presence of low frequency vibrations or other disturbance.

Figure 3.7 is a photograph of the experimental switch layout on an optical bench. The components that can be seen in this photograph are:

- (1). Input fibre mount,
- (2). Collimation lens,
- (3). 2DX320 spatial light modulator,
- (4). Replay lens,
- (5). Back view of fibre array,
- (6). Fibre splices to photodiode array,
- (7). Alternative CCD monitor output, activated by insertion of a beam splitter after the SLM,
- (8). Modulated semiconductor laser source.

Once the required set of 15 holograms had been determined, the switch was configured to direct the optical signal into each array fibre in turn and the received power was plotted against the output fibre number, figure 3.8. For comparison, a simulation curve of the expected loss is also plotted. The experimental readings were all taken using the same photodiode to eliminate schematic errors and the results were normalised by continuously monitoring the axial fibre for variations in the level of optical power from the source.

Just less than half of the total insertion loss of the experimental system can be attributed to the poor phase efficiency of the 2DX320. This is partly due to operation at an incorrect wavelength (780nm instead of 633nm), but mainly occurs because of the very low effective FLC tilt angle of the proprietary material used in the device. The effective molecular tilt of an FLC material can depend on the operating conditions. In this SLM, the need to passively address and multiplex 320 rows of image data at a reasonable frame rate, and the image



KEY

- Experimentally determined fibre core positions
- 125µm fibre cladding diameter
- + Expected fibre core positions (200µm pitch)
- (x,y) Fibre core coordinates, in holographic units (1 unit = smallest resolvable displacement)

Fibre Numbering Scheme

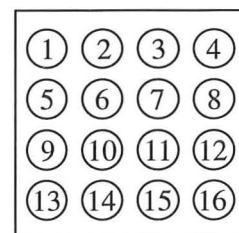


Figure 3.6: Single-mode fibre locations.

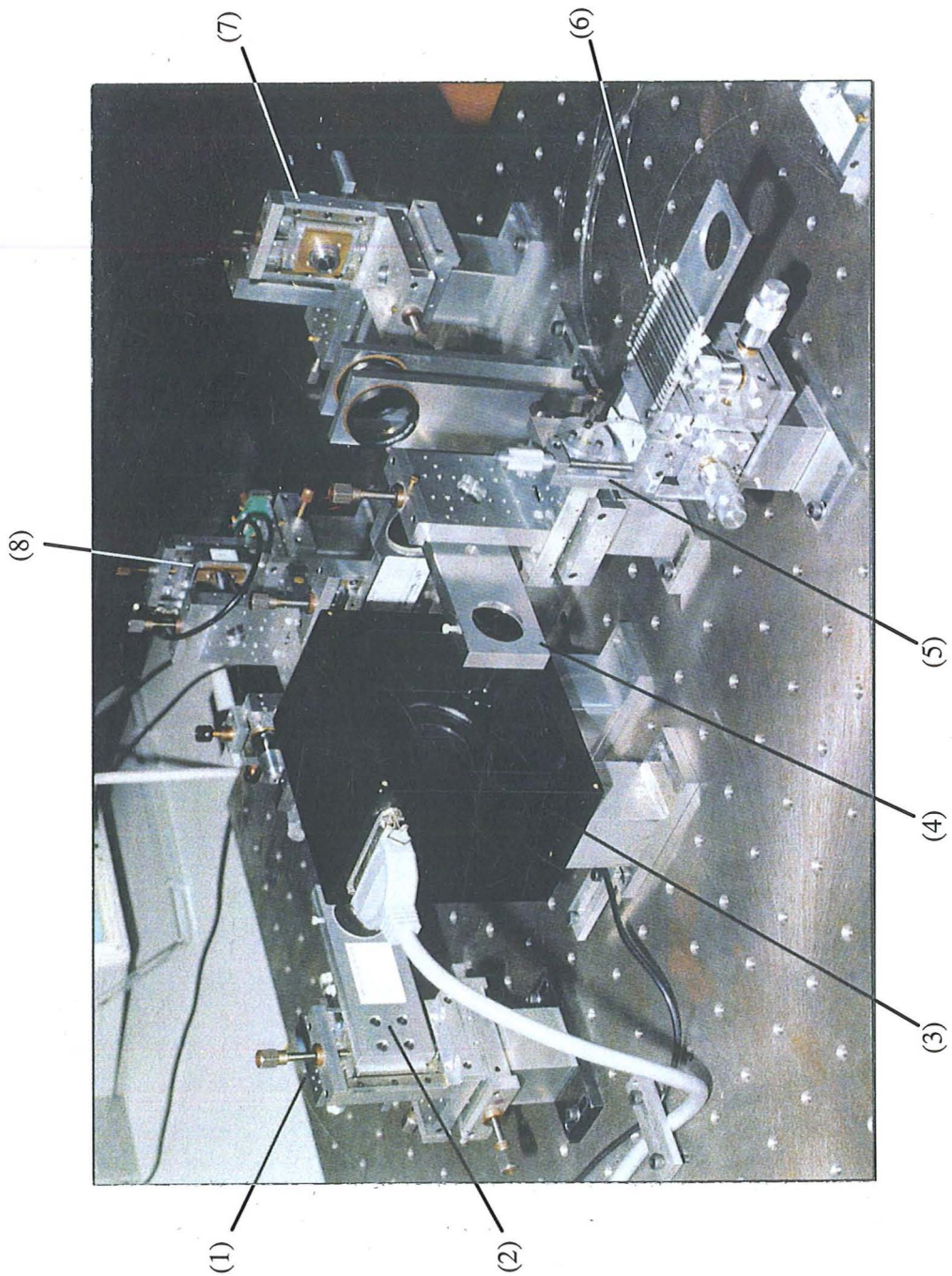


Figure 3.7: Photograph of the 1-to-15 experimental setup.

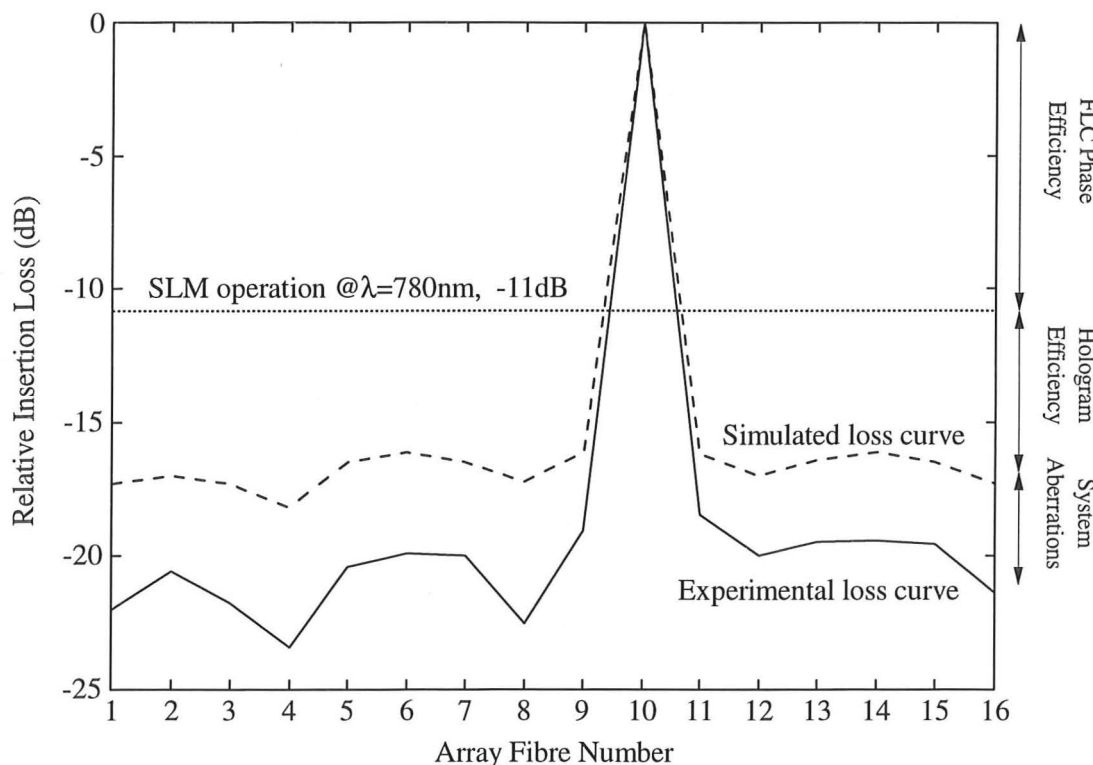


Figure 3.8: Normalised experimental insertion loss.

crosstalk between rows that this causes, means that the optical modulation properties have been compromised. An actively addressed backplane device would not suffer this constraint.

In a separate experiment, the 2DX320 liquid crystal switching angle was measured. The SLM was illuminated with circularly polarised light from a continuous-wave laser and a blank frame was displayed. Following the SLM, the light passed through a motorized rotating linear polariser. The transmitted optical power was detected by a photodiode and the received power signal was displayed on an oscilloscope. With an experimental setup of this type, it is found that the birefringence of the FLC material within the SLM distorts the circular polarisation state of the input and generates a sinusoidal power trace at the output. By synchronising the start of the oscilloscope trace to each motor revolution, and by switching the entire display between its two states, the phase of the sinusoid jitters between two values and the effective FLC tilt angle θ is calculated as $\frac{1}{4}$ of the observed phase-shift. This calculation is independent of the FLC cell thickness and can therefore be performed at any wavelength. The sinusoidal peak-to-peak amplitude does however become

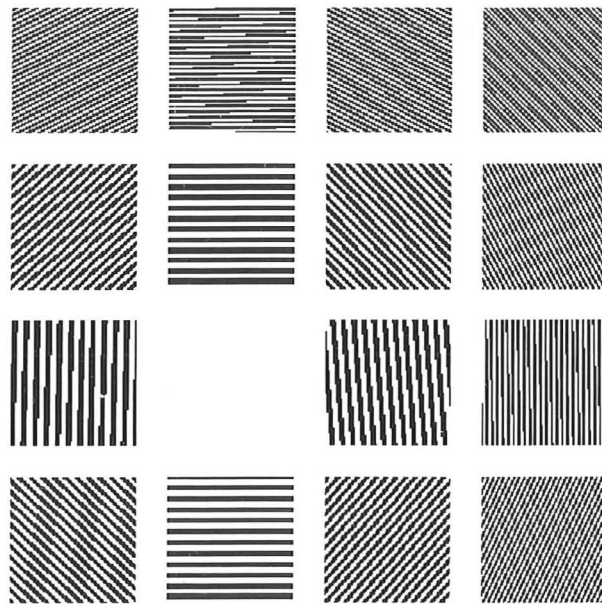


Figure 3.9: Hologram set for the 1-to-15 fibre switch experiment.

very small near to the SLM design wavelength and for accuracy, this spectral region should be avoided. For the 2DX320, the switching angle 2θ was found to be only 17.4° . The measured performance of the 1-to-15 switch could therefore be radically improved through use of a different SLM with a better FLC diffractive phase-efficiency.

Figure 3.9 shows 80x80 pixel portions from each of the 16 switch holograms. The Gerchberg-Saxon algorithm [52] was used in the design of these holograms, rather than simulated annealing, because of the very large number of CGHs that had to be generated during the array scanning procedure. The Gerchberg algorithm is based on the imposition of constraints upon the hologram function and its Fourier transform replay, and it relies upon iteration between these two functions. The algorithm typically converges to a solution considerably faster than simulated annealing, but provides less control over noise in the final replay field. Hence the holograms that were used experimentally are essentially grating-like and exhibit greater diffraction losses than the more complex patterns that an optimised annealing technique would generate. Simulations of the hologram efficiencies are shown as a dashed line in figure 3.8.

A discrepancy of several dB can be seen between the FFT computer simulated losses and the experimentally determined insertion losses in figure 3.8. The differences are almost

certainly due to additional system aberrations which could be largely eliminated by careful lens designs and alignment procedures. The extra loss is probably a culmination of effects including optical scattering from FLC alignment defects, changes in the SLM phase efficiency caused by thermal changes to the electrical operating conditions, and replay wavefront phase errors introduced by the two lenses which were intended to be used with visible light. The discrepancy appears to increase with the distance of each fibre from the optic axis. This suggests that small amounts of coma and/or astigmatism (imperceptible to a CCD camera without the use of magnifying optics) are present in the replay field. These Seidel aberrations would not affect the axial spot and are thus not accounted for by the original -6dB calibration figure. However the other fibre launches would be very sensitive to these distortions. Evidence for this theory was found when determining the core coordinates of fibre 4 which is furthest from the optic axis. It was observed that there were several holographic replay positions within the 9x9 scanning region that gave photodiode readings of similar magnitude. These adjacent grid points were roughly in a direction radially extending from the axial position, implying that the entire replay field had a 'star-field' distortion.

3.3 Diffraction Efficiency Limitations of FLC Switches

The spatial Fourier transform relationship between a hologram and its replay means that perfect arbitrary replay fields can never be generated without the existence of continuous-phase, non-sampled and infinitely large SLMs. Practical electrically-addressed FLC devices are currently limited to two phase states, must be pixellated and have a finite aperture and space-bandwidth product. A close approximation to the desired replay can usually be obtained, but quantization of the hologram's phase and spatial properties means that some optical power inevitably leaks into parts of the replay field as extra output peaks and/or a low-intensity background noise. The quantization effects not only reduce the efficiency of the system but also create unwanted crosstalk noise in the switch by reducing the output contrast ratios. The resulting diffraction efficiencies and signal-to-noise ratios of realisable holograms can only be partially predicted without full FFT-based simulation because deviations from the ideal replay depend largely upon the method and criteria used during the iterative generation of each hologram. But some useful theoretical efficiency limits can still be derived. These limits apply to the diffraction efficiency of binary $(0, \pi)$ phase holograms. It has been assumed that the FLC diffractive phase-efficiency loss due to imperfect phase modulation is an independent factor which can be accounted for separately by η_s .

3.3.1 Inversion symmetry from binary phase holograms

The diffraction efficiency η_h of a hologram or grating is the amount of optical power that replays exactly as desired, expressed as a ratio of the total power available. It may be mathematically defined as:

$$\eta_h = \frac{\iint_T I_T(x, y) \left| \mathfrak{F} \left[CGH(X_m, Y_n) \right] \right|^2 dx dy}{\iint_{-\infty}^{\infty} \left| \mathfrak{F} \left[CGH(X_m, Y_n) \right] \right|^2 dx dy} \quad (3.13)$$

where $I_T(x, y)$ is a normalised representation of the target (i.e., the ideal) replay intensity distribution. The phase states in a binary $(0, \pi)$ hologram may be represented entirely by ± 1 's, so the hologram is a *real* function in the mathematical sense rather than a complex one. Therefore it follows that:

$$r(x, y) = \mathfrak{F} \left[CGH(X_m, Y_n) \right] = \mathfrak{F} \left[CGH^*(X_m, Y_n) \right] = r^*(-x, -y) \quad (3.14)$$

A consequence of (3.14) is that the 2-dimensional replay intensity $|r(x, y)|^2$ is always constrained to be rotationally symmetric about the zero-order:

$$|r(x, y)|^2 = |r(-x, -y)|^2 \quad \text{and} \quad |r(x, -y)|^2 = |r(-x, y)|^2 \quad (3.15)$$

Half of the replay field will be in position as required, whilst a second conjugate-phase copy will always appear rotated by 180° about the system axis. If a rotationally symmetric replay pattern such as the 4x4 spots of figure 3.3(b) is required, this property of binary holograms will generally result in a very high CGH diffraction efficiency. But in a diffractive optical switching environment, typically a unique one-to-one connection is wanted and the replication of the target replay field due to the inversion symmetry represents a waste of optical power and replay area.

For every output spot that is generated, a second spot must also appear, diametrically opposed across the optic axis. Although the symmetric-order may be used in some circumstances to monitor the switch routing configuration, there is little possibility of recombining the two orders because they will tend to interfere coherently. This unfortunately places an upper limit of 50% on the diffraction efficiency of any binary-phase hologram (25% limit on any binary-amplitude hologram). In addition, the need to avoid unacceptably high levels

of crosstalk leads to either the reservation of the symmetric half of the output plane as unusable — the output fibres must be confined to only half of the first-order — or a need for irregular placement of the output fibres. In the latter case, all possible positions of the inversion symmetry peaks might be avoided by constructing the fibre array with non-redundant centre-to-centre spacings. The spacings might be based on prime numbers, for example. A similar variation is discussed theoretically in [70], where prime numbers have been applied to the effective hologram pitch rather than to the fibre spacings. Experimentally this system would be able to support far fewer outputs than allowed for by a non-restricted CGH set. The method is suggested as a means of precisely controlling the hologram quantization noise by restricting the hologram set to ‘perfect’ gratings, but evidence is presented later that suggests that the system crosstalk is limited by coherent scatter noise from inhomogeneities in the FLC recording medium, rather than by the hologram designs.

Although it was impossible to accurately determine the system crosstalk in the 1-to-15 experiment because of the limited source power available, the fibre array irregularity actually helped in preventing crosstalk between the outputs, e.g., the fibre positional errors prevented a significant signal launching along fibre 15 when it was intended for fibre 5. Alternatively, one of the corner fibres within the array could have been chosen as the zero-order launch and all the inversion symmetry spots would then have been incident upon the kevlar plate, away from the immediate vicinity of the 15 outputs.

The only method of breaking the symmetry of a diffractive optical element is to effectively ‘blaze’ it by introducing additional phase levels, hence forcing the hologram function $CGH(X_m, Y_n)$ to become complex-valued. Although it is possible to generate four-levels of phase $(0, \frac{\pi}{2}, \pi, \frac{3\pi}{2})$ using a combination of two distinct FLC-SLM devices in conjunction with a waveplate [71–73], the alignment and control of such a system is difficult, typically requiring extra lenses to image one device onto the other. Fast multi-level FLC phase modulators as single components are still to be developed, but some possible methods of achieving asymmetric replays are discussed briefly in chapter 6.

3.3.2 *Effects of hologram pixellation and dead-space*

The replay spot of an FLC hologram can be placed anywhere within the first-order diffraction region of the switch output plane. The inversion symmetry must also lie within this area. Except in situations where the optical signal is to be multi-cast to several outputs, ideally

these would be the only two spots in the entire replay plane. Unfortunately, the phase boundaries that exist between adjacent hologram pixels, tend to force power into multiple diffraction-orders. The Gaussian spots that are generated within these higher-order regions are outside the central first-order replay and cannot therefore contribute any crosstalk noise. But they further limit the efficiency performance of diffractive switch technology.

All SLMs must have some amount of dead-space between their pixels. The exact effect of this dead-space in a particular FLC device is difficult to quantify because the manufacturing process may introduce surface irregularities along the pixel edges and because the applied pixel voltages tend to generate curved fringe-fields across the inter-pixel areas. The dead-space characteristics directly affect the redistribution of optical power from the first-order replay to the higher-order diffractions. So by assuming that the dead-space areas do not transmit light, it is possible to calculate a theoretical upper bound for the first-order diffraction efficiency of any binary phase hologram.

For generality we assume that the SLM pixels are rectangular and have an x -directional pitch of d_x and a y -directional pitch d_y . The active modulation area of each pixel may be represented by an aperture function:

$$Rect(a_x, a_y) = \begin{cases} 1 & \text{for } -\frac{a_x}{2} \leq x \leq \frac{a_x}{2} \quad \text{and} \quad -\frac{a_y}{2} \leq y \leq \frac{a_y}{2}, \\ 0 & \text{elsewhere.} \end{cases} \quad (3.16)$$

such that the dead-space widths are $(d_x - a_x)$ and $(d_y - a_y)$ in the x, y directions respectively. The SLM consists of an array of such pixels as shown on the left-hand side of figure 3.10. The phase state of each pixel is contained within $CGH(X_m, Y_n)$. This is a discrete function which corresponds to a normalised array of weighted ± 1 delta functions, each delta positioned at the centre of a single pixel. A full representation of the pixellated SLM structure can only be provided by the continuous hologram function $CGH(x, y)$, obtained by convolution of the discrete function with the pixel aperture:

$$\begin{aligned} \mathfrak{F}[CGH(x, y)] &= \mathfrak{F}[CGH(X_m, Y_n) * Rect(a_x, a_y)] \\ &= r(x, y) \times Env(x, y) \end{aligned} \quad (3.17)$$

Equation (3.17) reveals how the replay plane is affected by the pixel apertures. The spatial quantization of the hologram causes the replay plane to expand into an infinite number of

replay orders. $|Env(x, y)|^2$ is an envelope function which weights the intensity of the replay plane across all these diffraction-orders:

$$|Env(x, y)|^2 = \left| \mathfrak{F} \left[Rect(a_x, a_y) \right] \right|^2 = \left(\frac{a_x}{d_x} \text{sinc} \left[\frac{\pi a_x}{f\lambda} x \right] \times \frac{a_y}{d_y} \text{sinc} \left[\frac{\pi a_y}{f\lambda} y \right] \right)^2 \quad (3.18)$$

The right-hand side of figure 3.10 shows the shape of this envelope for an 88% pixel fill-factor, 12% dead-space area. The plot shows an expanded view of the diffraction envelope across three replay orders. Only one quadrant of the output plane is displayed, such that the main peak at the top of the plot intensity-weights the first-order replay field. It can be seen that although the sinc envelope falls to zero intensity within the second-orders, it ripples back up again in the third- and does so again in higher-orders.

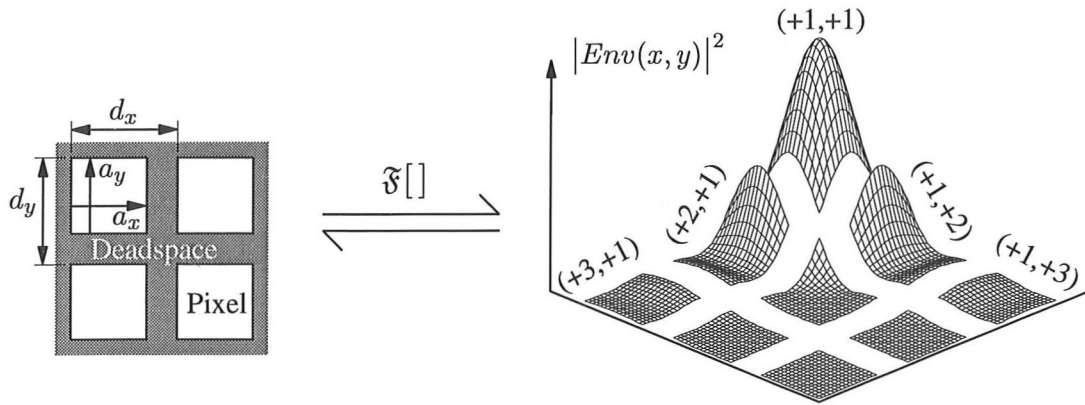


Figure 3.10: Intensity envelope across the replay diffraction-orders.

Pixellation of the SLM means that the pattern of spots within the first-order replay field $r_{1st}(x, y)$, is replicated in all other orders. This forms the complete replay plane image which is then appropriately weighted by the diffraction intensity-envelope. From equation (3.11), the first-order has a width of $\frac{f\lambda}{d}$ and is centred about the optic axis. Hence:

$$r(x, y) = r_{1st}(x, y) * \sum_{p=-\infty}^{\infty} \sum_{q=-\infty}^{\infty} \delta \left(x - \frac{f\lambda}{d_x} p, y - \frac{f\lambda}{d_y} q \right) \quad (3.19)$$

Temporarily neglecting the hologram inversion symmetry and assuming that the FLC phase-efficiency loss has been accounted for separately, an ideal hologram for optically intercon-

necting fibres would only generate a single interconnect spot. If there is no additional replay noise, then only this single perfect replay peak and its higher-order replications remain in the replay field. The first-order spot may be defined to be positioned at a fractional-order coordinate (σ, ξ) relative to the optic-axis:

$$r_{1st}(x, y) = \begin{cases} 1 & \text{at } x = \sigma \frac{f\lambda}{d_x}, \quad y = \xi \frac{f\lambda}{d_y}, \\ 0 & \text{elsewhere.} \end{cases} \quad (3.20)$$

$$\text{where } |\sigma| \leq \frac{1}{2} \text{ and } |\xi| \leq \frac{1}{2}$$

The replay field contains a Gaussian in reality, but with the same integrated optical power as this delta function. Also (σ, ξ) are not continuous variables because they are governed by the replay resolution of equation (3.11). The optical distribution in very high diffraction orders will also become distorted by lens aberrations and by the breakdown of the paraxial diffraction integral, but this will not affect the current analysis which is only concerned with the first-order replay efficiency. The optical power diffracted by the CGH can be appropriately normalised and distributed between the various replay orders by substituting expression (3.20) into (3.19) and applying the envelope function of (3.18). The integrated power in all replay orders is then equal to the optical power transmitted through the SLM. Because light is only transmitted by the active pixel modulation areas, it follows that:

$$\sum_{p=-\infty}^{\infty} \sum_{q=-\infty}^{\infty} \left(\frac{a_x}{d_x} \text{sinc} \left[(p + \sigma) \frac{\pi a_x}{d_x} \right] \times \frac{a_y}{d_y} \text{sinc} \left[(q + \xi) \frac{\pi a_y}{d_y} \right] \right)^2 = \frac{a_x a_y}{d_x d_y} \quad (3.21)$$

Equation (3.21) is true for all values of σ and ξ and it accurately represents the distribution of power between an infinite number of diffraction-orders. The upper bound on holographic efficiency is found by examining the intensity of the principal replay spot. This spot is located in the central $p = q = 0$ order. To tidy the final result, we might assume that practical SLMs of interest have perfectly square pixels, such that their diffractive efficiency is:

$$\eta_h = \mathcal{T}^4 \text{sinc}^2 \left[\sigma \pi \mathcal{T} \right] \text{sinc}^2 \left[\xi \pi \mathcal{T} \right] \quad (3.22)$$

$$\text{where } \mathcal{T} = \frac{a_x}{d_x} = \frac{a_y}{d_y}$$

The above analysis predicts that even a blank hologram frame will suffer some diffraction of power into higher replay-orders when dead-space is present. This is easily verified by looking

at the pattern of replay spots generated by a pixellated mirror in coherent light. The zero-order reflection receives most of the power, but a grid of regularly spaced replications is also present, most visibly along the x - and y -axes. From equation (3.22), a diffraction efficiency of 100% can only be achieved when the hologram has no dead-space (i.e., $\mathcal{T} = 1$) and when the replay spot is located on the optic axis, i.e., $\sigma = \xi = 0$. This only occurs in the rather trivial situation when the CGH-SLM is actually removed.

Hologram diffraction efficiencies are proportional to \mathcal{T} to the fourth power. This means that an increased amount of dead-space as a fraction of the pixel pitch rapidly compromises the effectiveness of the SLM as a diffractive element. The $80\mu\text{m}$ pitch, $5\mu\text{m}$ dead-space of the 2DX320 represents a $(1 - \mathcal{T}^2)$ dead-space area of 12%, and produces a theoretical maximum efficiency of $\mathcal{T}^4 = -1.12\text{dB}$, followed by a further 3dB loss due to the inversion symmetry. The detrimental effects of dead-space are particularly significant when miniaturised SLMs are integrated on top of silicon circuits. The pixel pitches have to shrink as the number of pixels increases, but the minimum dead-space gap is limited by the lithographic resolution of the process used to pattern the SLM. A theoretical silicon device manufactured using a $2\mu\text{m}$ lithography process and having a $10\mu\text{m}$ pixel pitch introduces a much larger minimum loss of $3.88\text{dB} + 3\text{dB}$. This device would waste over half of the optical power in dead-space absorption and high-order diffraction replications.

Figure 3.11 is a plot of the upper bounding efficiency η_h for 2DX320 binary phase holograms, taking account of the inversion symmetry. The horizontal axis displays the radial displacement $\sqrt{\sigma^2 + \xi^2}$ of the principal first-order replay spot from the zero-order. Equation (3.22) isn't quite a polar function and this can be seen by the slight line thickening around the centre region of the plot where there are multiple points. The curve has a discontinuity at the \mathcal{T}^4 on-axis peak and two others at 0.5 and 0.71. These two peaks correspond respectively to the principal replay spot being positioned at an edge-centre of the (square) first-order replay field, or in a corner of the first-order. At these positions, the replay spot merges with the inversion symmetry of the next highest order. This also occurs in all the replication fields, hence doubling the local diffraction efficiency.

A multi-phase hologram would have a doubled theoretical efficiency at all displacements, without the discontinuities of figure 3.11. Despite the considerable technological effort required to minimise the dead-space wastage and to introduce extra phase levels to break the inversion symmetry, only a relatively modest increase in diffraction efficiency is ever

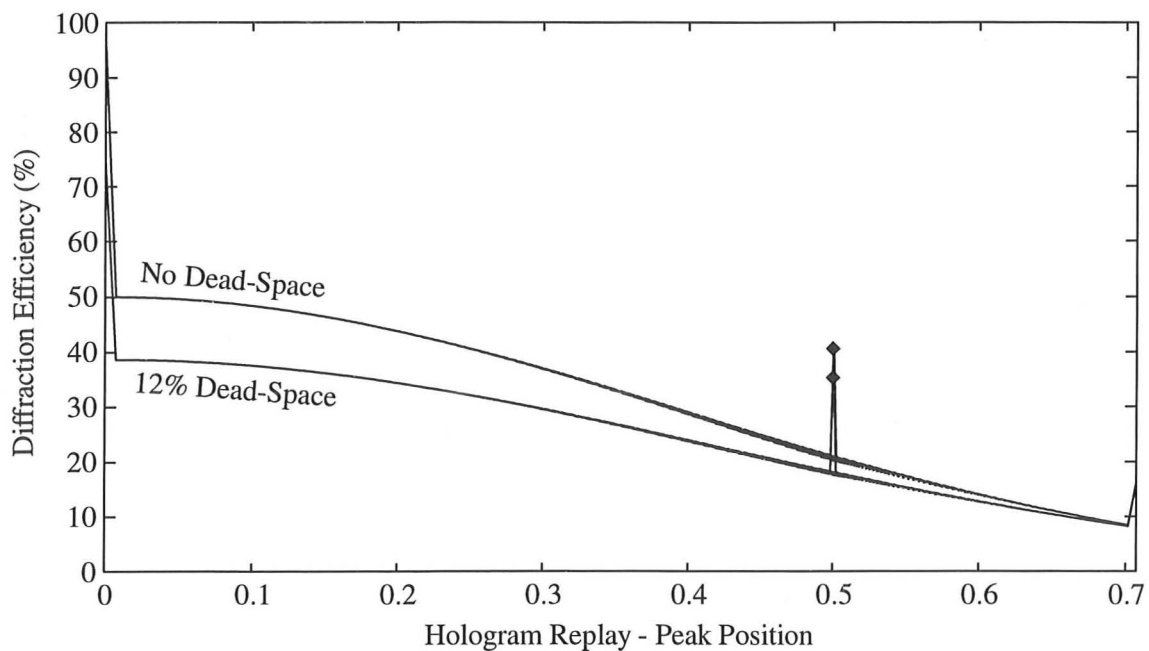


Figure 3.11: Theoretical bound on binary hologram efficiency.

possible. The generation of 'power-hungry' high-order diffractions is the main factor that limits the eventual performance of FLC diffractive switches.

Equation (3.22) is verified at $\sigma = \frac{1}{2}$ and $\mathcal{T} = 1$ by Dammann's analysis of 1-dimensional stepped grating structures [74]. For arbitrary binary phase holograms, the efficiency will not generally reach the theoretical limit plotted in figure 3.11 because of the presence of extra quantization peaks in the replay. The effects of this noise typically reduce the actual efficiency to about 70-80% of η_h .

In real SLMs, the dead-space will probably not block out light, but will rather transmit it without any phase modulation. Provided there are no scattering features recorded in the dead-space FLC, the extra transmitted power can only be diffracted into the on-axis zero-order and into the central points within all higher-orders. Under these circumstances, the dead-space cannot contribute any replay crosstalk noise. In an operational device, the liquid crystal above the dead-space may even partially switch according to the average state of surrounding pixels, but this is by no means guaranteed and it will probably not occur throughout the entire pixel array.

3.4 Crosstalk

Crosstalk in an optical network is caused by one or more of the data signals cross-coupling power into other signal paths. If the transmitted data sequences are independent and do not exhibit any cross-correlation, then the total crosstalk in any path may be modelled as a source of random noise with some probability density distribution. This noise directly affects the mean optical signal-to-noise ratios (SNRs) and hence ultimately degrades the bit-error-rate performance at the data receivers. The network bit-error-rate typically depends upon a number of different parameters other than just the optical SNR. The layout of the network; whether optical amplification or regeneration is used; the sensitivity of the receivers; and the type of data transmitted will all have contributions. It is most convenient however, to describe the performance of any optical switch architecture and in particular, how many switching nodes might be traversed before regeneration of the signal is necessary, in terms of the optical SNR found at any of the switch output ports.

Crosstalk in a diffractive optical switch can be caused by overlap of the 'infinite' Gaussian output tails and by the non-ideal beam steering efficiency of the CGH-SLM. The high degree of spatial repetition and therefore inherent redundancy within the patterning of holograms makes them very robust against pixel faults and can lead to excellent theoretical crosstalk isolation. But in practical situations, non-uniformities within the SLM structure and binary-phase quantization effects inevitably cause some of the optical power to be coherently scattered around the replay. Even 'perfect' gratings (i.e., $\sigma = \frac{1}{2}, \frac{1}{4}, \frac{1}{6}$, etc.) suffer from diffraction noise in practice. This noise is ultimately the limiting crosstalk factor.

Photo-detectors and large numerical aperture multi-mode fibres are efficient devices for collecting all incident power within a finite aperture. If these devices are used as the switch output ports then the optical SNR is simply the contrast ratio averaged across the output aperture, i.e., the integrated optical intensity received when a data signal is being routed to that particular output, divided by the mean integrated noise power when the signal is being routed elsewhere. But when the switch output ports are single-mode fibres or are only just multi-moded, then more attention must be made to calculation of the output SNR. Only incident light that matches the fibre's guided-mode profile will be accepted into the fibre. Any mismatched optical field may initially enter the fibre but will then tend to exit through the cladding after propagating only a short distance. To analyse the switch SNR with single-mode fibre outputs, we must compare the relative fibre coupling efficiencies of

the signal launch and of the crosstalk noise.

3.4.1 Replay phase-profiles and the overlap integral

The field emitted from a cleaved single-mode fibre is a precisely defined TEM_{00} Gaussian. By the argument of reciprocity of light, the launch mode from free-space back into a single-mode fibre must be an identical TEM_{00} . Distortion to either the intensity- or the phase-profiles of the beam will have an adverse effect upon the fibre launch efficiency. If fibre-to-fibre routing is to be attempted then the issue of phase-profile across the output beam becomes very important. The replay spots must always be matched to the guided-mode of the fibre.

The overlap integral (3.23) takes account of the complex optical field profile of the replay plane and may be used to calculate the power efficiency with which replay spots or unwanted crosstalk noise will launch down single-mode fibres.

$$\eta_o = \frac{\left| \iint r(x, y) \tilde{E}_f(x, y) dx dy \right|^2}{\iint |r(x, y)|^2 dx dy \iint |\tilde{E}_f(x, y)|^2 dx dy} \quad (3.23)$$

where $r(x, y)$ is the complex amplitude replay field and $\tilde{E}_f(x, y)$ is the fibre TEM_{00} mode profile. Equation (3.23) is a measure of how closely the incident field resembles the fibre mode. Each output fibre is typically offset to a coordinate (x_f, y_f) to avoid the zero-order replay. Maximum launch efficiency is achieved when $r(x, y)$ exactly matches $\tilde{E}_f(x, y)$, where:

$$\tilde{E}_f(x, y) = \frac{1}{w_o} \sqrt{\frac{2}{\pi}} \exp \left[-\frac{(x - x_f)^2 + (y - y_f)^2}{w_o^2} \right] \quad (3.24)$$

Figure 3.12 shows a Gaussian replay spot being routed into a single-mode output fibre. The beam is inclined at an angle $\partial\theta$ radians and is offset from the fibre axis by a distance ∂r . The optics are relatively insensitive to axial movement of the waist position and it may be assumed that the Gaussian waist of diameter $2w'_o$ coincides exactly with the fibre end face. The guided-mode has a diameter $2w_o$. Marcuse [34] found an analytical solution of the overlap integral under these conditions:

$$\eta_o = \left(\frac{2w'_o w_o}{w_o'^2 + w_o^2} \right)^2 \exp \left[-\frac{2(\partial r)^2}{(w_o'^2 + w_o^2)} \right] \exp \left[-\frac{2(\pi w'_o w_o \partial\theta)^2}{\lambda^2 (w_o'^2 + w_o^2)} \right] \quad (3.25)$$

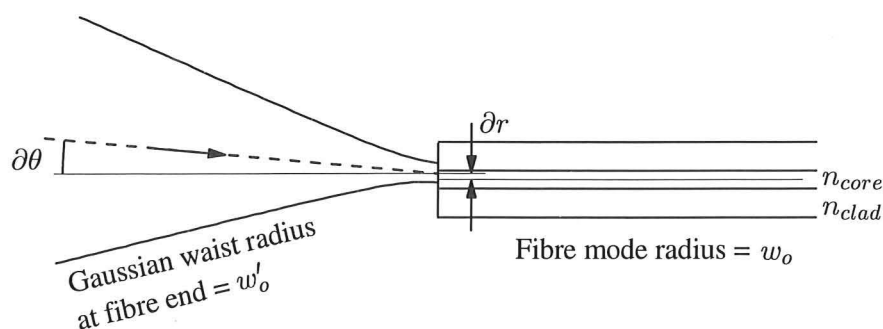


Figure 3.12: Conditions for a replay spot to launch into single-mode fibre.

Equation (3.25) demonstrates the importance of the Fourier flat-phase condition. If the optics of a single-mode fibre switch are not correctly aligned in the form of a $4-f$ relay or equivalent geometry, then the spherical phase distortion of the replay plane introduces an efficiency reducing wavefront tilt across every output spot, worsening with radial distance from the optic axis. To maximise the Gaussian signal launch efficiency and hence maximise the SNR, the output spot-size should be correctly matched to the fibre guided-mode and a (telecentric[†]) lens system should be employed which meets the condition that $\partial\theta = 0$ in all replay field locations.

Figure 3.13 shows two plots of the effect of beam misalignment upon fibre launch efficiencies, for ∂r and $\partial\theta$ respectively. Comparative curves for conventional telecommunication fibres ($\lambda = 1.55\mu\text{m}$) are plotted alongside curves for the fibres within the 1-to-15 fibre array ($\lambda = 780\text{nm}$). Both plots show that the output signal coupling efficiency and therefore the optical SNR and switch insertion loss are very sensitive to misalignments of the optical system. If the system lenses are not diffraction-limited, optical wavefront aberrations in the hologram replay will have a similar effect. The plots also show that the alignment tolerances at the commercial wavelength are slightly less stringent. Therefore it should be easier to optimise a one-to-any switch in a real optical network application than it was to demonstrate the optical-bench system at $\lambda = 780\text{nm}$.

We now need to examine the coupling efficiency of the replay crosstalk noise. Figure 3.14 is a simulation of the experimental replay of figure 3.3(a). The height of the plot represents the output intensity and a greyscale colouring has been used to represent the phase-wavefront. The 32 grey-levels range from 0 to 2π phase, changing from dark to light. This is a typical replay wavefront created by a hologram when the Fourier flat-phase condition is met. It can

[†]Telecentric lenses are designed with the principal ray parallel to the optic axis in object space.

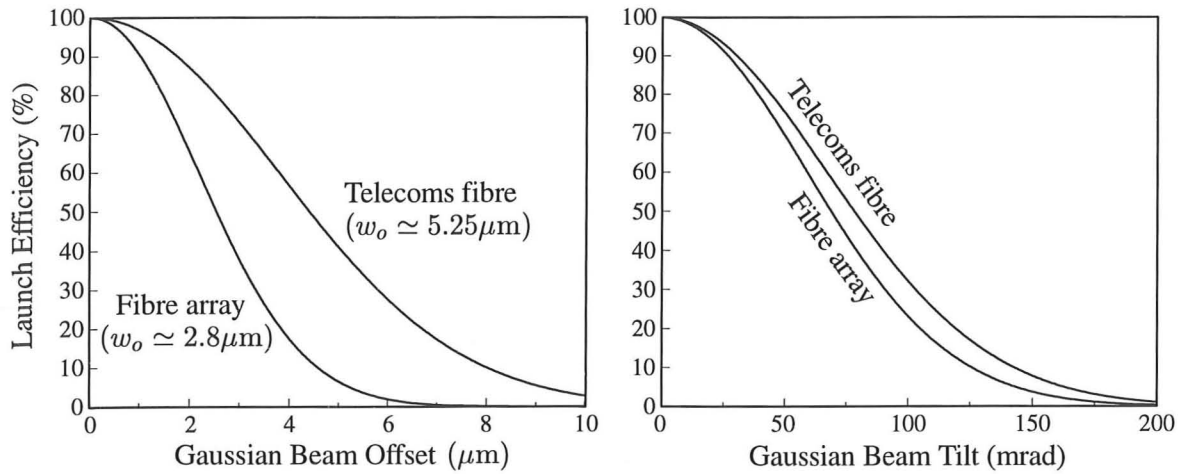


Figure 3.13: Gaussian to single-mode fibre coupling efficiencies.

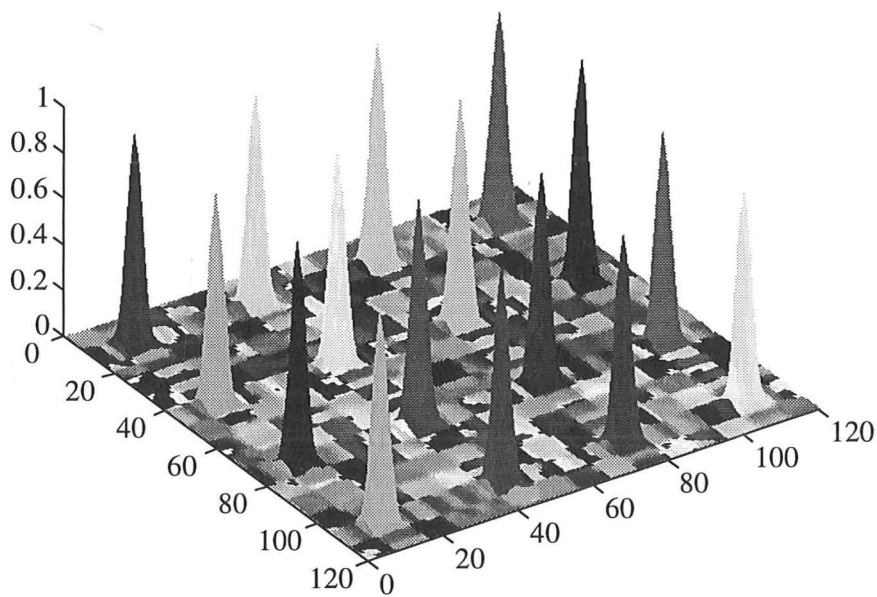


Figure 3.14: Typical hologram replay wavefront.

be seen that the 4x4 Gaussian output spots have flat or nearly flat wavefronts and can be expected to couple into output fibres with high efficiencies. However the phase-profile of the remaining low-intensity quantization noise appears to be completely random and is found to contain very rapid phase transitions. The essentially chaotic nature of this (potential) crosstalk noise ensures that such noise only couples into radiative modes of the fibre outputs as predicted by the low guided-mode overlap efficiency from (3.23). These modes have short transmission lengths and soon leak back out of the fibre cladding. The simulation therefore predicts that when single-mode fibres are used as the output ports, the optical SNR obtained should be considerably greater than when photo-detectors are used.

3.4.2 Experimental crosstalk measurement

To obtain an experimental measurement of the crosstalk noise introduced by the 2DX320 SLM, the basic optics of the 1-to-15 switch experiment were retained, but the input source was replaced by a more powerful 3mW continuous-wave laser diode emitting at $\lambda=670\text{nm}$. This source is closer to the SLM design wavelength of 633nm and thus provides +11.1dB more diffracted power at the output fibres than measured during the 1-to-15 results in figure 3.8. To maintain single-moded operation at this wavelength, the input fibre had to be replaced with one of a smaller core diameter ($w_o \simeq 2.3\mu\text{m}$) and the output fibre array was replaced by a single identical fibre, mounted on a mechanical micro-positioning stage.

A hologram frame was generated to direct power to an off-axis location in the first-order replay field and the output fibre position was optimised to collect maximum light power from this replay. The output fibre was wound once around a 1cm tube and the optical signal was passed to a silicon photo-detector. The effect of the tight bend radius was to remove all non-guided fibre modes and hence to simulate the effect of a longer fibre transmission length. This ensures that only the fundamental TEM_{00} mode reaches the photo-detector.

With the output fibre at a fixed position, a number of CGH frames were then generated and displayed to shift the principal replay spot away from the output fibre core along the 8 compass directions. The experimentally received optical power levels are plotted as '+'s in figure 3.15 as the fibre launch was de-tuned along axial directions, and as 'x's for diagonal directions. These points correspond to the equivalent crosstalk power received by an output in very close proximity to the replay spot, placed at an offset distance given by $N\Delta x_r$ and $\sqrt{2}N\Delta x_r$ respectively, where N is an integer in the range 1-10. Δx_r is the holographic

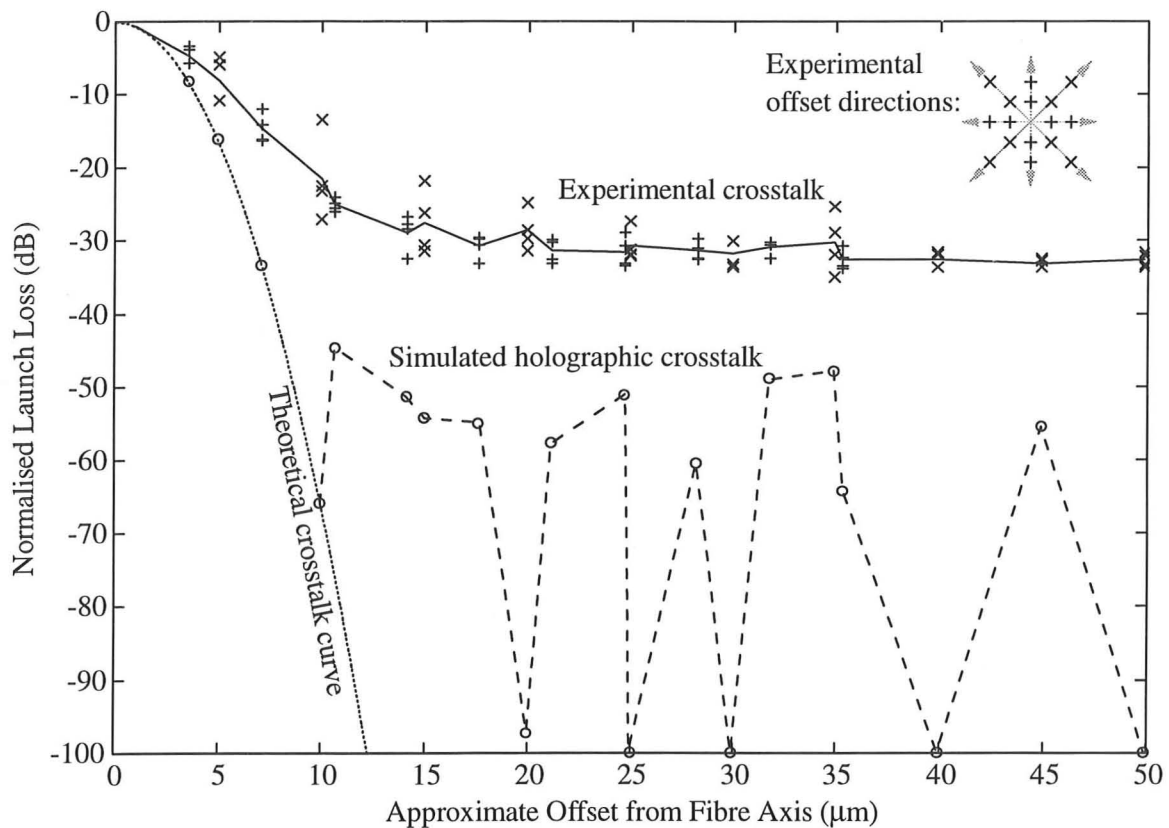


Figure 3.15: Experimental determination of 2DX320 crosstalk performance.

replay resolution which was $\approx 3.5\mu\text{m}$ for the optics used. The mean of each data set of 4 (vertical) points for a particular offset is also superimposed on the figure.

The experimental results have been normalised by the original optimised launch power. This launch was repetitively monitored throughout the experiment and variations in the combined optical power stability of the laser source and the mechanical stability of the entire optical system on an optical bench were found to affect the received power signal by less than 3%.

The experimental readings demonstrate the increased optical insertion loss as the fibre launch is de-tuned, levelling out to a nearly flat crosstalk plateau. This plateau is only about 3dB higher than the photo-detector dark-current and is therefore prone to error. However, the signal was discernible above the electrical noise and even very large replay spot offsets, such that the replay was not even incident upon the fibre cladding, gave the same crosstalk isolation figure. It is therefore unlikely that the crosstalk was due to stray defocused reflec-

tions, but was probably a coherent scatter noise limit of the system.

If the holograms had replayed perfectly without quantization noise, equation (3.25) would have predicted the behaviour of the above experiment from the overlap of Gaussian tails. This is shown as the rapidly descending theoretical curve to the left of figure 3.15. But as shown in figure 3.14, practical holograms generally exhibit background noise. Simulation of the experiment using the same hologram set, yielded the points represented by 'o's. These points initially follow the theoretical curve as expected, but then depart as the CGH quantization effects begin to appear. The discontinuities in the simulation plot are due to fluctuations in the localised quantization noise level, and due to numerical problems with overlap integration across a discrete simulated replay field.

The dotted simulation line represents the best achievable crosstalk isolation for this optical system using the Gerchberg-Saxon hologram iteration algorithm. Even the worst theoretical isolation is better than -40dB and this would improve slightly if the x -axis were extended because the hologram background noise tends to accumulate in axial directions close to the main replay spot. Simulation of a $25\mu\text{m}$ -diameter photodiode positioned in the output field in place of the single-mode fibre, produced a crosstalk plateau of approximately -25dB. This corresponds directly to the power SNRs of the hologram set taken in This simulation figure is worse than even the experimentally determined crosstalk, and therefore as predicted, the use of single-mode fibre outputs is preferable.

The large discrepancy between the experimental and simulated crosstalk curves can only be explained by practical considerations of the SLM. Figure 3.16 is a frame-captured microscope image of a representative portion of the 2DX320 whilst it was displaying a sequence of black-and-white intensity images. The pixel structure and dead-space can be clearly seen, but the high density of glass spacers that were observed through the microscope are too small to be apparent in the frame capture. Many of these spacers do however induce much larger visible liquid crystal defects. These defects are in static positions and are present in both the black and white pixel states. They are regions of FLC material which are not surface stabilised and thus simply fail to respond to the applied pixel voltages. The defect regions are all formed on the same side of their respective spacer. They were probably caused by relative movement of the two SLM glass plates during final SLM assembly such that the resulting movement of the glass spacers destroyed the nearby SiO alignment layer which had been deposited on top of the ITO electrodes.

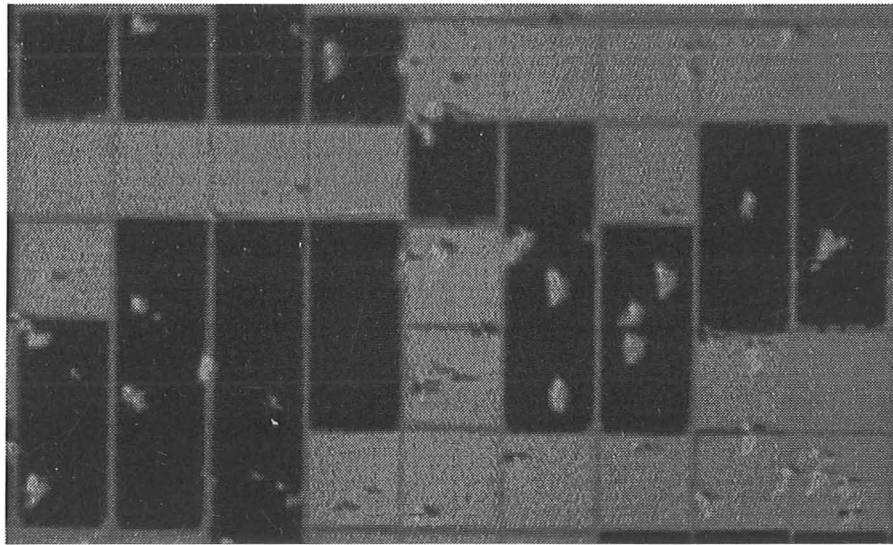


Figure 3.16: Microscope image of a portion of the 2DX320 SLM.

The large number of spacers and defect regions act as scattering centres for the light passing through the SLM. These and other optical non-uniformities tend to produce coherent speckle noise in the replay plane, reducing the output SNR. Silicon backplane SLMs have a much smaller pixel area and therefore require relatively few spacers. In these devices it would be desirable to confine spacer-like structures to dead-space areas only, although the aluminium pixel mirror surfaces will still probably contribute diffraction noise of their own. Initial simulations from visual inspection of the defects in figure 3.16 only account for a small proportion of the discrepancy between simulation and experiment. It is the author's belief that there may be other fundamental limitations to the crosstalk in FLC optical systems, caused by coherent diffractive scattering from molecular domain boundaries and from thickness and refractive index variations throughout the FLC layer. Clearly more work is required in this area before theoretical crosstalk figures can be quoted with confidence.

3.5 Discussion

The experimental results verify that polarisation independent routing of optical signals can be performed using diffractive FLC-SLMs. In particular, the results of the 1-to-15 switching experiment are the first non-mechanical demonstration of optically transparent signal routing between a large number of single-mode fibres, without having to resort to

several cascaded stages of switching. These optical-bench experiments demonstrate the feasibility of free-space optical switching between single-mode fibres, but they have also highlighted some of the experimental design problems that need to be considered, especially the importance of careful design and manufacture of the optical components.

The measured insertion loss of the experimental switch was not sufficiently low enough to be used as the basis of a real world application, but the switching was performed using a large FLC passive-matrix device. This SLM was not well-suited to efficient holography and the catalogue optical lenses that were used to manipulate the Gaussian beam, were not designed for imaging applications at the infrared switch design wavelength.

The simulated annealing technique of generating holograms can be partially optimised to allow the designer some degree of control over how the replay diffraction noise is distributed. If necessary, simulated annealing can also be used to confine the quantization noise in 'safe' regions of the replay, away from the output ports. Its main drawback is the length of time taken to produce each hologram. Fortunately this CGH generation is an off-line process and it should be possible to create holograms with a larger space-bandwidth product that adequately minimise the crosstalk noise (in the absence of other crosstalk effects), probably approaching a figure of -60dB isolation for realistic hologram sizes. Perhaps the hardest question to answer at the current time is: without having to resort to the use of expensive optical amplifiers or regenerators, what is the minimum insertion loss that might be possible using this type of approach to optical switching? The insertion loss has contributions from:

- (1). the optical power that passes undiffracted into the zero-order due to the non-ideal phase efficiency η_s of the FLC-SLM recording medium,
- (2). the redistribution of optical power into the inversion symmetry and into the higher-order diffraction regions because of the theoretical bound η_h on the efficiency of binary, pixellated CGHs with inter-pixel dead-space,
- (3). the power that is scattered into the replay as a background optical noise level due to quantization effects in the hologram function and due to defects within the SLM structure,
- (4). any other losses due to the optical components, including stray reflections and reduced fibre launching efficiencies η_o .

An optimistic view is that a one-to-any switch might be constructed with between perhaps 4dB and 6dB of loss, or less than 3dB if the inversion symmetry could be broken. However,

the diffractive loss penalty and crosstalk figures remain essentially constant for a given FLC switch architecture, regardless of how many outputs are placed in the system. From this point of view, diffractive switches are cheap, scalable and become serious technology contenders when a large number of fibre data-streams need to be interconnected. It is also worth noting that only one amplification stage (at the input) is needed to boost the power level and reduce the insertion loss of a one-to-any switch.

The FLC switch reconfiguration speeds are obviously limited by the SLM frame rate, which in the case of the 2DX320 is only about 10Hz. Realistically, even the fastest FLC switching speeds of about $10\mu\text{s}$ are still insufficient to be suitable for use in fast packet-switching applications. FLC architectures are therefore much better suited to the lower reconfiguration speeds of circuit-switched applications or to network load management, especially where very high data rates and/or wavelength multiplexing makes electronic switching difficult.

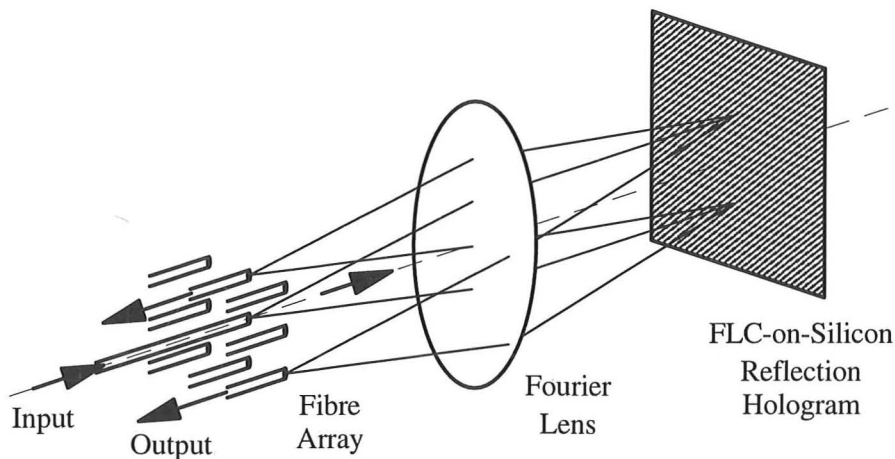


Figure 3.17: One-to-any fibre switch: Compact 2- f architecture.

Through the use of a reflective display such as one of the miniature FLC-over-silicon actively-addressed SLMs, the present bulky demonstration of a one-to-any switch (figure 3.7) could be folded into a much more compact 2- f architecture [63]. In figure 3.17, the on-axis central fibre within the array has been chosen as the input source and the switch is shown making a connection with two of the other outputs within the same fibre array. Light from the central fibre is reflected off and diffracted by the switchable aluminium mirror pads which are integrated onto the silicon backplane beneath the FLC layer. From equations (3.11)

and (3.12), the number of outputs that may be supported by this one-to-any switch is:

$$\text{Maximum number of output fibres} = \left(5.305 \frac{N\lambda}{\Delta s} + 1 \right)^2 \quad (3.26)$$

where Δs is the fibre spacing and N is the number of hologram pixels in one dimension. At telecommunications wavelengths using standard $125\mu\text{m}$ cladding diameter silica fibres, $(0.066N + 1)^2$ array fibres may be supported. An extremely compact 1-to-8 switch could therefore be constructed from 32×32 SLM pixels in a total free-space $2-f$ length of only 5.1mm using $30\mu\text{m}$ pixels. Integration of photodiodes onto the silicon surface might also allow optical control signals to be passed directly to the electronic hardware and the routing hologram patterns might be stored and recalled directly from memory areas within the device circuitry.

A potential problem of figure 3.17 is that of the unwanted zero-order returning along the input fibre and destabilising the signal source. This could be prevented by either placing an opto-isolator on the input fibre, or by laterally moving the entire fibre array slightly, so that the zero-order reflection is incident between fibres. The second method has the advantage that it also introduces non-regular fibre-to-axis distances and neatly avoids the inversion symmetry crosstalk problems. Although shown this way round, the FLC switch is actually fully bidirectional, and any output could return a signal to the single input.

To conclude, careful manufacture and optimisation of the SLM is the most likely factor to improve the performance of fibre switches, although proper optimisation of the lens designs and system alignment would have removed some of the experimental losses in the results presented here. The FLC requirements for fibre switches and other diffractive applications are that the pixel fill-factor and the FLC switching angle must be maximised to help reduce the insertion loss of the system. For use in commercial optical telecommunications, the optics must be designed for use within the Erbium fibre amplifier spectral window, $\lambda \approx 1.55\mu\text{m}$, and the FLC layer will typically need to be thicker than in SLMs which have only been optimised for visible wavelengths. In a real switch, the speed advantage obtained by electronically interfacing with silicon circuitry is important and should not be compromised by a slow FLC response time. Integration with silicon technology also allows the implementation of direct-drive addressing schemes and thus means that high tilt FLC materials without full molecular bistability could be used.

CHAPTER 4

A Holographically Tuneable Wavelength Switch for $\lambda = 1.55\mu\text{m}$

An important emerging application for optically transparent fibre switches is in the implementation of wavelength-division-multiplexed (WDM) network routing elements [75]. The low-loss spectral window of normal telecommunications silica fibre runs from approximately 1250nm to 1600nm. This wavelength range corresponds to a potential optical bandwidth several orders of magnitude larger than current state-of-the-art laser modulation and detection techniques, which can only operate up to 10-20 Gbit/s. The huge potential bandwidth has led to considerable efforts to increase the information bandwidth efficiency of fibres by multiplexing several independently modulated laser sources onto the same optical fibre, each source operating at a slightly different wavelength.

Ferroelectric liquid crystal spatial light modulators operate across all wavelengths for which the liquid crystal is transparent. Typical FLC materials have electronic absorption bands in the ultraviolet and molecular absorption bands in the far infrared [76], but are completely transparent throughout the rest of the optical spectrum. FLC-SLMs obviously exhibit the normal λ -dispersion properties of coarse diffractive elements, but in other respects they have a very broad wavelength response. This makes them very well suited to high data-rate spatial interconnection techniques, but the weak wavelength dependence is insufficient to directly implement wavelength routing for dense WDM applications.

To avoid having to demultiplex and remultiplex the signals at each network node, WDM networks generally establish data connections via some kind of dynamic allocation of the available wavelengths [77], tuning either the individual lasers and/or the receivers to the assigned wavelength on demand. These systems not only allow more efficient utilisation of

the optical bandwidth, but they also introduce extra flexibility into the fibre network by allowing wavelength selective switching elements to perform optically transparent routing. WDM networks therefore rely on the functionality provided by wavelength tuneable sources, receivers and filters.

This chapter presents a completely new approach to WDM network routing by combining a CGH-SLM with a high resolution diffraction grating to achieve a tuneable filter device with a narrow-band wavelength response. These are the first recorded results utilising an FLC-SLM for long wavelength free-space switching and they demonstrate the suitability of programmable CGHs for telecommunication fibre networks. The diffractive nature of the device provides the potential for excellent crosstalk isolation between WDM channels.

4.1 Diffractive WDM Components

The use of fixed gratings for reversible WDM (de)multiplexing is well known [78]. These are passive systems which allow multiple WDM channels to be either completely combined or completely separated, but they do not provide selective filtering or dynamic switching of the various fibre network bit-streams. In these (de)multiplexers, angular wavelength combination of the channels into the network, or dispersion from the network, is governed by the grating equation:

$$\sin \phi_r + \sin \phi_i = \pm m \frac{\lambda}{d_F} \quad (4.1)$$

where ϕ_i and ϕ_r are the grating angles of incidence and reflection (or transmission) respectively, of the WDM channel of unmodulated wavelength λ . These angles are defined relative to the grating surface normal, and have the same sign if they occur on the same side of the normal. d_F is the fixed grating pitch, defined for a binary grating to be twice the feature size or for a blazed grating to be the distance between ridges, and m is the grating diffraction order being used.

Of the various configurations possible, the most commonly known is the Littrow mount shown in figure 4.1. In this configuration, the wavelength dispersive element is a planar, blazed reflection grating, tilted to obtain high diffraction efficiency in the first-order ($m=1$) and to reduce the angles through the lens such that $\phi_i \simeq \phi_r$. Selection of the correct spatial regions within the output plane (typically by means of single-mode fibres) allows

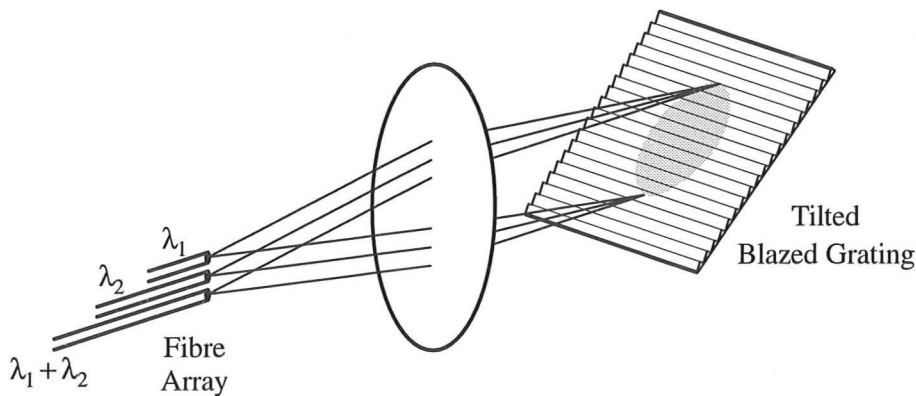


Figure 4.1: The Littrow mount passive wavelength (de)multiplexer.

every WDM channel to be demultiplexed and isolated. As with most single-mode free-space architectures, the Littrow configuration has telecentric imaging and meets the requirements for reciprocity. Lossless multiplexing of many WDM channels into one single-mode fibre is thus also possible.

The WDM channel spacing $\Delta\lambda$ supported by this type of multiplexer, is obtained by differentiation of equation (4.1). Assuming that the grating is inclined at a fixed angle of $\phi = \phi_i$ to the vertical:

$$\begin{aligned} \Delta\lambda &\simeq d_F \cos \phi \Delta\phi_r = \frac{\lambda_0 \Delta\phi_r}{2 \tan \phi} \\ &\simeq \left| \frac{\lambda_0 \Delta y}{2f \tan \phi} \right| \end{aligned} \quad (4.2)$$

where λ_0 is the wavelength for which $\phi_i = \phi_r$, Δy is the distance between fibres in the output plane, and f is the lens focal length.

4.1.1 Ferroelectric liquid crystals as dynamic gratings

Various methods of achieving wavelength tuning have been suggested. These include techniques based on liquid crystal birefringent slabs [79], Fabry-Perot cavity filters [80], acousto-optic surface wave effects [81] and semiconductor resonant amplification [82]. A method of simultaneous space and wavelength switching using a mechanically rotatable grating has also been demonstrated [13]. But these methods are generally analogue in operation, have non-linear responses, and hence require complex calibration or control algorithms.

If the grating pitch in figure 4.1 could be dynamically varied, then the passive multiplexer would be converted into a tuneable switch capable of directing different wavelengths towards a fixed output fibre or detector. FLC-CGHs are capable of displaying arbitrary binary phase holographic patterns and are therefore suitable devices to be configured as dynamic WDM gratings. Unfortunately, currently available FLC-SLM devices do not address enough pixels/mm to achieve sufficiently high wavelength dispersion to make them directly useful in a Littrow configuration. In addition, the variation in holographic pitch that must be displayed on the SLM to tune the component, adversely affects the wavelength resolution $\Delta\lambda$ across the tuning range, resulting in a non-linear WDM channel spacing.

Both these problems are solved by the use of a fixed grating of smaller pitch in combination with the FLC-SLM. This is a new configuration [44], using the SLM to achieve very fine angular tuning of the angle of incidence from a wavelength-multiplexed source onto the fixed grating. The grating then provides the large angular dispersion of the spectral channels that is required in dense WDM applications. The difference in pitch between the two diffractive elements can be arranged to produce a wavelength filter with a very high channel density and with nearly constant channel spacings. Tuning of the filter relies upon an exact CGH pattern being displayed on the SLM and the switch operation is therefore extremely repeatable. The tuning may also be considered to be digital in nature because it is determined by a binary image frame, rather than by an analogue control signal.

4.2 The Wavelength Switch Architecture

The architecture that was chosen for investigation of a holographic wavelength switch was the compact 2- f double-pass system shown schematically in figure 4.2. Conceptually this is just a folded Gaussian relay with the central SLM replaced by a combination of an SLM and a fixed grating. The architecture is designed to filter one or more wavelengths on demand from a multi-wavelength coherent source, e.g., in conjunction with a fibre splitter, it could be used as the local traffic dropout in a WDM routed fibre network. The switch is therefore an N -to-1 wavelength router, configured to reduce the physical extent of the switch and minimise the number of optical components that are required.

The multiplexed WDM channels enter the system from a cleaved single-mode input fibre that has been aligned along the system optic axis. The resultant multi-chromatic beam

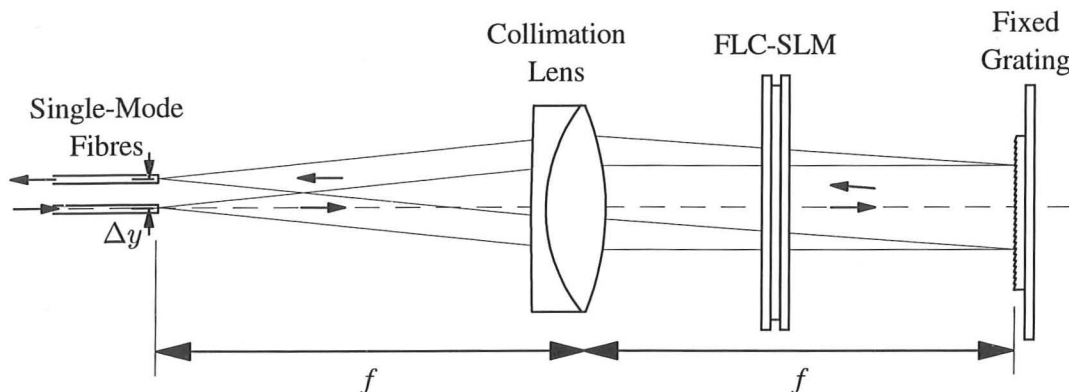


Figure 4.2: Tuneable wavelength switching experiment.

is collimated by the lens and is diffracted through the FLC-SLM pattern onto the fixed grating. Each spectral component of the source is incident upon the grating at a slightly different angular direction, according to which CGH frame is displayed from the set of pre-calculated holographic patterns. The optical channels are reflected from and dispersed by the fixed diffractive element, back through the same CGH pattern, then refocused through the lens into the input/output plane. As with the fixed demultiplexer, the various WDM channels are now spatially dispersed, and a single data channel may be filtered from the others by means of an output fibre. Dynamic selection of the filtered channel occurs as the SLM pattern is altered, and the reconfiguration speed of the switch is thus determined by the SLM frame rate. The inherent redundancy within CGH frames makes the architecture extremely robust against corrupt frame pixels.

Provided the fixed grating is placed exactly one focal distance behind the lens, the positioning of the SLM is unimportant because the return pass of light through the FLC-CGH ensures that the output imaging is always telecentric. To explain this operation, it is easiest to resort to conventional ray-tracing techniques. Consider the path of the principal ray as shown in figure 4.3. Because the input source is axially aligned, the principal ray passes through the centroid of the collimation lens, and it is then diffracted by three surfaces. From equation (4.1), the surface equations are:

$$\sin \phi_1 = \pm \frac{n}{N} \times \frac{\lambda}{d_{SLM}} \quad , \quad \sin \phi_2 = \frac{\lambda}{d_F} + \sin \phi_1 \quad , \quad \sin \phi_3 = \pm \frac{n}{N} \times \frac{\lambda}{d_{SLM}} + \sin \phi_2 \quad (4.3)$$

where ϕ_1 , ϕ_2 and ϕ_3 are defined as the ray angles to the grating normals as shown in

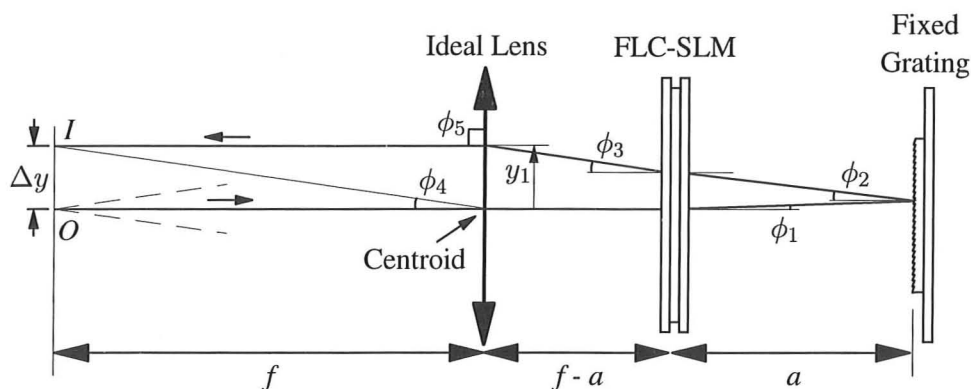


Figure 4.3: Ray-trace of the principal ray through the WDM switch of figure 4.2.

figure 4.3, d_{SLM} is the SLM pixel pitch, N is the number of SLM pixels in a direction perpendicular to the fixed grating grooves, and n is an integer in the range $0 \rightarrow \frac{N}{2}$ which sets the equivalent grating pitch of the current SLM frame. Hence n determines the tuning of the switch, where the \pm signs are due to the first-order and symmetry deflections from the binary CGH-SLM. Figure 4.4 shows a typical switch frame and the angular far-field replay it produces. The irregularities in the CGH periodicity result in an effective grating pitch of $\frac{N}{n} \times d_{SLM}$, which is a non-integer multiple of the SLM pixel pitch. This extra resolution is gained at the expense of introducing some noise peaks in the replay.

In figure 4.3, the principal ray arrives at the lens on its return path at a height y_1 above the axis. Provided all angles are small, we may make the approximation that $\cos \phi \simeq 1$ and hence $\tan \phi \simeq \sin \phi$. Substituting the expressions of (4.3) gives:

$$\begin{aligned} y_1 &= a(\tan \phi_1 + \tan \phi_2) + (f - a) \tan \phi_3 \\ &= f \sin \phi_3 \end{aligned} \quad (4.4)$$

From the properties of ideal thin lenses, the angle ϕ_4 that the image point I subtends to the centroid of the lens, must be equal to ϕ_3 . Hence the separation distance Δy between the input and output fibres must equal y_1 , making ϕ_5 a right-angle. Thus assuming that the performance of the actual lens used in the filter design is close to a diffraction-limit, the output beam will always be focused with a flat wavefront and a high efficiency single-mode fibre launch can be expected. The input and output fibres are also conveniently aligned parallel to one another.

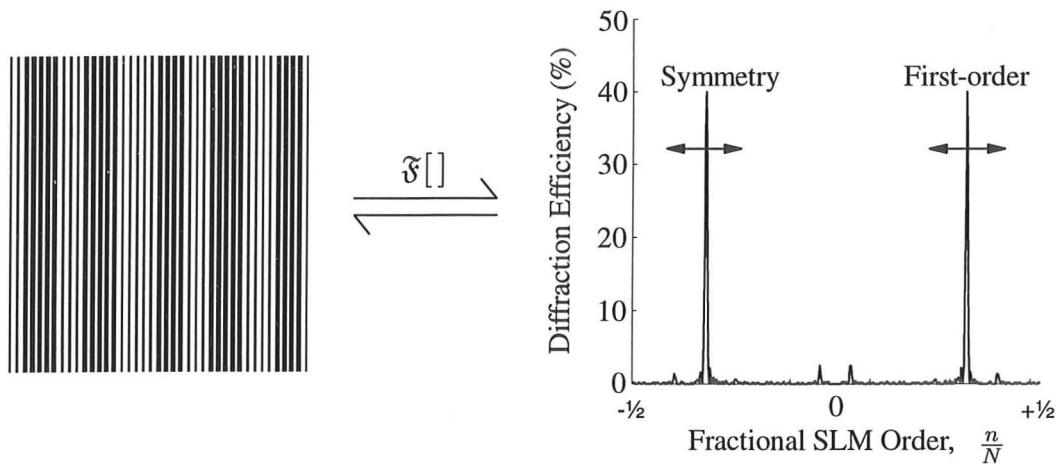


Figure 4.4: Typical WDM switch hologram and replay.

The first- and symmetric-diffraction orders of the CGH frame each direct a different wavelength into the output fibre. These two wavelengths may be dynamically tuned simultaneously by changing the SLM holographic equivalent grating pitch. Unfortunately a third, untuneable wavelength is also filtered, which corresponds to the wavelength which would be received if the SLM were removed from the system. These three wavelength solutions may be predicted by combining the grating equations of (4.3):

$$\lambda_r = \frac{\Delta y}{f\left(\frac{1}{d_F} \pm \frac{n}{N} \times \frac{1}{d_{SLM}} \pm \frac{n}{N} \times \frac{1}{d_{SLM}}\right)} \quad (4.5)$$

where λ_r are the unmodulated WDM channel wavelengths that are received in the output fibre. The untuneable wavelength arises because the two \pm signs are independent. However, by designing the switch and arranging the fibre separation in such a way that the fixed wavelength and, for example, the longer wavelength tuneable solution, exist in unused spectral regions of the WDM network, the desired single channel filtering may be achieved:

$$\lambda_r = \frac{\Delta y}{f\left(\frac{1}{d_F} + \frac{n}{N} \times \frac{2}{d_{SLM}}\right)} \quad (4.6)$$

The spectral range (and therefore the modulated WDM channel bandwidth) filtered into the output fibre is determined by the overlap integral of equation (3.25). With telecentric output imaging, the launch condition $\partial\theta = 0$ holds for all dispersed wavelengths so that

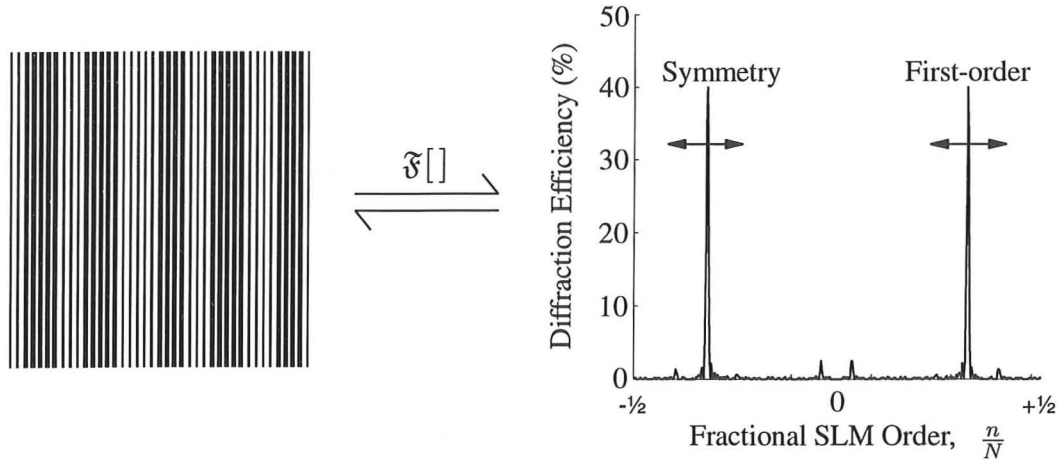


Figure 4.4: Typical WDM switch hologram and replay.

The first- and symmetric-diffraction orders of the CGH frame each direct a different wavelength into the output fibre. These two wavelengths may be dynamically tuned simultaneously by changing the SLM holographic equivalent grating pitch. Unfortunately a third, untuneable wavelength is also filtered, which corresponds to the wavelength which would be received if the SLM were removed from the system. These three wavelength solutions may be predicted by combining the grating equations of (4.3):

$$\lambda_r = \frac{\Delta y}{f\left(\frac{1}{d_F} \pm \frac{n}{N} \times \frac{1}{d_{SLM}} \pm \frac{n}{N} \times \frac{1}{d_{SLM}}\right)} \quad (4.5)$$

where λ_r are the unmodulated WDM channel wavelengths that are received in the output fibre. The untuneable wavelength arises because the two \pm signs are independent. However, by designing the switch and arranging the fibre separation in such a way that the fixed wavelength and, for example, the longer wavelength tuneable solution, exist in unused spectral regions of the WDM network, the desired single channel filtering may be achieved:

$$\lambda_r = \frac{\Delta y}{f\left(\frac{1}{d_F} + \frac{n}{N} \times \frac{2}{d_{SLM}}\right)} \quad (4.6)$$

The spectral range (and therefore the modulated WDM channel bandwidth) filtered into the output fibre is determined by the overlap integral of equation (3.25). With telecentric output imaging, the launch condition $\partial\theta = 0$ holds for all dispersed wavelengths so that

only the exponential term containing ∂r can affect the channel response, where ∂r is the distance of each focused wavelength from the output fibre core. Provided the dispersion angles are small and $d_F \ll d_{SLM}$, the spatial dispersion of wavelengths in the output plane is almost constant. Hence the launch efficiency for wavelength λ when the switch has been tuned to receive wavelength λ_r , will be:

$$\eta_\lambda \simeq \exp \left[- \left(\frac{f|\lambda - \lambda_r|}{d_F w_o} \right)^2 \right] \quad (4.7)$$

The holographically tuneable wavelength switch of figure 4.2 therefore has a Gaussian channel response with a full-width at half-maximum (FWHM) spectral range:

$$\lambda_{FWHM} \simeq \frac{2w_o d_F \sqrt{\ln 2}}{f} \quad (4.8)$$

where w_o is the output fibre's single-mode guided field radius.

4.2.1 Experimental wavelength switching

In the absence of a multi-channel WDM source, a Fabry-Perot semiconductor laser diode was coupled into a single-mode telecommunications fibre ($w_o \simeq 5.25\mu\text{m}$) and the various modes emitted by the laser were used as the switch input. The laser was manufactured to be the optical pump for an Erbium amplifier, and it should therefore produce several milli-Watts of output power across a fairly wide spectral range. However the device had been rejected for its intended purpose because the laser cavity was found to be defective. An L-I characterisation of the device showed that it was only just lasing, with an indistinct threshold at about 55mA drive. The laser diode was found to emit in the infrared spectrum at about $\lambda = 1.45\mu\text{m}$. It was coupled with a 633nm HeNe laser through a -3dB fibre splitter, and the two fibre splitter output arms formed the input to the filter, and a separate monitor fibre for recording the laser diode output power and spectrum. The defective nature of the diode laser caused it to produce a rather irregular output spectrum, (see figure 4.8), but it adequately served the purposes of this proof-of-principle switch design. The visible HeNe beam was only used for initial optical alignment of the system, and was switched off during measurements.

The switch input and output fibres were positioned exactly one focal distance in front of a

38mm diameter, 76.2mm focal length cemented achromatic lens, and were set $\Delta y = 5.6\text{mm}$ apart. The switch was thus operated with the non-tuneable wavelength solution lying outside the laser diode spectral range at about $\lambda_F = 1.47\mu\text{m}$. The fixed diffraction grating was an in-house reflective binary phase grating and was made with 100 lines/mm pitch ($d_F = 20\mu\text{m}$).

The FLC-SLM was wavelength optimised for use within the fibre telecommunication band. Figure 4.5(a) is the diffractive phase efficiency response versus wavelength of the 2DX320 SLM used in the last chapter, taken from equation (3.10). This device has a spectral width of 400nm over which the phase efficiency is within -1dB of its peak value. But the 2DX128IR SLM response shown in figure 4.5(b) is more appropriate for operation at longer infrared wavelengths. The 2DX128IR[†] device has been filled with BDH744[‡] liquid crystal to a thicker depth of about $4\mu\text{m}$. Consequently, its frame rate is slightly slower than might be achieved with a thinner cell of the same specification, but its peak spectral response occurs at about $\lambda = 1.44\mu\text{m}$, and its -1dB response spans $\lambda = 1.1\mu\text{m}$ to $2.05\mu\text{m}$.

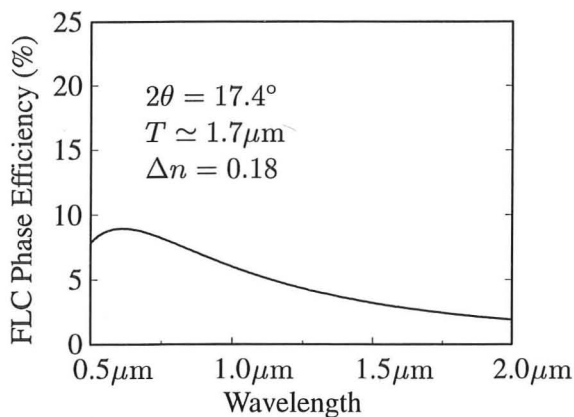


Figure 4.5(a): Wavelength response of the 2DX320, optimised for $\lambda \simeq 633\text{nm}$.

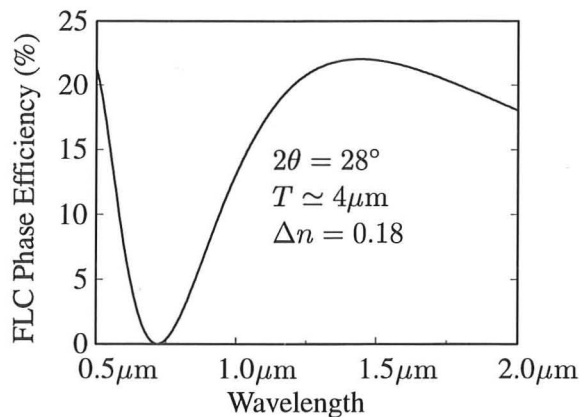


Figure 4.5(b): Wavelength response of the 2DX128IR, optimised for $\lambda \simeq 1.5\mu\text{m}$.

The 2DX128IR is driven from a $\pm 15\text{V}$ supply and is of a transmissive glass cell construction with 128×128 pixels arranged on a $d_{SLM} = 165\mu\text{m}$ pitch. The dead-space between pixels is $5\mu\text{m}$. The FLC material inside the device has a birefringence $\Delta n = 0.18$, effective switching angle $2\theta = 28^\circ$, and was manufactured with $4\mu\text{m}$ glass spacers. The SLM provided the experimental switch with 64 discrete wavelength tuning steps, leading to the near-linear wavelength response shown in figure 4.6 (from equation (4.6)). The Gaussian filter channels

[†]The 2DX128IR device was specifically developed by STC Technology for applications at $\lambda = 1.5\mu\text{m}$. Increasing the FLC thickness whilst maintaining the stringent conditions for passive multiplexing [30] required considerable experimentation, (unpublished work by A.B. Davey, A. Sparks and W.A. Crossland).

[‡]Material developed during the Joers-Alvey collaborative project on large area FLC displays.

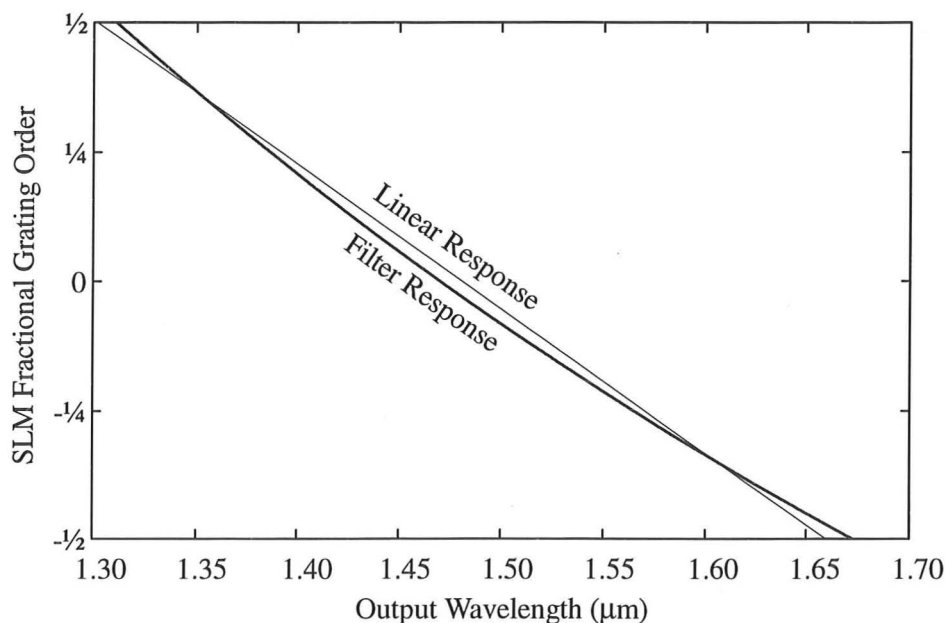


Figure 4.6: FLC-SLM tuning response for the experimental WDM switch.

had a FWHM response of $\lambda_{FWHM} \simeq 2.3\text{nm}$ and a mean channel separation of $\Delta\lambda \simeq 2.5\text{nm}$. Although finer resolution could be achieved by increasing the focal length f , or by reducing the fixed grating pitch d_F , both these parameters were limited by the SLM clear aperture.

Figure 4.7 is a photograph of the compact experimental switch as it was laid out on an optical bench. The components that can be seen in this photograph are:

- | | |
|-----------------------------------|---|
| (1). -3dB fibre coupler, | (6). Positioning mount for the fixed grating, |
| (2). Laser diode pig-tail fibre, | (7). 2DX128IR SLM, |
| (3). HeNe laser and fibre launch, | (8). Collimation / focusing lens, |
| (4). Spare coupler output arm, | (9). Input fibre mount, |
| (5). SLM power supply, | (10). Output fibre. |

The CW laser diode input source had the spectral characteristic of figure 4.8. This plot was generated by connecting the spare single-mode fibre splitter arm to a Hewlett Packard MS9030A optical spectrum analyser. The fibre coupler operated as a 50-50% splitter at the laser diode wavelength and therefore figure 4.8 is also an accurate indication of the power levels that entered the switch. Superimposed as dashed curves onto this figure are four arbitrarily normalised Gaussian filter responses (A through D), representing the approximate positions of consecutive tuning envelopes. The SLM was programmed to each

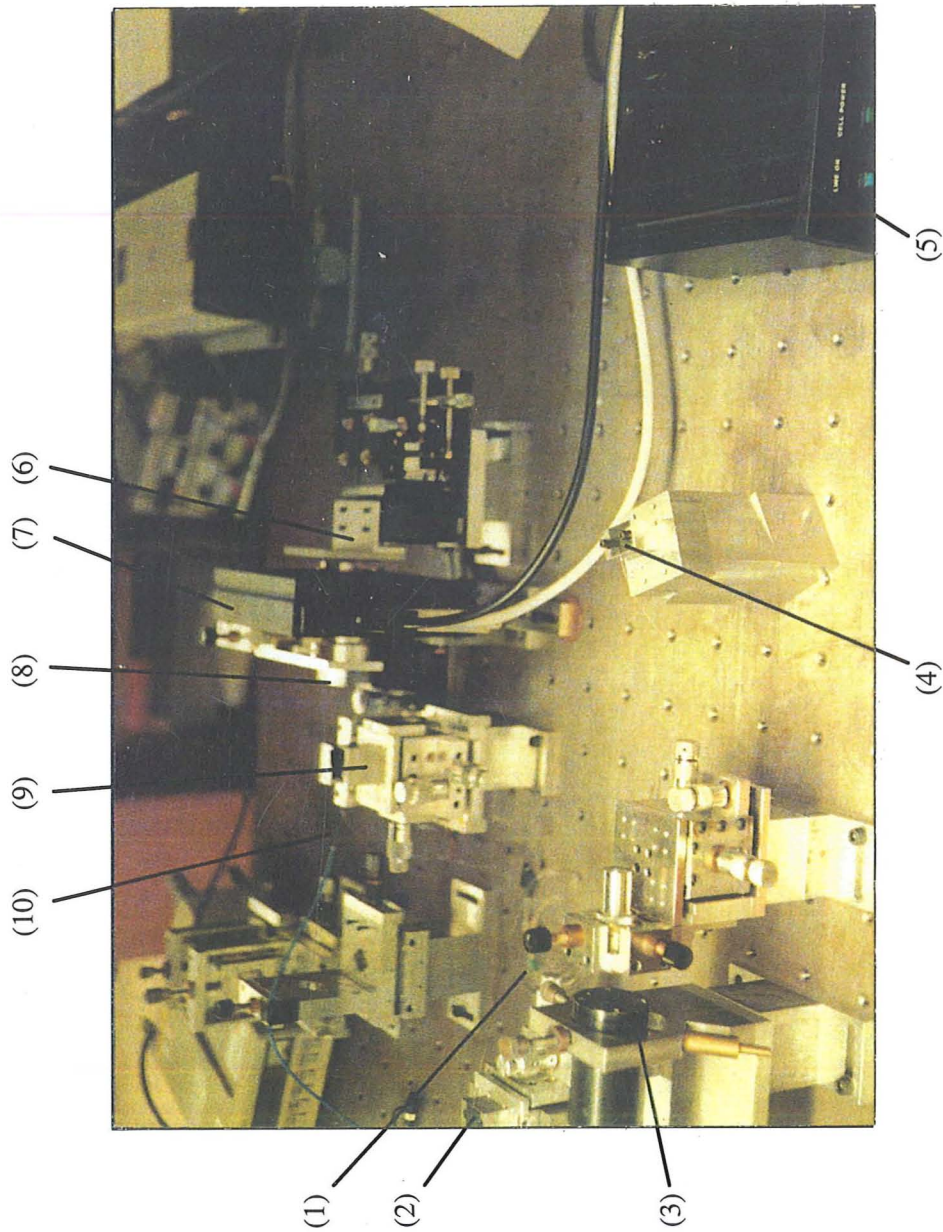


Figure 4.7: Photograph of the WDM switch experimental setup.

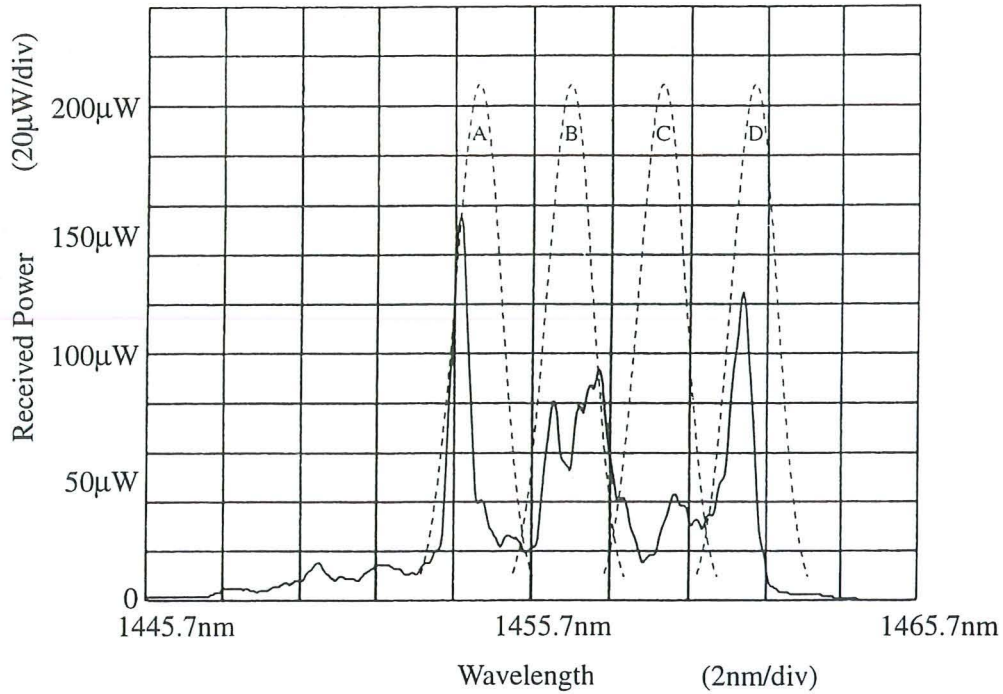


Figure 4.8: Spectral characteristic of the input diode laser source.

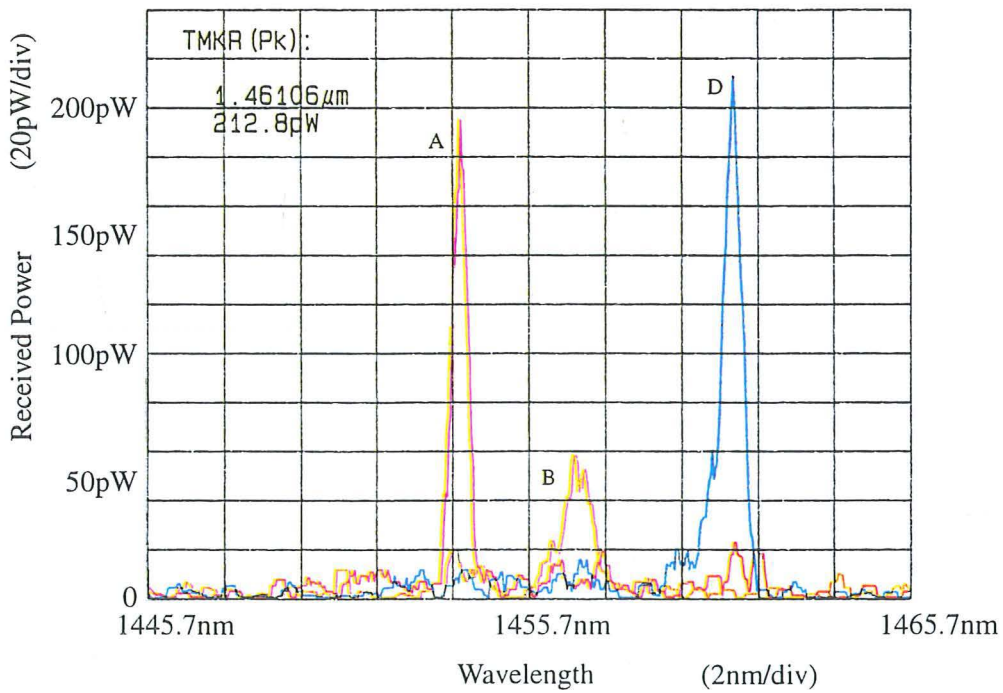


Figure 4.9: Experimentally filtered output spectra.

of these responses in turn, in an attempt to isolate each of the three major modes of the diode spectrum, figure 4.9. In this second plot, the three independently colour-coded spectra correspond to different SLM frames and hence to different filter responses. It can be seen that although the two outer laser modes lie fairly close to the centres of their respective envelopes, the central mode does not coincide so well and has been suppressed by the channel response. The three modes have however been successfully and independently isolated. Envelope C falls in a relatively inactive region of the diode spectrum and has therefore been omitted from figure 4.9. Although the input spectrum was only about 8nm wide, the space-bandwidth product of the SLM means that a total spectral tuning range of almost 160nm would have been possible with this particular experimental configuration.

4.2.2 Insertion loss performance

The results of this digitally tuneable wavelength filtering switch have succeeded by demonstrating for the first time that FLC-SLM switches are inherently capable of operating at standard telecommunication wavelengths. Although it has been impossible to investigate the full switch capability without access to a proper wavelength-multiplexed source, the experiment has also shown that the introduction of a passive grating into the optical system allows the wavelength selectivity of diffractive FLC-SLMs to be enhanced and exploited for configuration or routing of WDM networks.

The insertion loss of this proof-of-principle design is very high ($\simeq 60\text{dB}$), and one of the largest contributions to the loss may be accounted for by defects in the optical system. The overriding limitation occurs because of the choice of a PAC076 Newport Corp. catalogue achromatic as the transfer lens in the experiment. This lens was known to be diffraction-limited at $\lambda = 546\text{nm}$ for field angles less than 2° , but its experimental performance was found to be rather compromised when operated at a wavelength $\lambda = 1.45\mu\text{m}$, and at field angles of $\simeq 4^\circ$. The infrared nature of the source meant that the extent of the lens imaging problem was only discovered at a later date when the switch optics were modelled at $\lambda = 1.45\mu\text{m}$ for wavefront distortion. Simulations predict that optimisation of the optical configuration would result in a decrease of the fibre relaunch and imaging distortion losses by more than 20dB, leaving a residual optical loss of 1 or 2dB due to fibre coupling and glass reflections.[†]

[†]Substantial optimisation of wavelength filtering performance, including a dramatic reduction of the optical insertion loss to about 26dB, has recently been performed by M.C. Parker [83].

4.3 Optical Simulation of the Wavelength Switch

A model of the experimental system was constructed and examined using the CODE V software package [84]. Figure 4.10(a) is a diffraction-based simulation of the exit pupil wavefront. This plot shows a considerable aberration of almost 4λ across a rather curiously shaped pupil. The form of the pupil is a combination of the $(21.12\text{mm})^2$ square SLM aperture, and aperture clipping at the final circular 35mm diameter polariser during the return off-axis pass of the beam through the filter. The effective aperture shape does not limit the design in reality though, because the exit phase pupil function also has a Gaussian intensity profile such that over 99.3% of the optical power passes through the pupil. The optical performance is therefore determined exclusively by the phase contours.

Diffraction-based optical modelling relies on the assumptions [31] that the entrance pupil has a finite aperture which is uniformly illuminated, and that the system aberrations are sufficiently modest for ray-tracing to adequately describe the light beam between the entrance and exit pupils. Diffraction effects are only included between the exit pupil and the image plane. The CODE V model also constrains gratings and holograms to be simulated as elements without thickness, generating only a single diffraction order. The exit pupil wavefront is therefore only an approximate form of the coherent transfer function (CTF) of the filter optics, but it is reasonably accurate for point-like TEM_{00} sources.

The Fourier transform of the CTF is the point-spread function (PSF), and the output spot profile is predicted by convolving this function with the Gaussian input fibre mode:

$$\text{Complex amplitude output field} = G(w_o) * \mathfrak{F}[\text{CTF}] \quad (4.9)$$

The simulated output spot intensity image is shown in figure 4.10(b). Although severely aberrated, most of the power lies along a line in the x -direction. This explains why it was possible to experimentally tune the switch to different wavelengths without an overwhelming amount of crosstalk between consecutive channels. The presence of some noise along the y -axis direction of wavelength dispersion probably accounts for the relatively poor experimental signal-to-noise ratios (figure 4.9), although this may also have been due to the noise limit of the optical spectrum analyser.

In a properly designed system, the crosstalk isolation between WDM channels should reach or exceed the -30dB diffraction-noise limit measured in chapter 3. To achieve this perfor-

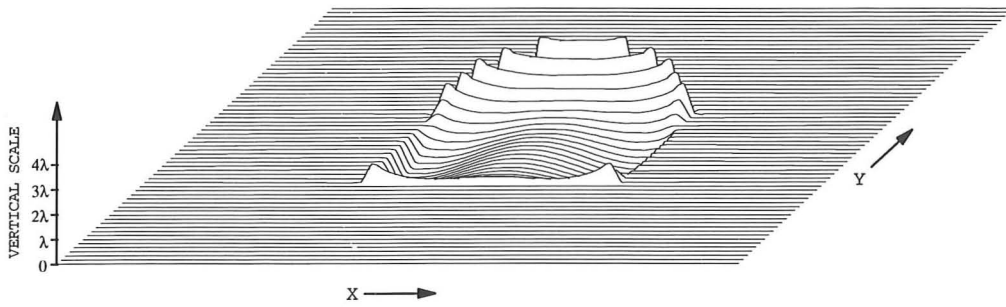


Figure 4.10(a): CODE V simulation of the exit pupil wavefront.

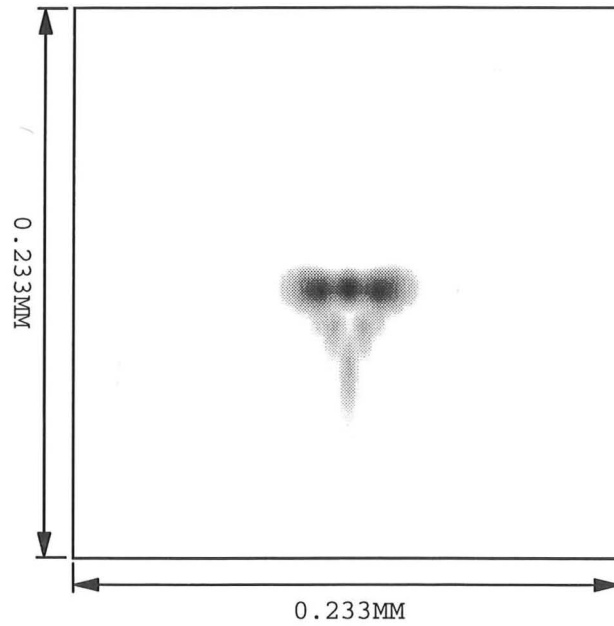


Figure 4.10(b): CODE V simulation of the output spot intensity profile.

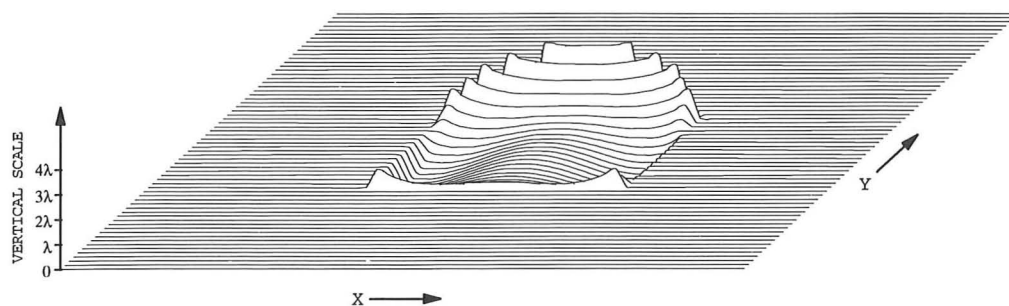


Figure 4.10(a): CODE V simulation of the exit pupil wavefront.

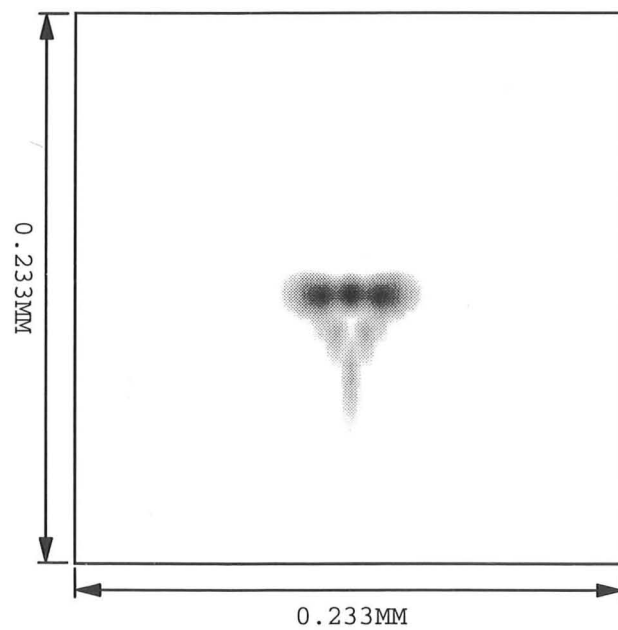


Figure 4.10(b): CODE V simulation of the output spot intensity profile.

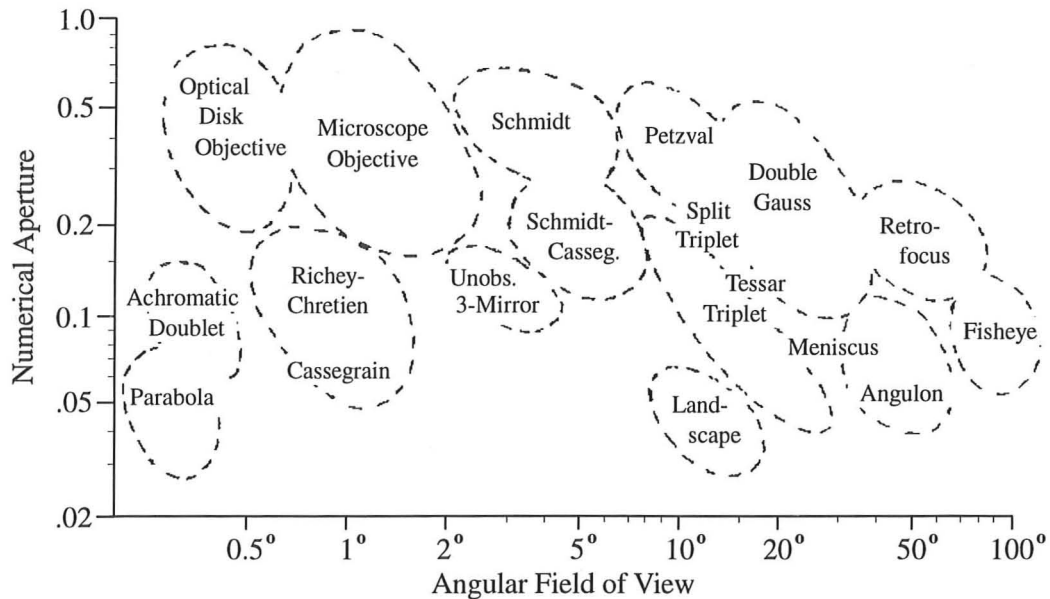


Figure 4.11: Operating parameters for commonly used lens designs.

mance, a number of alternative lensing systems were considered and modelled. In simulation, aspheric and multi-element lenses perform far better than the PAC076 achromatic doublet, but they still fall short of the diffraction-limit. The best output wavefront profile that could be generated exhibited 0.8λ of phase distortion, corresponding to a residual optical loss of about 4dB. Aberration-free imaging is elusive because the return optical pass of a single lens system at a high angular deviation makes minimisation of aberrations very difficult. This is demonstrated in figure 4.11 which is a diagram of standard lens configurations [85]. Unfortunately, it shows no recommended design for single-mode fibres (numerical aperture $\simeq 0.11$) at 4° field of view.

A recent $4-f$ unfolded filter configuration is discussed in [86]. Although this configuration avoids many of the optical imaging problems by allowing a second output lens to be tilted, it is ultimately less compact and more difficult to align. Perhaps the most promising double-pass $2-f$ lens configuration for the switch is an $f-\theta$ scanner lens [87, 88]. These lenses are specifically designed to scan a Gaussian laser beam through large angular deviations, and they are commonly found in supermarket bar-code scanners and in laser printers. Although scanner lenses are typically optimised for monochromatic sources, the wavelength dispersion of most glasses throughout the infrared spectrum is much lower than in the visible range. It should therefore be possible to optimise a design across a reasonable WDM spectral range.

Alternatively, a large subset of applications might involve the immediate photo-detection of the filtered signal. The output fibre could then be replaced with either a small diameter photodiode, or with a short length of multi-mode fibre. This would relax the optical imaging requirements at the expense of a broader full-width half-maximum channel response. Use of a multi-mode output fibre would also provide the filter with a steeper, non-Gaussian wavelength response.

4.4 Use of a 1-Dimensional SLM

The minimum insertion loss of the experimental switch is theoretically determined by the diffraction efficiencies of the SLM and of the reflective grating. Due to the generation of symmetric- and higher-orders, the diffraction efficiency (η_h) of binary phase SLM holograms cannot generally exceed the bound derived in the last chapter. However, the switch tuning holograms typically only need to be 1-dimensional grating-like structures (figure 4.4). In this particular switch configuration, there is little advantage in having the second hologram dimension unless the switch is to route wavelength channels to more than output fibre. In fact there are several positive benefits to be gained by replacing the 2DX128IR with an SLM that only consists of a 1-dimensional array of long, thin pixel stripes. These advantages may be summarised as follows:

- (1). the SLM dead-space between pixels is removed from one of the two dimensions and the theoretical bound on hologram efficiency from equation (3.22) is increased to:

$$\eta_{h1d} = \mathcal{T}^2 \text{sinc}^2 \left[\sigma\pi\mathcal{T} \right] \quad (4.10)$$

where \mathcal{T} is the active width to pixel pitch ratio as before, and σ is the fractional SLM grating order $\frac{n}{N}$. Notice that the original \mathcal{T}^4 in equation (3.22) has now been reduced to a squared power.

- (2). in a 1-dimensional glass cell device, only one face of the SLM has to be patterned with pixels, making the construction and alignment of the device much simpler.
- (3). each pixel stripe in a 1-dimensional SLM may be continuously powered, and the device may therefore be filled with a high-tilt FLC material. Such materials often lack any significant bistability and are therefore unsuitable for 2-dimensional passive glass cells. The use of a high-tilt FLC material means that the imperfect diffractive phase effi-

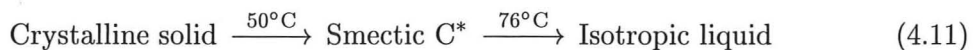
ciency performance (η_s) of the switch SLM can be greatly improved, further reducing the overall switch insertion loss by up to 13dB.

The ideal solution for driving a non-bistable FLC material would be to continuously power the entire pixel array through an FLC-over-silicon backplane SRAM SLM, but until these devices become more readily available, the relative merits of silicon devices versus glass cells are less clear-cut for 1-dimensional SLMs than they are for full 2-dimensional pixel arrays. The pixel layout for a 1-dimensional transmissive glass device is much faster and simpler to design, considerably cheaper to manufacture, and the SLM is not limited by the fairly low voltages of standard silicon VLSI processes. In fact most FLC materials, and high-tilt materials in particular, generally work much better with drive voltages of the order of $\pm 20\text{V}$, which cannot easily be supplied by a silicon backplane.

4.4.1 Experimental performance of a 1-dimensional SLM

To improve the performance of the tuneable wavelength filtering switch and investigate the properties of a better optimised FLC material, a 1-dimensional SLM was designed and assembled. This device is based on the Thorn EMI CRL 2DX320, but with one glass face replaced by a single large electrode. The resulting 1-dimensional SLM array has 320 pixel stripes arranged on a $80\mu\text{m}$ pitch with $5\mu\text{m}$ dead-space gaps ($\mathcal{T} = 0.94$). The SLM square usable aperture is $(25.6\text{mm})^2$ and rubbed polymer FLC alignment layers have been deposited on both glass faces.

The SLM was assembled and filled with an experimental FLC mixture known as CDRR 4.[†] This FLC material exhibits very little bistability and is therefore unusable in 2-dimensional transmissive SLMs. It undergoes the following phase transitions when heated:



The FLC material is actually solid at room temperature and must therefore be heated until the liquid crystal enters the smectic C* phase. The SLM must be maintained at this temperature during operation without obstruction to the optical aperture. This is achieved by using a heating element that consists of a third transparent ITO covered glass plate arranged parallel to the two SLM glass faces but separated from them by a small sealed air gap. When an electric current of the order of 2A is passed through this ITO element,

[†]This high tilt FLC mixture was developed under the UK LINK collaborative project "Fast Electro-optic Effects in Chiral Smectic Liquid Crystals." The chemical structure includes siloxane side-chains (as proposed in [61]) and was synthesised at Hull by Goodby and Dong. The materials were characterised in Cambridge by A.B. Davey, who also first suggested their use as reconfigurable holograms (unpublished work by A.B. Davey and W.A. Crossland).

heat is transferred to the SLM by convection. A thermocouple is also located inside the air cavity for use with standard heat controllers.

The FLC phase transitions show that the material does not exhibit the normal nematic or smectic A liquid crystal phases. The presence of these extra phases in most display-application FLCs is believed to significantly aid in the surface-stabilised alignment of the smectic C* phase molecules. The effect of their absence was encountered during the initial efforts to align the material by cooling it slowly through the isotropic to liquid crystal transition. These attempts led to the generation of a fine granular scattering appearance due to the creation of numerous FLC domains aligned in different directions. However further attempts which included the application of a 25V peak-to-peak 1kHz square-wave signal across the entire cell during cooling, led to excellent alignment, even when the cooling rate was quite rapid. The alignment was even retained after solidification and transition back into the smectic phase, suggesting that the SLM would not need to be temperature cycled into the isotropic phase every time it was turned on.

At 55°C, the switching angle 2θ of the FLC material was measured as 63°. With this SLM device integrated into a wavelength filter, an efficiency gain of over 11dB would be obtained relative to the 2DX320IR performance. This efficiency is only 2dB lower than a full 90° switching angle would be able to achieve, but with the advantage that this FLC material may be driven fairly rapidly. The switching angle was maintained up to a frame rate of 5kHz before it began to noticeably decrease.

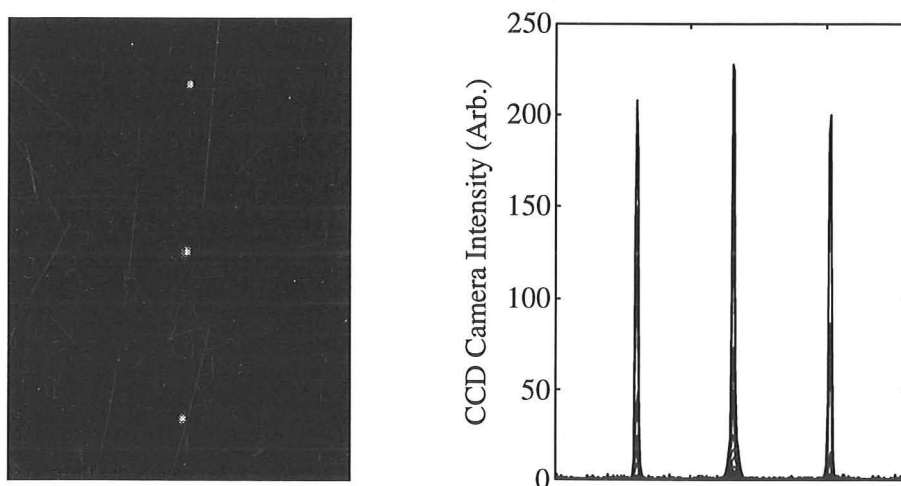


Figure 4.12: Suppression of the zero-order replay by a high-tilt FLC-SLM. Measured at $\lambda = 674\text{nm}$.

Each SLM pixel is driven from a dedicated high-voltage latch with dynamic DC balancing to achieve a zero-mean drive voltage. The control interface to these latches is still under development, but the interlaced nature of the SLM stripes means that by shorting out alternate electrodes, it is possible to display a grating and obtain an experimental replay measurement of the device performance. Figure 4.12 shows that the first- and symmetric-replay spots receive almost two-thirds of the available optical power. This is the smallest zero-order ever seen without polarisers.

4.5 Discussion

The experimental results presented in this chapter are the first known demonstration of FLC-SLM computer-generated holography and fibre interconnection at wavelengths within the fibre telecommunications band. Although the insertion loss obtained for the prototype wavelength switch was very much higher than it might have been, the demonstration results are very significant because they confirm for the first time that diffractive FLC-SLM technology can be applied in commercial fibre networks, and can be designed to be either wavelength insensitive (e.g., a one-to-any interconnect) or wavelength selective as required.

Designs for a near-optimised 1-dimensional SLM and suggestions for an aberration-free lensing system were investigated further as a means of improving the switch performance. Although it has not yet been possible to try the high-tilt 1-D SLM in a second experimental filter because the drive electronics are still being completed, the holographic replay recorded by this device has one of the highest SLM efficiencies ever obtained, with the capability of producing a switch with well under 10dB insertion loss. The FLC material used in the device has the advantage compared with other potential high-tilt materials that it is easy to align and exhibits a potential frame rate of $200\mu\text{s}$. Further measurements are required to determine its birefringence and fully optimise future devices for use at $\lambda = 1.55\mu\text{m}$. In conjunction with this 1-dimensional SLM, the Fourier transfer lens would be compatible with commercially available scanner lens designs because the optics need only 'scan' in one dimension.

To summarise, a proof-of-principle diffractive wavelength filtering switch has been proposed and constructed using a single FLC-SLM. The switch has a narrow-band Gaussian wavelength response, and may be quickly and repeatably tuned over a wide tuning range. If a

1-dimensional SLM with less effective dead-space than a normal device is employed, then the switch has a theoretical insertion loss and crosstalk similar to or slightly better than a one-to-any FLC-SLM fibre switch. The switch is capable of filtering either a single, or a number of independent WDM channels simultaneously. The latter operation is achieved by designing the hologram frames (through appropriate iterative design) to generate more than one replay angle. Provided the associated splitting loss can be tolerated, each angle has an equivalent grating pitch and corresponds to a particular filtered wavelength. The switch therefore has particular applications in the implementation of a tuneable receiver or WDM switch for network routing or configuration.

CHAPTER 5

A Single-Stage, Single-Mode Holographic Interconnect

In the context of 3-dimensional free-space optical capabilities, the simplest multiple input/multiple output network switch topology is the single-stage crossbar [89,90]. Conceptually a crossbar is just a matrix of binary crosspoint switches with N inputs and M outputs. Arbitrary any-to-any connection mapping between the inputs and outputs is achieved by simply closing the relevant crosspoints. This type of single-stage architecture is strictly non-blocking because there are always a sufficient number of crosspoints to allow all inputs to be in use simultaneously. A crossbar also has an associated ease of control whereby the entire switch may be reconfigured in a single algorithmic step. At the other extreme of switch topology, optical methods that are not based in free-space often centre around cascades of small 2×2 exchange/bypass modules [91]. By necessity, these technologies usually form multistage networks and therefore require complex software control algorithms.

Although a crossbar requires MN crosspoints and is therefore ultimately limited in scalability, considerations of the parallelism provided by optics, the simplicity of individual FLC-SLM pixels, and the simple control mechanism of crossbars, suggest that a modest free-space optical switch could best be implemented as a single-stage structure [89]. This chapter describes the design of a suitable FLC-SLM fibre crossbar. Experimental switching results have not yet been achieved because of the complexity of the optical system, but a proof-of-design model has been constructed and significant advances have been made to show that GRIN lens collimators can be used to form the required micro-optic fibre arrays.

5.0.1 Free-space crossbar structures

A dilated $N \times M$ crossbar is formed by placing N lots of 1-to- M switches back-to-back with

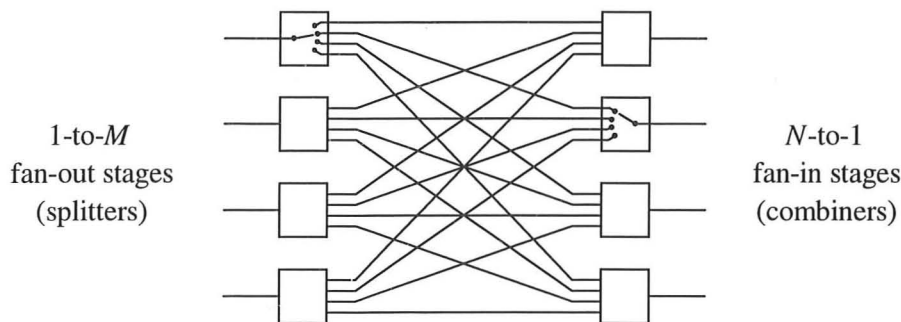


Figure 5.1: Dilated crossbar structure created from multiple one-to-any sub-blocks.

M lots of N -to-1 switches, figure 5.1. This principle has been applied to the construction of bulky opto-mechanical crossbars [92], and to the design of shuttering architectures based on the Stanford vector-matrix multiplier [93]. In particular, the OCPM (Optically Connected Parallel Machine) project [94] has demonstrated the use of an FLC-SLM as an array of intensity-mode pixel shutters (crosspoints), to form a fully interconnected free-space 16×16 optical crossbar. The project has also demonstrated a partially populated 64×64 system.

The OCPM crossbar is very powerful, but diffractive FLC switches can be polarisation insensitive and potentially have much lower insertion losses than their shuttering based contemporaries, especially as the required size of switch increases. Therefore hologram-based optical crossbars perhaps offer a better possibility for constructing simple and cheap non-mechanical switches that are capable of supporting fairly high numbers of inputs and outputs. In a holographic architecture, each block in figure 5.1 can be implemented as a single reconfigurable CGH. If the holograms behave identically wherever they are placed, then the base CGH frame set needed to interconnect $(N + M)$ lots of one-to-any sub-blocks and achieve any non-multicasting connectivity, only consists of $\max[N, M]$ holograms. The optical 'wiring' between the blocks is then a fixed logical interconnection that could be implemented either as a "rats-nest" of optical fibres, or preferably as a free-space interconnect.

5.1 The Holographic Crossbar with Passive Fan-In

The use of an FLC-SLM as a diffractive component in a crossbar switch was first suggested by O'Brien [38, 95]. The crossbar takes the form of figure 5.2, where an array of parallel single-mode input fibres are arranged in front of the SLM. Each Gaussian beam is separately collimated by a lens to illuminate some portion of the SLM plane. The SLM must be divided into N sub-hologram routing areas, such that each region is filled with a distinct

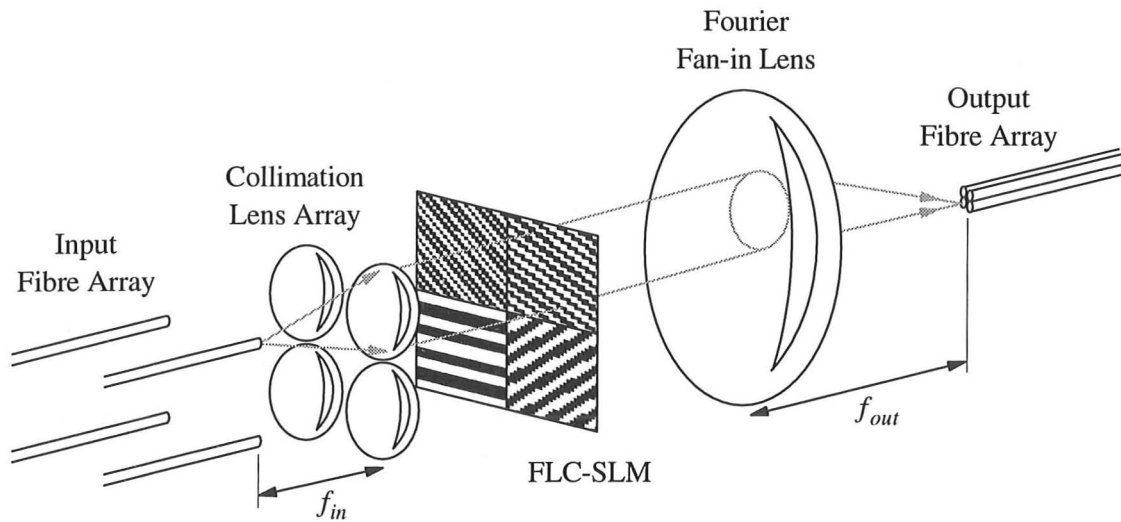


Figure 5.2: A single-pass holographic crossbar structure.

and independently controlled CGH. Each hologram deflects light from its associated input fibre towards an arbitrary output port. The architecture is therefore equivalent to a stacked array of one-to-any switches, with the exception that a single Fourier lens, rather than an array of lenses, must be used at the output to superimpose all CGH replay fields. Depending upon the physical aperture of the SLM with respect to the extent of the first-order replay field, the input fibres typically need to be sparsely arranged, whilst the output fibres must be fairly closely packed.

The O'Brien architecture operates under the condition of passive fan-in at the output fibres, i.e., there are no output 'combining' holograms to match the input 'splitter' holograms. This condition translates into the optical domain as a numerical aperture increase of the Gaussian beam angles travelling through the system. Light arriving at any particular output fibre can originate from a variety of input positions. The Fourier fan-in lens converts the offset of each input fibre from the optic axis into a different angle of arrival at the outputs. Hence although a Fourier $4-f$ configuration removes the spherical wavefront phase distortion of the replay fields,[†] residual wavefront tilts still exist on the replay spots as a consequence of the non-telecentric output imaging. If the output ports are implemented as large diameter multi-mode fibres or as an array of photodetectors, then these wavefront tilts are accepted within the large numerical aperture of the output components, and the tilts may be ignored. But if the optical transparency or crosstalk noise rejection properties of single-mode fibres are required, then the tilts will introduce large insertion losses, limiting the scalability of

[†]See section 2.2.2.

the architecture. This problem also arises in the design of all shuttering based architectures such as the OCPM crossbar.

5.1.1 $1/N$ Scalability limitation

For the crossbar of figure 5.2, the most favourable geometry in terms of the lowest average insertion loss, occurs when the single-mode output fibres are bunched close to the system axis. No excess insertion loss penalty occurs when any input fibre is also aligned along this system axis (in a geometry identical to the one-to-any switch), but maximum beam tilt is introduced from an input fibre which is positioned in a corner of the input array. Thus if the N input fibres are arranged on a $\sqrt{N} \times \sqrt{N}$ grid with Δs spacings, then the maximum transverse displacement of any fibre from the system axis is $\frac{1}{2}\sqrt{2}(\sqrt{N}-1)\Delta s$. The average offset \bar{s} of all input fibres from the axis is also of particular interest. This mean value may be calculated as a 2-dimensional summation across the entire input array:

$$\text{Mean fibre offset, } \bar{s} = \frac{\Delta s}{N} \sum_{m=1}^{\sqrt{N}} \sum_{n=1}^{\sqrt{N}} \sqrt{\left(m - \frac{\sqrt{N}+1}{2}\right)^2 + \left(n - \frac{\sqrt{N}+1}{2}\right)^2} \quad (5.1)$$

where \bar{s} is always weighted towards the edge of the array because proportionately more fibres are positioned there. $g(N) = \bar{s}/\Delta s$ is a function of N alone and is of order $O\left\{\sqrt{\frac{N}{2}}\right\}$. The value of this function is determined entirely by the physical packing of the input fibres and it is ultimately related to the optical numerical aperture that must be accepted at the outputs. For an $N = 9$ input crossbar with square-spaced fibres, $g(N) = 1.41$, and for a 64 input structure, $g(N) = 4.95$. Hexagonal and other fibre spacing arrangements may give slightly better (lower) values.

The wavefront tilt across the hologram replay spots will on average be given by:

$$\partial\theta = \tan^{-1} \left(\frac{\bar{s}}{f_{out}} \right) \quad (5.2)$$

where $\partial\theta$ is measured in radians and f_{out} is the focal length of the Fourier lens as shown in figure 5.2. Again we assume the most favourable geometry such that the collimation lenses have the maximum allowable diameter of $D = \Delta s$ and are completely filled by the $\frac{1}{e^2}$ Gaussian field intensity radii of the input beams. Substitution of the focal length f_{in} of this collimation array as obtained from equation (3.12), together with suitable single-mode

fibre parameters, (e.g., $w_o \simeq 5.25\mu\text{m}$ for $\lambda = 1550\text{nm}$), then leads to:

$$\partial\theta = \tan^{-1} \left(0.19 \frac{f_{in}}{f_{out}} g(N) \right) \quad (5.3)$$

The mean angle of the output beams is thus simply a function of N and of the ratio of focal lengths. As usual, the fibre overlap integral solution of equation (3.25) can be used to predict the output fibre launch efficiencies under these conditions. The output focal length f_{out} must be made significantly longer than f_{in} to avoid the theoretical output beam angles rapidly tending towards 90° , where the insertion loss becomes infinite. Thus the output Gaussian spot radii w'_o , must be defocused with respect to the input fibre modes of radii w_o . For nearly all practical situations, this defocus is determined by equation (5.4):

$$w'_o = \frac{f_{out}}{f_{in}} w_o \quad (5.4)$$

The defocused output spots potentially create severe crosstalk as the Gaussian tails from different inputs begin to overlap more significantly in the replay plane. They also decrease the output fibre launch efficiencies because of the mismatched Gaussian-to-fibre mode profiles in the replay. Figure 5.3(a) is a plot of the crossbar insertion loss versus the ratio of focal lengths. This plot was generated by substituting equations (5.3) and (5.4) into the overlap integral solution. The plot represents the compromise between minimisation of the output launch angles, and the need to mode-match the output spots. The uppermost shaded boundary of the figure corresponds to the minimum insertion loss of an on-axis input fibre as the system is defocused. The lower boundaries of the two shaded regions correspond to the insertion loss incurred by fibres positioned in the extreme corners of the input array, plotted here for $N = 9$ and $N = 64$ sized crossbars respectively. The two heavy black lines show the average insertion loss of these systems. The mean loss curve always exhibits a minimum, demonstrating that it is possible to design a system with an average insertion loss of slightly better than $\frac{1}{N}$ using an optimum ratio of focal lengths of just greater than \sqrt{N} . These system parameters are summarised in figure 5.3(b) for variously sized crossbars. The optimum condition occurs when all lenses in the system have the same f -number. The shaded height of figure 5.3(a) shows that the operational insertion loss of the design will vary dramatically between different input fibres. Thus the worst case loss will always be considerably greater than the mean, making passive fan-in architectures such as figure 5.2 unattractive for single-mode environments. The effects of Gaussian tail crosstalk also grow as the number of inputs is increased because of the need to scale f_{out} in proportion to \sqrt{N} .

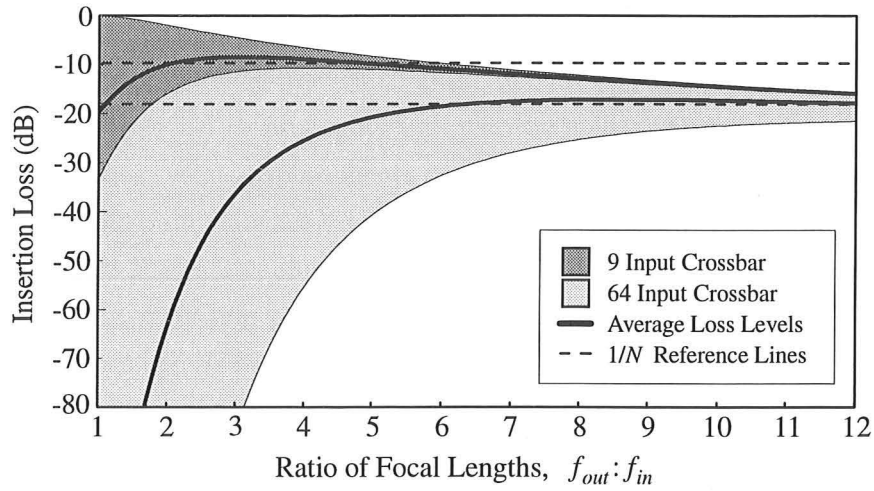


Figure 5.3(a): Insertion loss scalability of the passive fan-in FLC-SLM crossbar.

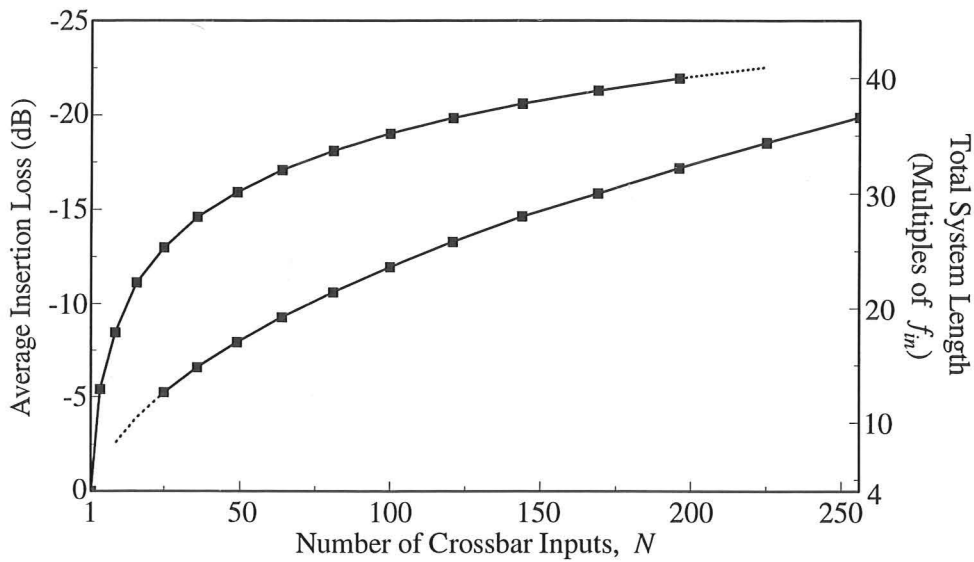


Figure 5.3(b): Optimum design parameters versus number of crossbar inputs.

The obvious solution to the crossbar fan-in problem is to remove the passive Fourier fan-in lens and reintroduce the concept of active holographic combiners. Matched hologram pairs for eliminating output angles have been implemented in fixed holographic interconnection patterns [96,97], but have never been used in dynamic reconfigurable structures other than the tuneable wavelength filter in the last chapter. In such a system, the angular holographic deflections must be allowed to propagate between the splitter and combiner planes of figure 5.1, becoming transverse displacements of the beams. The correct separation distance between the two hologram planes is set by the range of deflections that is possible from the diffractive elements. The interconnect volume therefore depends upon the minimum feature size of the hologram recording process. Fixed diffractive elements can record very small features so the planes can be in fairly close proximity. Much larger separations are required between holograms written on FLC-SLMs. The standard grating equation predicts that the maximum possible first-order SLM diffraction angle ϕ_{max} at normal incidence, is given by:

$$\phi_{max} = \pm \sin^{-1} \left(\frac{\lambda}{2d} \right) \quad (5.5)$$

where d is the SLM pixel pitch. Thus to diffract a beam from the top-left of figure 5.1 to the bottom-right, a separation distance Z between the two hologram planes is required:

$$Z \simeq \frac{2Dd}{\lambda} \quad (5.6)$$

where D is the aperture of each hologram plane, i.e., the total aperture containing all input or all output fibres. If it is assumed that each plane is implemented as a single SLM divided into sub-holograms, then using two 2DX320s with $80\mu\text{m}$ pixels and 25.6mm apertures, the interconnect length Z is of the order of several metres. This is clearly too long and too susceptible to mechanical vibrations to be acceptable in any practical application.

One method of halving the system length is to observe that a plane of symmetry exists within the optical interconnection pattern of figure 5.1, midway between the two active hologram planes. A planar mirror placed at this point folds the two hologram planes into one so that the optical signal paths are now made to and from a single array of bidirectional fibres. Although the physical volume of the crossbar has been halved, equation (5.6) shows that there is still a fundamental scalability conflict between an increased SLM aperture to support more inputs and outputs, and minimisation of this same aperture to reduce the system length and maintain a compact architecture.

5.2 The Scalable Holographic Crossbar with Active Fan-In

Figure 5.4 shows the author's suggestion of a new scalable architecture for holographically interconnecting single-mode fibres. The operation of this compact folded crossbar structure is as follows. In plane P1, light enters the system as multiple divergent Gaussian beams emerging from cleaved single-mode fibres which have been aligned parallel to the system axis. Each fibre is also positioned so that it lies along the central axis of one of the lenses within a collimation lens array. The collimation array in plane P2 is arranged exactly one focal distance in front of the fibre ends so that the Gaussian signal beams are individually collimated through the FLC-SLM. The SLM display area is then divided into distinct sub-holograms, such that every input source is deflected by a different CGH. The angular holographic beam deflections are converted into spatial offsets by means of a Fourier lens in plane P3 which focuses the beams onto a mirror's surface in plane P4. This Fourier lens effectively forms a superimposed set of replay fields. For any particular input fibre, the position of the first-order replay spot on the mirror's surface relative to the system axis, is determined by the angle of deflection of that input's sub-hologram frame.

The Gaussian beams are reflected back towards the SLM at an angle which obeys the normal law of reflection. The Fourier lens then re-collimates each light beam through a different sub-hologram region of the same FLC-SLM. During this second pass of the SLM, the output holograms must remove the beam angles and cause them to emerge parallel to the axis of the output fibres. The input and output holograms are theoretically related by a simple

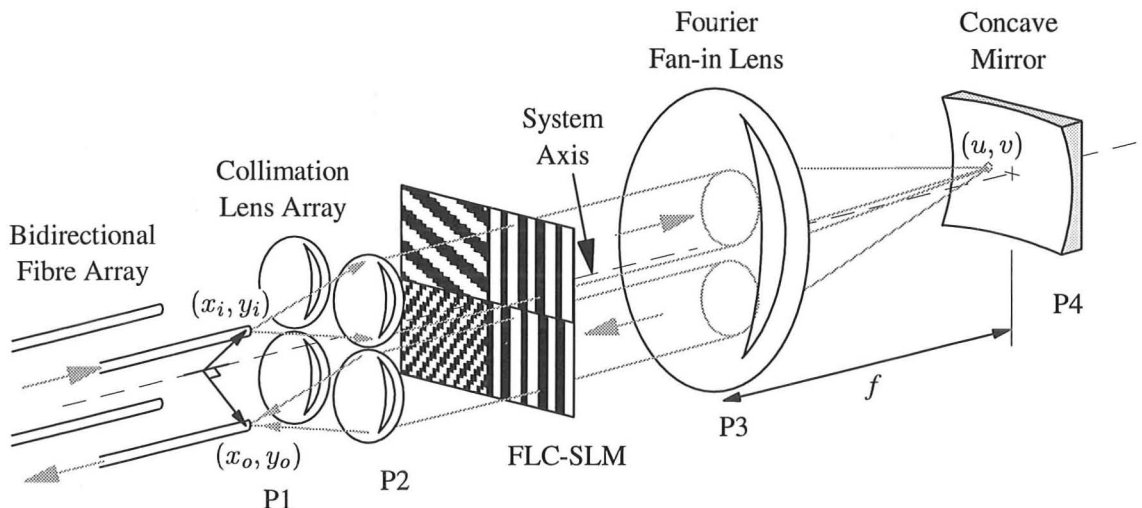


Figure 5.4: A double-pass holographic crossbar structure for single-mode fibres.

rotational symmetry (which for binary phase holograms means they can be identical), but may differ slightly in practice to compensate for imperfections in the optical system.

The resultant beams are finally refocused by the lenses in plane P2, back into the single-mode output fibres at the correct 0° launch angle. To accommodate input and output fibres within the same fibre array, the array may either be divided into separate input and output areas, or it may be assumed that every fibre may be bidirectionally connected to any other. Hence arbitrary low-loss crossbar interconnectivity between single-mode fibres is achieved by the use of matched pairs of dynamic holograms.

5.2.1 Design and optical modelling of an experimental 8×8 crossbar

Figures 5.5(a) and (b) show the results of an experimental model of a compact 16 channel crossbar, constructed using CODE V. The eventual aim is to build this design as a proof-of-principle demonstrator. The model has been based on a 2DX320 SLM optimised for $\lambda = 1.55\mu\text{m}$, and the ray-trace of the optical configuration is to scale, and corresponds exactly to the interconnect size in real life. Graded-index rod lenses of 4mm diameter, arranged in a 4×4 array with a 6.4mm pitch, have been used as the fibre collimators, and a standard Melles Griot catalogue achromatic doublet (LAI011) has been used as the $f/3.3$ Fourier lens without any further optical components for wavefront correction. The CODE V model predicts that almost aberration-free performance can be achieved (better than $\lambda/20$ flatness), even with this non-custom lens design. Figure 5.5(b) is the exit pupil wavefront function for the worst case interconnection. This limiting configuration arises when the signal from a fibre positioned in a corner of the array is optically routed back into itself.

From figure 5.4, light originating from an input fibre located at a height (x_i, y_i) above the system axis is focused to a replay spot at a position (u, v) relative to the same axis on the mirror, and returns to the output plane at a height (x_o, y_o) . The symmetry of the system implies that the replay position (u, v) required to interconnect any two fibres must be derived from a mean value:

$$(u, v) = -\frac{f\lambda}{Dd} \times \left(\frac{x_i + x_o}{2}, \frac{y_i + y_o}{2} \right) \quad (5.7)$$

where D is the SLM aperture, and $f\lambda/d$ is the width of the first-order replay. (u, v) may be more conveniently written in terms of the fractional order replay coordinate $(\sigma, \xi)^\dagger$ that

[†]See the definition in equation (3.20).

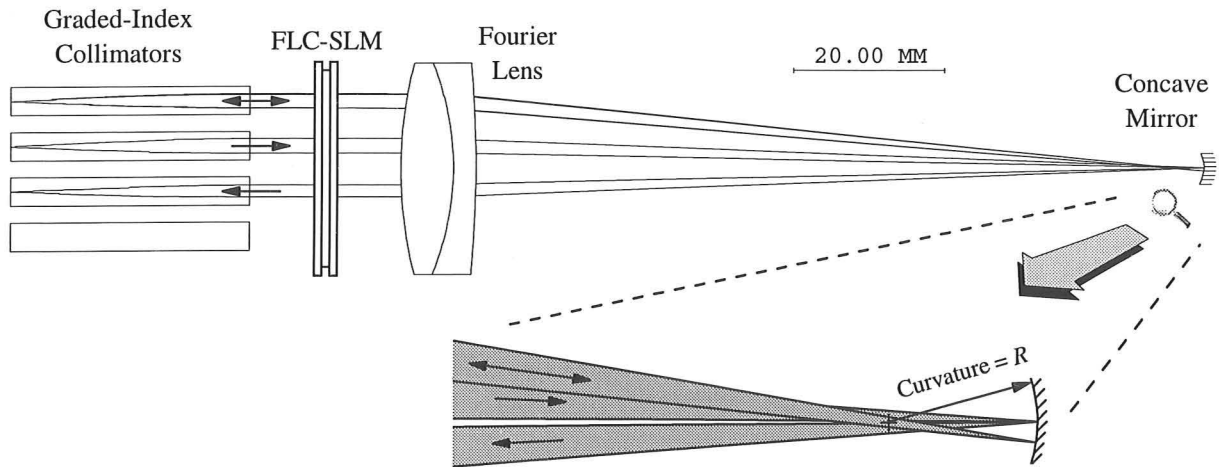


Figure 5.5(a): CODE V ray-trace of an 8x8 single-mode optical crossbar at $\lambda = 1.55\mu\text{m}$. The crossbar is shown making an arbitrary interconnection, and is plotted at a 1:1 scale.

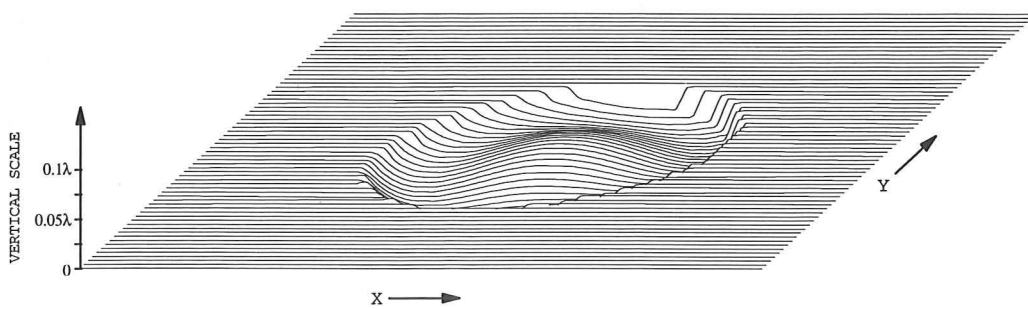


Figure 5.5(b): CODE V simulation of the worst-case exit pupil wavefront.

must be used in the design of the input and output holograms:

$$(\sigma, \xi) = -\frac{1}{2D}(x_i + x_o, y_i + y_o) \quad (5.8)$$

The simplest method of producing this interconnectivity is to introduce optical power into the mirror surface by bending it into a spherical shape. It is possible to form the crossbar interconnect using either a convex or a concave mirror surface because this simply affects the sign of equation (5.8). A concave mirror is preferable however, because it more closely follows the natural field curvature of the positive Fourier lens and minimises aberrations.

The small diameters of the replay spots on the mirror means that each spot is effectively incident upon a tilted *plane* mirror, where the angle of tilt is proportional to the height of the spot above the system axis. This tilt makes the angles of reflection greater than they would be from a planar mirror, introducing an 'optical lever' effect into the system. The lever removes all constraints on the focal length of the Fourier lens, so that any focal length can be accommodated by altering the radius of mirror curvature. This allows the volume of the system to be minimised.

The optical model was optimised by configuring the crossbar with a partially populated set of interconnection paths, carefully chosen to represent the full range of optical imaging requirements. The interconnection pattern was implemented by placing CODE V gratings of different pitches in front of each graded-index fibre collimator, derived by dividing the 2DX320 pixel pitch by the values obtained from equation (5.8). The radius of curvature of the spherical mirror was then allowed to be an optimisation variable, and the air-spacings were varied in a systematic manner that was as similar as possible to experimental alignment procedures.

The centre of curvature of the spherical mirror surface must intersect the principal ray from any looped-back input (see detail in figure 5.5(a)). This leads to an ideal mirror radius of curvature R , predicted by:

$$R = \frac{f^2 \lambda}{Dd} \quad (5.9)$$

where f is the focal length of the Fourier lens, and D , d are the SLM aperture and pixel pitch respectively, as before. Equation (5.9) is based on a $2-f$ imaging system between the

SLM and the concave mirror. But if the mirror is curved slightly further, then it is possible to directly compensate for the spherical wavefront phase curvature normally associated with the Fourier replay of a $1-f$ transfer lens. Thus with the FLC-SLM placed immediately in front of the lens as shown in the model, the required radius of curvature of the mirror becomes:

$$R = \frac{f^2 \lambda}{Dd + f \lambda} \quad (5.10)$$

The theoretical radius of curvature for the optical elements used in the design of figure 5.5(a) is $R=7.213\text{mm}$ for an interconnect volume of less than 82cm^3 . This agrees very closely with the $R=7.218\text{mm}$ value obtained from the CODE V model. Equation (5.10) is very significant because it demonstrates that only the radius of curvature of the final spherical mirror has to vary as the crossbar aperture D is increased, rather than the Fourier lens focal length. The radius R is also only weakly dependent upon D , and the mirror actually flattens as the density of SLM pixels is increased — as would occur when using a 2-dimensional silicon backplane device instead of a passive SLM for example. This system property has important implications because it means that the holographic aperture, and hence the number of crossbar channels, can be scaled almost arbitrarily without affecting the system length.

The length of a crossbar with active fan-in will typically be much shorter than either the original passive fan-in architecture, or the simple interconnect length Z from equation (5.6). In fact, the length is only limited by the degree of optical aberration that is acceptable. The optics are thus potentially scalable to very large holographic apertures, where the possibility of placing several SLMs within a single crossbar begins to arise. Such a switch would be capable of routing a very large number of channels ($\gg 1 \times 10^3$), and breaks the limits imposed by the physical sizes of practical FLC-SLMs in terms of number of pixels.

As a theoretical example of the capability of a single polarisation insensitive SLM, consider that an ideal device with $30\mu\text{m}$ pixels and a $D=30\text{mm}$ aperture would be capable of interconnecting 900 telecommunications fibres (e.g., a 450×450 crossbar) arranged on a 1mm array pitch. This hugely parallel interconnection could be fairly easily achieved using an $f/4$ Fourier lens and a spherical mirror of diameter 6.2mm and curvature $R=20.6\text{mm}$. The total optical length between the 900 fibres and the mirror would then be slightly longer than $f=120\text{mm}$, giving a modest density of optical connection of about $8 \text{ beams}/\text{cm}^3$ within a total optical volume of about 110cm^3 .

5.3 Microlens Arrays

Various runs of the crossbar model have revealed that the imaging quality of the system is likely to be limited by the performance of the fibre collimation lens array, rather than by the bulk Fourier lens design. Careful consideration of the planar array of collimating lenses is therefore an essential part of the optical design process. Each lens must be aligned along the axis of its respective fibre and must be matched to the fibre numerical aperture. The collimated beams must illuminate an adequate number of SLM pixels to ensure accurate replay of the crossbar holograms. Too few pixels would lead to the generation of noisy replay fields, especially in the presence of beam misalignments due to manufacturing tolerances. For an FLC-over-silicon SLM with $50\mu\text{m}$ pixels, Gaussian beam diameters of the order of 1mm ($\frac{1}{e^2}$ intensity) are required to cover enough SLM pixels and support usefully large numbers of crossbar channels. In addition, the array lens diameters should not be significantly wider than the beams they produce to avoid wasting the SLM pixel area.

The above requirements exclude the use of conventional bulk lenses and indicate the necessity of using a microlens array. Microlens technology may be broadly split into three categories: diffractive, refractive, and graded-index lenses. Diffractive Fresnel lenses are typically formed by etching a number of phase steps into an optical glass flat. This is an attractive approach because it is possible to tailor the lens design to the particular application. However multi-level lenses are very difficult to manufacture accurately, and although up to 8 phase levels have been reported [98], the phase and spatial quantization of the lenses still make them prone to high-order diffraction noise. This noise will tend to cascade through the optical system, so that diffractive lenses are probably inappropriate as fibre collimators at the very front end of the crossbar.

Refractive microlens arrays are usually formed by depositing 'blobs' of polymer onto a glass slide. The glass is then heated until the polymer melts, and surface tension pulls the blob into a plano-spherical lens. This technique has been used to form some very high quality lens arrays [99]. Unfortunately, polymer lenses with diameters greater than about $200\mu\text{m}$ tend to collapse in the middle during the melt. One possible method of creating larger collimated beam diameters is to follow the array of small polymer lenses with a telescopic magnification stage [100], but this will not produce a compact architecture. Glass coupling spheres [101] and even small singlet lenses have been used as alternative fibre collimators, but the formation of a mechanically stable array of such lenses would be difficult.

Both diffractive and refractive lens arrays have to be precisely aligned parallel to the plane of the input fibre array, but air-spaced from it. This is a considerable alignment problem that imposes tight tolerances on the manufacture of both these components. Graded-index rod lenses (GRINs) offer a simple solution to this problem [102–104] because the lens focus can coincide exactly with one polished face of the rod, whilst the collimated beam emerges from the opposite face. Each input fibre can thus be accurately aligned and glued to its respective GRIN. This alignment could be automated in a manufacturing process because it is required on a repetitive ‘per lens’ basis. In addition, the final task of packing all the rods into the array structure has now been separated from the assembly of the fibre collimators. The denser GRIN refractive indices mean that the length tolerances on the rods and on the axial alignment between inputs throughout the array, are far less critical than for the original air-spaced lenses. The SLM holograms may of course be used to compensate for any variations in the lens array pitch as usual. GRINs have already been used as high quality lenses to couple light between single-mode fibres, with losses as low as -0.2dB [105]. GRINs are typically a few millimetres in diameter and they currently represent the only practical means of constructing the collimation array optics for these types of FLC-SLM crossbar.

5.3.1 Theory of GRIN lenses

Graded-index lenses (GRINs) act as inhomogeneous circular waveguides and are very similar to the glass preforms that are pulled down to small diameters during the manufacture of optical fibres. A thorough analysis of GRIN properties can be found in Sodha and Ghatak [106], but the salient results are presented here. GRIN lenses usually consist of a glass rod of material containing small dopant ions such as Li^+ , to give a base refractive index of n_o . The graded refractive index profile is then formed through an ion-exchange process whereby larger ions such as Na^+ or K^+ diffuse into the glass edges and reduce the local refractive index according to their concentration. The resultant radial index profile $n(r)$ takes a general form:

$$n^2(r) = n_o^2 \left\{ 1 - (gr)^2 + h_4(gr)^4 + h_6(gr)^6 + \dots \right\} \quad (5.11)$$

where r is the radial distance of any point from the central axis of the GRIN rod, g is a gradient constant typically quoted in mm^{-1} , and h_4 etc. are higher order profile constants.

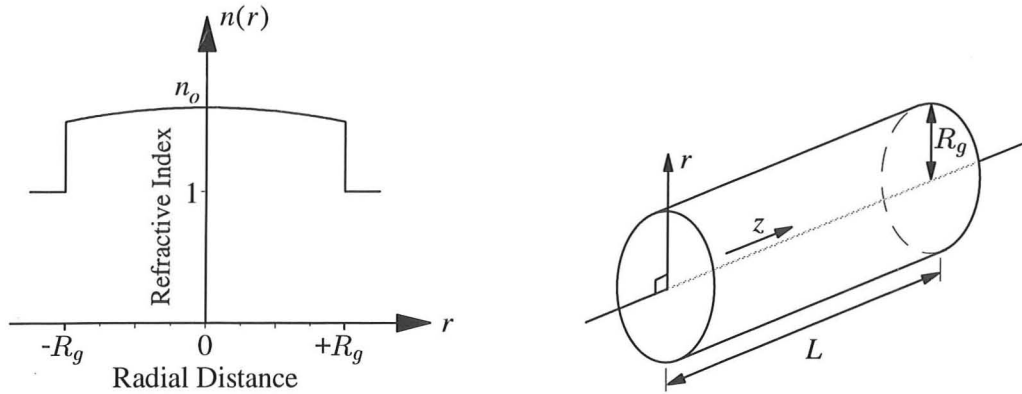


Figure 5.6: Selfoc GRIN index profile and lens geometry.

Most GRINs of interest closely follow a parabolic Selfoc (self-focusing) index:

$$n^2(r) \simeq \begin{cases} n_o^2(1 - g^2 r^2) & \text{for } |r| \leq R_g, \\ 1 & |r| > R_g. \end{cases} \quad (5.12)$$

where R_g is the radius of the GRIN, and the refractive index of the surrounding air is 1. The higher order terms are assumed to be negligible. Provided $R_g \ll \frac{2}{g}$, the optical field will always remain well confined within the centre of the GRIN and the effect of the pupil edge at $r = R_g$ will be negligible. Figure 5.6 shows a typical Selfoc GRIN lens index profile and its optical configuration. Light passes along the axis of the lens in the z -direction of propagation such that the transverse (x, y) field in any plane must satisfy a modified version of the scalar wave equation. Provided the radial variation of the glass dielectric constant $\epsilon_r(r) = n^2(r)$, is very small across the distance of one wavelength, the Fresnel integral from equation (2.8) may be used with an appropriate Kernel propagation function in (5.13), to predict the evolution of a wavefront through the GRIN [106]:

$$K(x, y, z; x_o, y_o) = \frac{\exp \left[jkn_o \left(z + \frac{g(x^2 + y^2)}{2 \tan(gz)} \right) \right]}{j\lambda \frac{\sin(gz)}{n_o g}} \exp \left[jkn_o \left(\frac{g(x_o^2 + y_o^2)}{2 \tan(gz)} - \frac{g(xx_o + yy_o)}{\sin(gz)} \right) \right] \quad (5.13)$$

where k and λ are the free-space wavenumber and wavelength respectively. As with free-space propagation, Gaussian TEM_{00} waves are exact solutions of Selfoc GRIN media. Thus if a Gaussian waist of radius w_o is incident upon one face of the GRIN rod, the beam will

remain Gaussian, with a beam radius $w(z)$ and phase wavefront radius of curvature $R(z)$:

$$w(z) = \sqrt{\frac{-\lambda}{\pi n_0 \operatorname{Im}\{Q(z)\}}} \quad , \quad R(z) = \frac{1}{\operatorname{Re}\{Q(z)\}} \quad (5.14)$$

$$\text{where} \quad Q(z) = g \frac{Q_o - g \tan(gz)}{g + Q_o \tan(gz)} \quad \text{and} \quad Q_o = \frac{-j\lambda}{\pi n_o w_o^2}$$

The Gaussian beam sinusoidally oscillates between a maximum and a minimum diameter as it propagates [107]. A flat waist, i.e., $R(z) \rightarrow \infty$, exists at both these extremes and the pitch P of the lens is defined as the GRIN length required for a full sinusoidal beam path to be completed. With a single-mode fibre glued to the input GRIN face, the minimum length required for the Gaussian beam to oscillate from w_o to its larger collimated waist is thus $0.25P$. To achieve this collimation condition, the GRIN should be cut and polished to a length L given by:

$$L = 0.25 \times P = \frac{\pi}{2g} \quad \implies \quad w(L) = \frac{\lambda}{\pi n_o g w_o} \quad (5.15)$$

where $w(L)$ is the collimated Gaussian radius that emerges into free-space.

5.3.2 Experimental characterisation of GRIN collimators

Having chosen GRINs as the best microlens technology, the next stage in the construction of the proof-of-principle crossbar demonstrator is to assemble a number of single-mode fibre collimators to use as inputs and outputs. Only two commercial manufacturers of GRIN lenses exist at the present time, these being Nippon Sheet Glass [108] and Gradient Lens Corporation [109]. The collimated beam radius $w(L)$ generated by any of the available GRIN glasses is found to be approximately half the GRIN radius. It was decided that the largest collimated Gaussian beam radius of $500\mu\text{m}$ provided by the Nippon collection of lenses would not illuminate sufficient numbers of $80\mu\text{m}$ SLM pixels. Fibre collimators were therefore assembled based on 4mm diameter BIG-GRINTM lenses from Gradient Lens Corp.

The mechanical construction of the collimators has been designed as a modified version of recent semi-commercial fibre-GRIN mounts.[†] Each BIG-GRIN is placed in a metallic

[†]The collimators referred to contain Nippon GRIN lenses, and are out-sourced by Nippon to Meteor Optics [110]. They are believed to be available as non-catalogue items from Spindler & Hoyer [111].

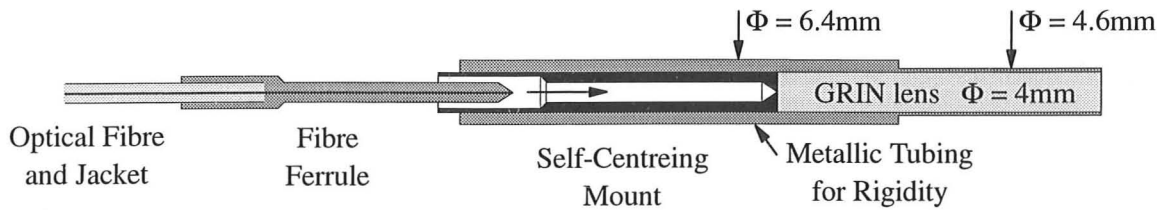


Figure 5.7: Mechanical drawing cross-section of the custom fibre-GRIN collimators.

tube for support, and the single-mode fibre is mounted in a separate self-centreing ferrule, figure 5.7. The mount is designed with a 6.4mm outer diameter to enable square-packing of 16 collimators within the $(25.6\text{mm})^2$ aperture of the crossbar SLM. All mechanical tolerances are $\pm 10\mu\text{m}$, and the polished Corning Coreguide fibre end ($w_o \simeq 5.25\mu\text{m}$ at $\lambda = 1.55\mu\text{m}$) is in contact with the GRIN. The only unknown design variable is the length of GRIN lens required to achieve collimation of the fibre TEM_{00} field. From equation (5.15), this length depends only on the gradient constant g . It must be experimentally determined in this case because of the lack of data for the BIG-GRIN glass at $\lambda = 1.55\mu\text{m}$ wavelength.

Various techniques exist for determining the refractive index profiles of fibres [112–114], but these methods require specialist equipment and calibration, and are of uncertain accuracy when applied to GRIN lenses. A beam intensity profiling approach was therefore adopted and developed by the author for determining n_o and g . The technique assumes that the beam is Gaussian or near-Gaussian in nature, and it uses a numerical analysis approach to extract the beam parameters and determine the degree of collimation in terms of milliradians (mrad) of convergence or divergence. Using an informed guess based on data at $\lambda = 633\text{nm}$, two collimators were assembled with GRIN lengths of 32.55mm and 32.95mm respectively. The first of these devices exposed manufacturing problems and produced a severely distorted output beam when light at $\lambda = 1.55\mu\text{m}$ was launched down the fibre into the lens. This distortion is believed to be due to compression and possible skewing of the fibre end at the GRIN face. The second collimator produced a high quality Gaussian output beam.

Transverse profiles of the emerging Gaussian beam were captured using a MicronViewer-7290 infrared camera from Electrophysics, connected to an 8-bit digitizing frame grabber. The camera uses an electron-scanned photoconductive lead-oxysulfide detection screen and outputs 512 lines of composite video data, sampled by the frame grabber at a horizontal resolution of 768 pixels. The effective pixel capture size of the system was calibrated by

imaging a resolution target onto the camera screen, and was found to be $17.6\mu\text{m}$ vertically and $14.9\mu\text{m}$ horizontally. An accuracy of $\pm 0.5\mu\text{m}$ was determined by performing a similar calibration with visible light for a CCD camera that had a known pixel size.

The Gaussian beam emerging from the 32.95mm long GRIN was converging, and time-averaged intensity profiles were captured at 5mm increment distances from the end of the collimator until the position of minimum beam radius had been exceeded. This process generated 65 frames of data. Each frame was then analysed to extract the Gaussian beam width, allowing a picture of the wavefront evolution to be built up. The analytical process applied to each frame was sophisticated and was based upon a numerical library non-linear least-squares fitting algorithm [115]. The procedure is summarised below:

- (1). Locate the point of maximum intensity within the frame capture and make an initial least-squares fit of 1-dimensional Gaussian curves through this point along the two orthogonal axial directions.
- (2). Using the parameters obtained from step (1), isolate the portion of the frame capture that contains 90% of the optical power. This step ensures that camera noise in dark regions of the frame capture does not distort the final fitting procedure.
- (3). Using the parameters obtained from step (1) as initial values, make a 2-dimensional Gaussian curve fit to the frame region isolated in step (2). The curve fitted to the frame has six free variables $\varphi_1 \dots \varphi_6$, but only the first two are of interest. These represent the beam radii in orthogonal directions. The other four parameters facilitate an accurate fit, but are of no further significance. The fitted curve takes the form:

$$I_{fit}(x, y) = \varphi_6 + \varphi_5 \exp \left[-2 \left\{ \left(\frac{x - \varphi_3}{\varphi_1} \right)^2 + \left(\frac{y - \varphi_4}{\varphi_2} \right)^2 \right\} \right] \quad (5.16)$$

where (φ_1, φ_2) are the x - and y - Gaussian beam widths,

(φ_3, φ_4) are x - and y - Gaussian peak coordinate offsets,

φ_5 is a normalisation term to represent the camera gain level,

φ_6 is a DC offset term to represent the camera dark level.

The 1-dimensional curve fit in step (1) consistently returns values that overestimate the Gaussian beam width by a few percent. The additional steps in (2) & (3) improve the ac-

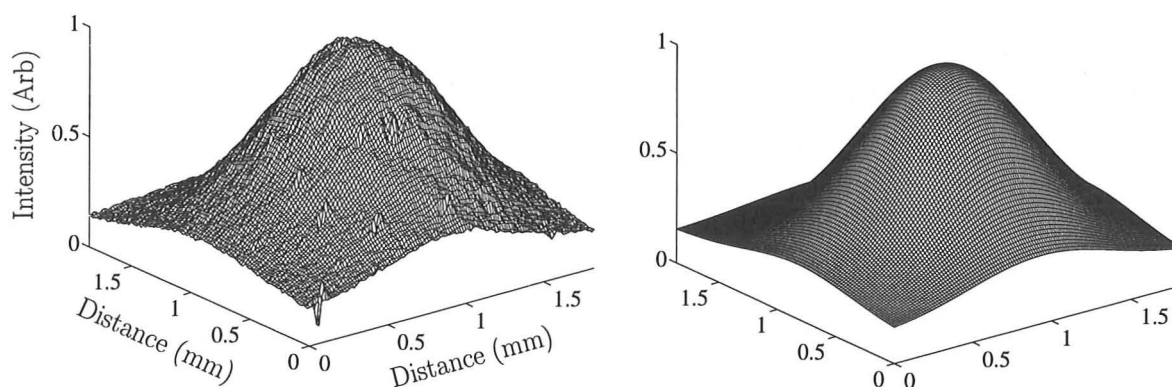


Figure 5.8(a): Experimental frame-capture profile and Gaussian beam fit of the light emerging from a fibre-GRIN collimator. The frame-capture is located 25mm from the end of the collimator, and the fitted Gaussian diameter is 1.822mm.

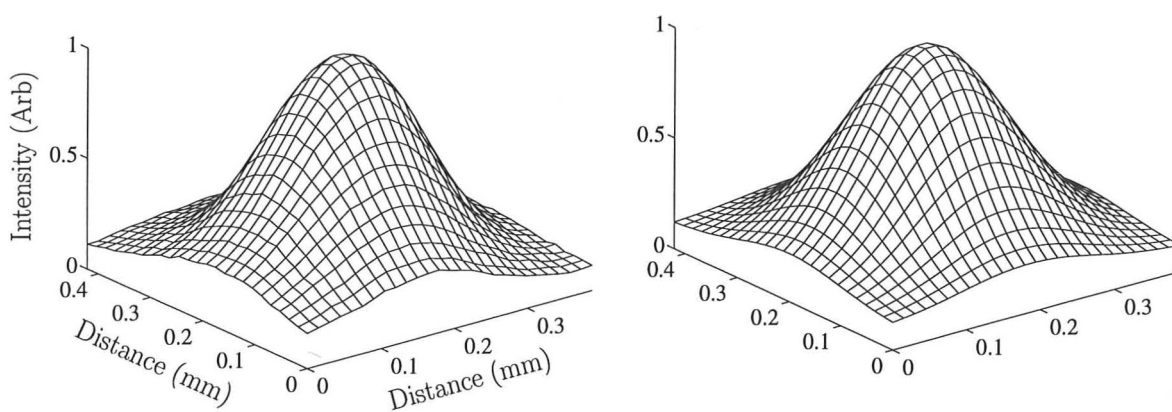


Figure 5.8(b): Experimental frame-capture and Gaussian fit in the plane of minimum beam radius. The frame-capture is 225mm from the collimator and the fitted Gaussian diameter is 0.373mm.

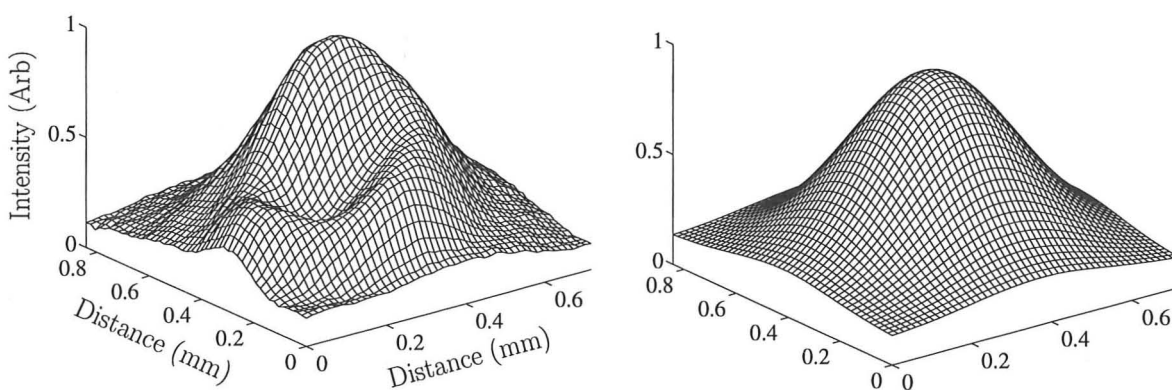


Figure 5.8(c): The experimental beam profile begins to exhibit distortion beyond the plane of minimum radius. The frame-capture is 300mm from the collimator and the least-squared error fit Gaussian diameter is 0.746mm.

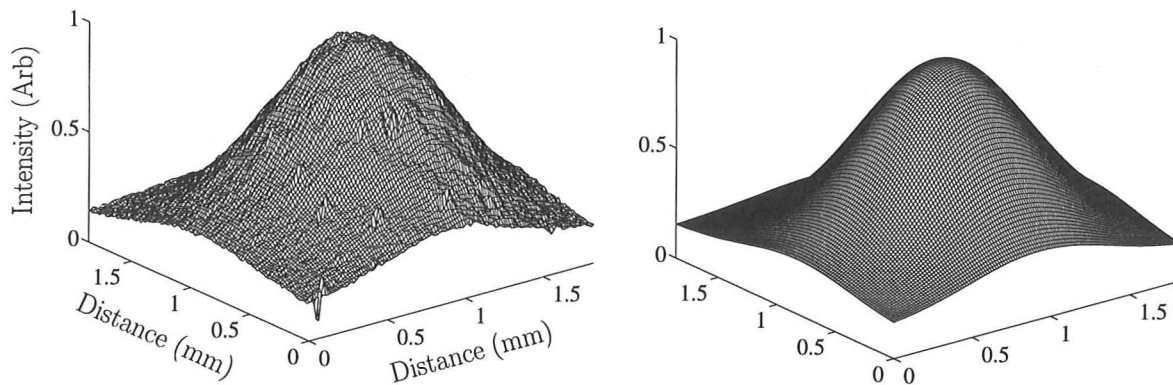


Figure 5.8(a): Experimental frame-capture profile and Gaussian beam fit of the light emerging from a fibre-GRIN collimator. The frame-capture is located 25mm from the end of the collimator, and the fitted Gaussian diameter is 1.822mm.

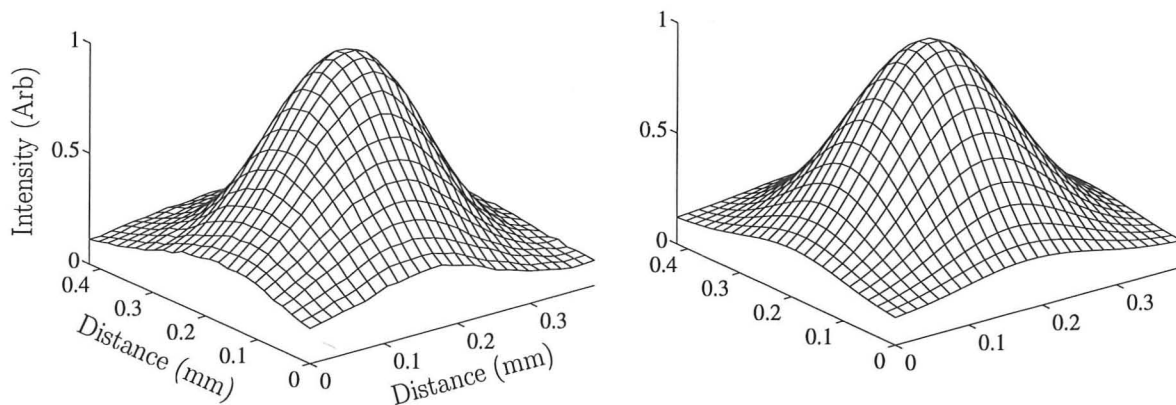


Figure 5.8(b): Experimental frame-capture and Gaussian fit in the plane of minimum beam radius. The frame-capture is 225mm from the collimator and the fitted Gaussian diameter is 0.373mm.

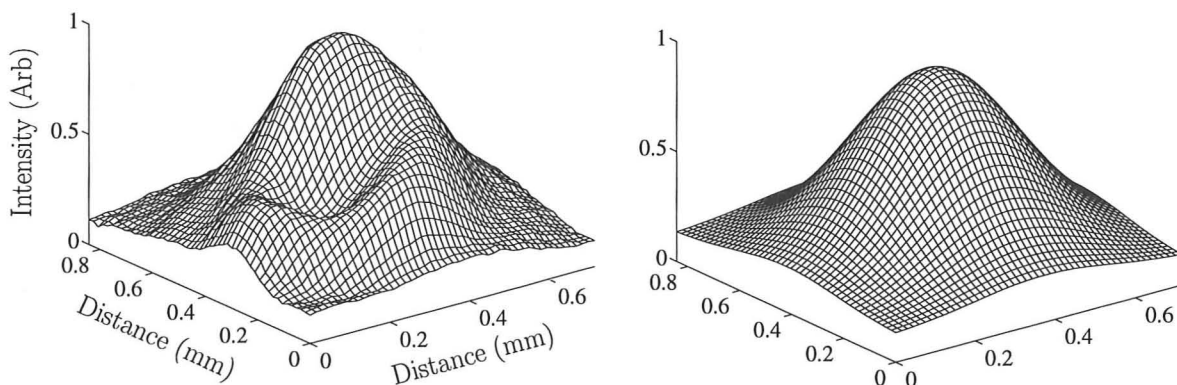


Figure 5.8(c): The experimental beam profile begins to exhibit distortion beyond the plane of minimum radius. The frame-capture is 300mm from the collimator and the least-squared error fit Gaussian diameter is 0.746mm.

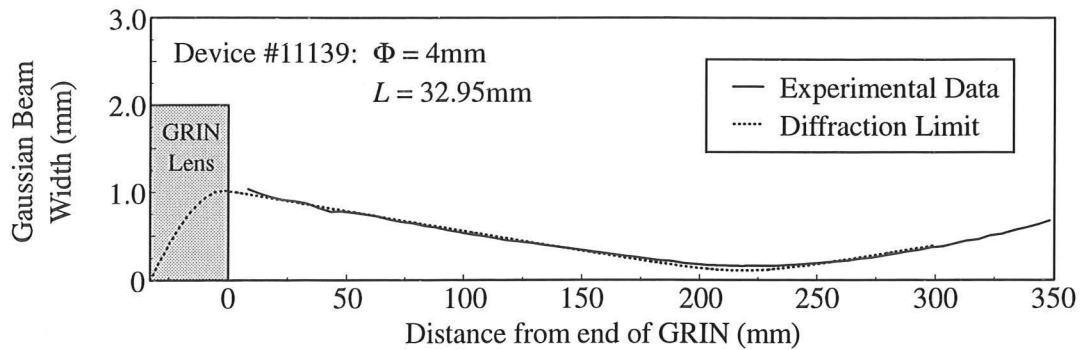


Figure 5.9: Evolution of the Gaussian wavefront emerging from a fibre-GRIN collimator.

curacy of the algorithm, returning perfect answers when applied to test frames, and making the procedure robust against the effects of noise in the Gaussian tails. The experimental frames were all processed in about 30 minutes using a fast 486DX2 PC computer. Figure 5.8 shows a representative sample of the captured beam profiles and the results of the Gaussian fitting procedure. The left-hand plots show the capture profiles that have been isolated by step (2) of the algorithm. The camera dark level is about 0.1. Figures 5.8(a)&(b) respectively show the beam profile directly in front of the collimator, and the minimum diameter waist at a distance of 225mm from the collimator. The experimental profiles are well fitted by the Gaussian functions in both cases, with a summed error power of less than 6% of the total optical power. Figure 5.8(c) shows the beam starting to distort as it propagates beyond the waist, with the fit error increasing to 10%. This is due to phase distortion in the Gaussian waist, probably caused by mechanical stresses within the collimator unit or by discontinuities in the GRIN doping profile. It is yet to be determined what effect these will have on the fibre crossbar insertion loss.

The final stage of the GRIN characterisation is to plot the evolution of the beam width as it propagates forward, and attempt to match its behaviour to a diffraction-limited TEM_{00} . Equations (5.14) and (2.5) describe the propagation of a diffraction-limited Gaussian through the GRIN, and out into free-space respectively. By varying the numerical estimates of n_o and g , a least-squared error fit can be made between these equations and the beam radii estimated from the frame captured profiles. The result is shown in figure 5.9, where the solid line represents the mean of the x - and y -radii determined by Gaussian curve fitting, and the dotted line shows the best fit diffraction-limited propagation. Deviation from diffraction-limited performance only occurs near to the waist where the experimental beam does not form as small a spot as expected. This phenomenon is commonly observed in beam analysis

because phase distortions tend to become more apparent at the waist, causing the beam to spread out.

Investigations reveal that varying n_o affects the diameter of the diffraction-limited beam, and varying g only affects its divergence. The value of g that is obtained for the GRIN material from the gradient of the equation fitting procedure is therefore insensitive to any measurement offset errors and to random noise. The estimated graded-index glass parameters are summarised in the table below, including comparative results from the original GRIN collimator that produced the badly distorted beam. Although the first line of the table is unreliable and there is a large discrepancy between the estimated values of on-axis refractive index n_o , the two values of gradient constant g agree within 2%. From equation (5.15), these figures predict with an accuracy of $\pm 0.6\text{mm}$ that future GRIN lens collimators should be polished to a length of 31.17mm. Such a lens should collimate to ± 1.6 mrad of divergence or better, and a further iteration of the procedure presented here could be used to obtain even better collimation.

	n_o	g	Divergence
Collimator 1 (distorted), $L = 32.55\text{mm}$	1.65	51.46 m^{-1}	-5.9 mrad
Collimator 2 (Gaussian), $L = 32.95\text{mm}$	1.83	50.39 m^{-1}	-4.6 mrad

Table 5.1: Summary of the estimated BIG-GRIN graded-index glass parameters.

5.3.3 Experimental demonstration of superimposed replay fields

To demonstrate the generation of multiple independently controlled replay fields for free-space crossbars, a further four fibre-GRIN collimators with characteristics similar to fig-

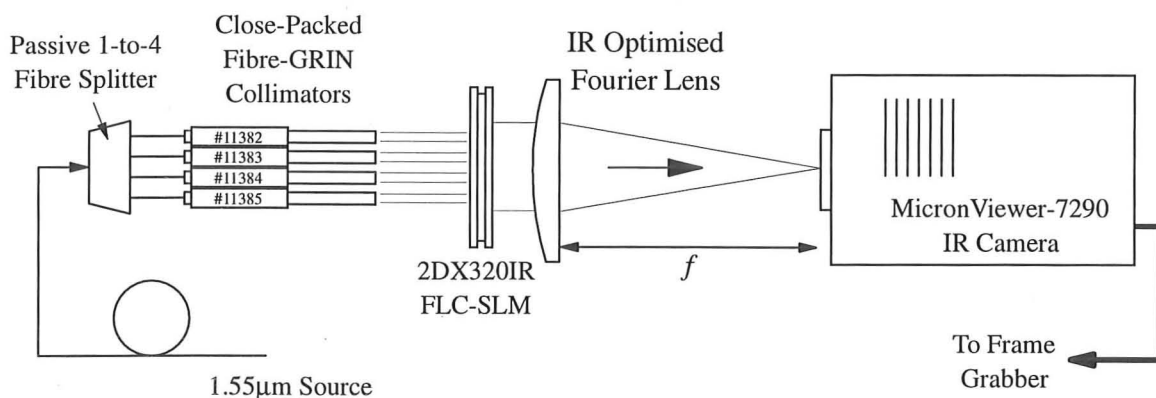


Figure 5.10: An experimental fibre-to-camera crossbar configuration.

ure 5.9 were assembled and arranged in a row. This array was then incorporated into the optical configuration shown in figure 5.10. Each of the four beams was deflected by a separate 80x80 pixel region of the 2DX320IR SLM. This transmissive FLC device has 80 μ m pixels, a 28° FLC switching angle, and exhibits a peak response around $\lambda = 1.1\mu$ m wavelength. A bulk doublet lens optimised for $\lambda = 1.55\mu$ m was used to form and superimpose the individual replay fields, and the replay plane was viewed with the MicronViewer camera.

Figure 5.11 is a camera image of the array of Gaussian beams that were incident upon the SLM. The figure also shows the four 80x80 pixel holograms that were displayed on the 2DX320IR device during the experiment. The holograms were designed with fractional order replay coordinates (σ, ξ) of (0.125,0), (0.25,0), (0.375,0) and (0.5,0) from left to right respectively. These holograms place the replay spots in close vicinity along a straight line to test the alignment and imaging quality of the system.

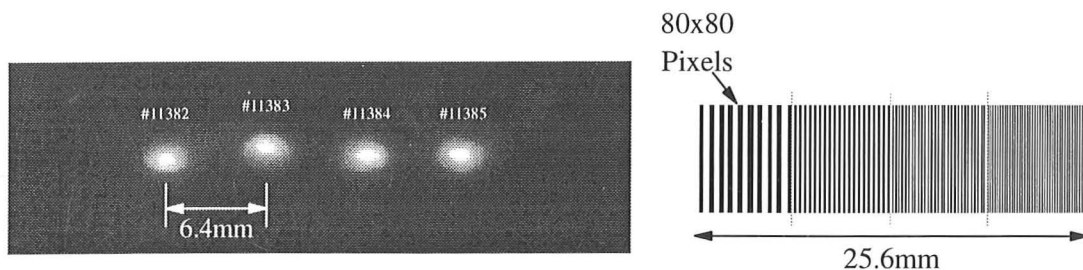


Figure 5.11: The array of Gaussian input beams and associated sub-hologram patterns.

The resultant replay plane intensity distribution is shown in figure 5.12(a). The large combined zero-order has been masked out from this image for clarity, and the four replay spots and their symmetries are clearly resolved. The imperfect alignment of collimator #11383, visible in figure 5.11, has not displaced the location of the associated replay spots. The misalignment is therefore purely a transverse offset, with no angular component.

The differences between the four replay spot intensities are due to: unequal optical power splitting of up to 1.2dB from the 1-to-4 passive fibre coupler used to supply the four fibre-GRIN collimators (see figure 5.10); variations between the four simulated hologram efficiencies; and slight differences in the focusing of the different replay fields, causing spot spreading and flattening. Figure 5.12(b) shows line profiles through each of the replays with the other three beams apertured out. Calculations of the optical system predict that the

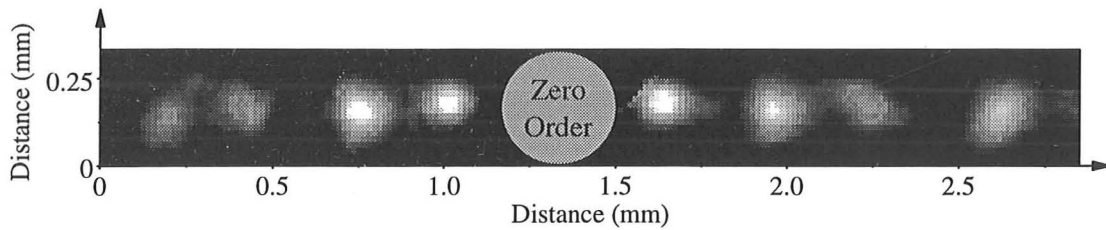


Figure 5.12(a): Camera image of the four optically superimposed replay fields.

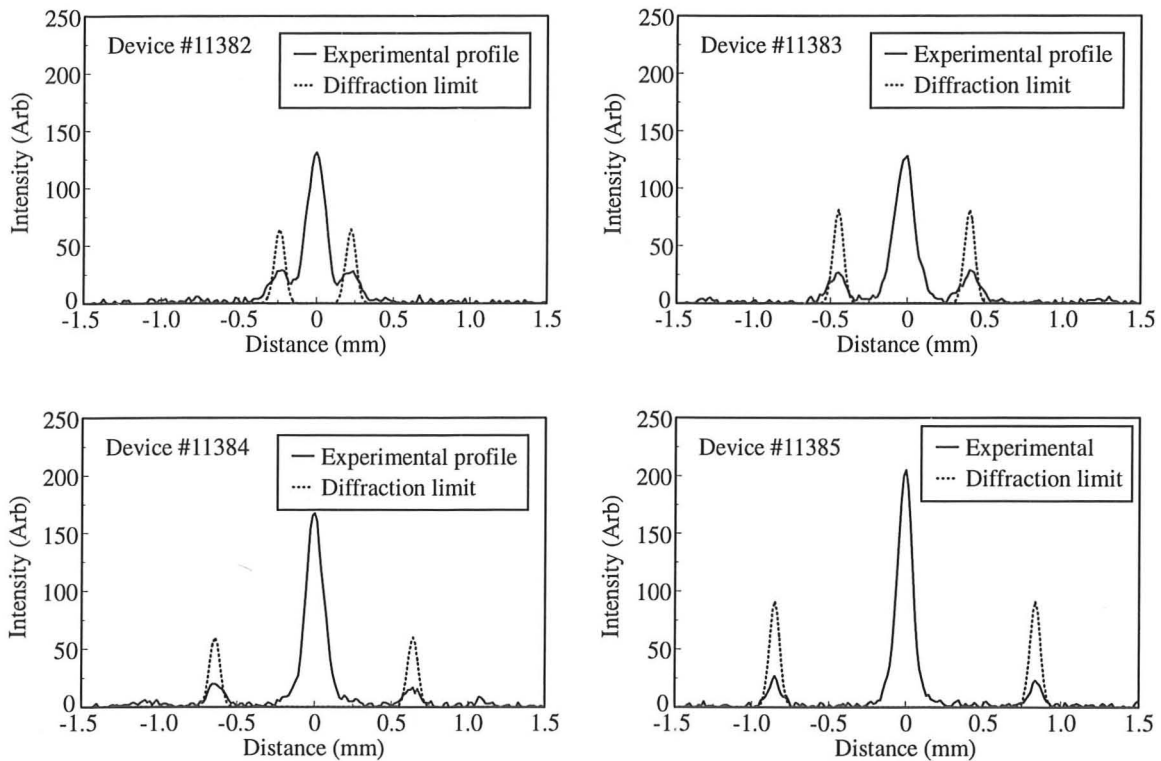


Figure 5.12(b): Line profiles of each replay and the corresponding diffraction-limits.

replay spots should all have Gaussian radii of $w_o \simeq 67\mu\text{m}$. The experimentally achieved radii were estimated by fitting Gaussian functions to the captured data. The fitted data was used to find the optical power in each spot, and then used to normalise the corresponding diffraction-limited Gaussian profiles which are overlaid on figure 5.12(b) as dotted lines.[†] The replay spots have Strehl ratios of 0.45, 0.35, 0.33 and 0.30 for collimators #11382 through #11385 respectively. Although these ratios are fairly low, the overlap integral solution in equation (3.25) predicts that the theoretical drop in single-mode launch efficiency for these replays would be only 0.67dB, 1.10dB, 1.25dB and 1.51dB respectively, assuming the spots are Gaussian.

[†]Note that the diffraction-limits for the zero-orders have been omitted.

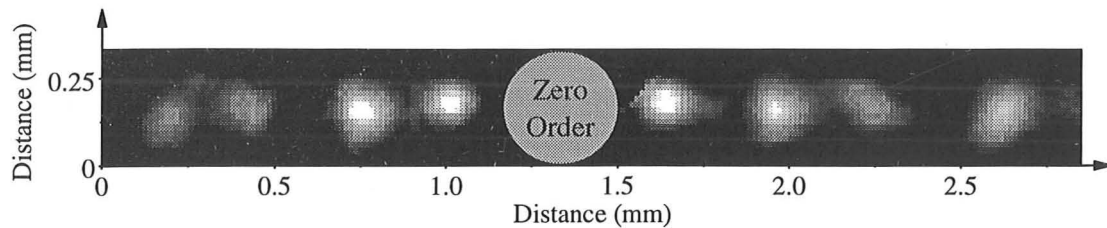


Figure 5.12(a): Camera image of the four optically superimposed replay fields.

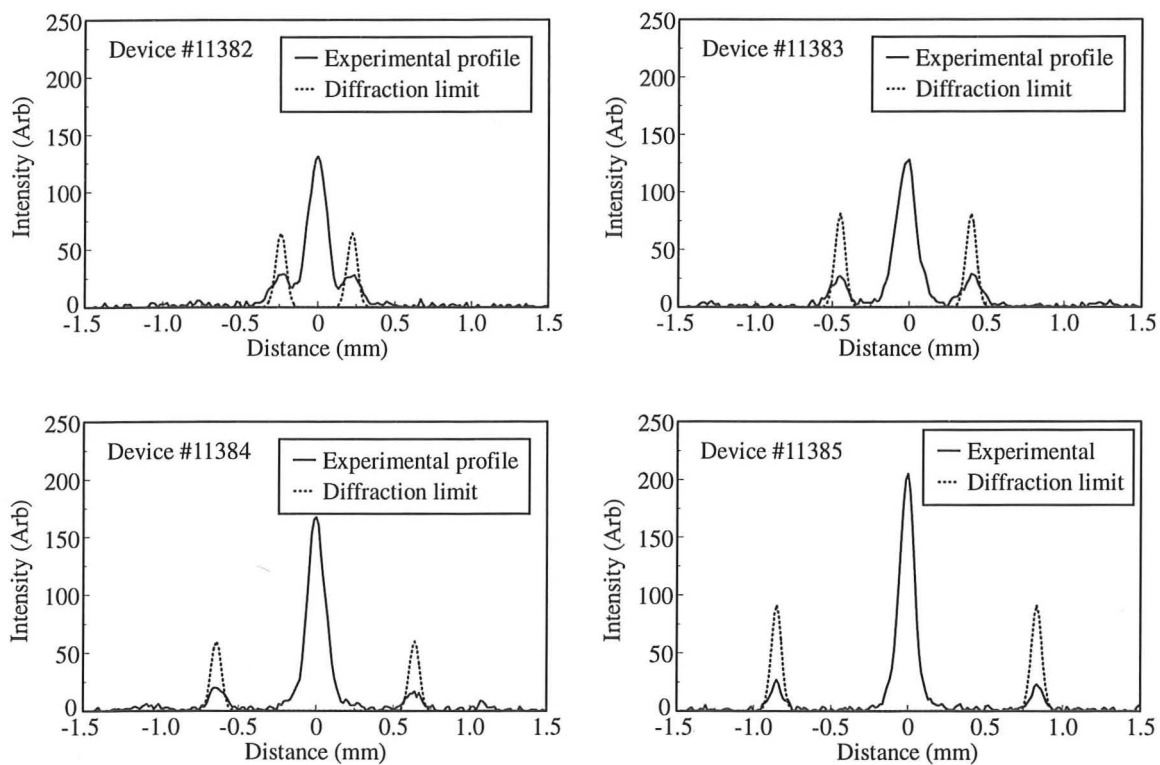


Figure 5.12(b): Line profiles of each replay and the corresponding diffraction-limits.

replay spots should all have Gaussian radii of $w_o \simeq 67\mu\text{m}$. The experimentally achieved radii were estimated by fitting Gaussian functions to the captured data. The fitted data was used to find the optical power in each spot, and then used to normalise the corresponding diffraction-limited Gaussian profiles which are overlaid on figure 5.12(b) as dotted lines.[†] The replay spots have Strehl ratios of 0.45, 0.35, 0.33 and 0.30 for collimators #11382 through #11385 respectively. Although these ratios are fairly low, the overlap integral solution in equation (3.25) predicts that the theoretical drop in single-mode launch efficiency for these replays would be only 0.67dB, 1.10dB, 1.25dB and 1.51dB respectively, assuming the spots are Gaussian.

[†]Note that the diffraction-limits for the zero-orders have been omitted.

5.4 Discussion

The CODE V optical model and the experimental GRIN characterisation results verify that it is possible to make a single-mode crossbar using a diffractive 2DX320 device. Even with the large aperture and pixel size of this SLM, the design is compact and virtually aberration-free. Once constructed, the unique optical configuration will ensure that it will become one of the smallest and simplest transparent switches ever assembled.

The results indicate that GRIN lens collimators appear to have solved the problems of finding suitable fibre array and microlens technologies. The fibre-GRIN collimators that were designed and assembled are custom experimental components, and their performance can be expected to improve further as the manufacturing technique matures. The collimators have the advantage over traditional air-spaced lenses of being mechanically rigid and therefore less prone to vibrational problems. A method for assessing the GRIN collimation quality and estimating the profile constants at $\lambda = 1.55\mu\text{m}$ has been presented in this chapter. The next step in the physical construction of the crossbar is to mount the collimators in a full 2-dimensional array and demonstrate fibre-to-fibre switching by replacing the MicronViewer camera with the spherical interconnect mirror.

The use of active holographic splitters and combiners is a crucial conceptual step for implementing the crossbar as a single-mode structure. This means that there is a large initial insertion loss penalty compared with other competing switch technologies, but this loss is essentially fixed by the hologram and SLM efficiencies, being independent of the number of switch inputs. The FLC-SLM approach starts to look like an attractive option at a crossbar size of around 16×16 , where many of the non free-space technologies begin to hit cost, complexity and interconnectivity limits, and where blocking architectures such as OCPM start to exhibit very high insertion losses.

One problem that has not yet been addressed is the effect of the zero-order, symmetric-order and higher-order replay spots. The geometry of the optical interconnect is such that optical power in the second- and higher-orders is completely reflected out of the system aperture by the spherical interconnect mirror. But the zero-order, and the symmetric spot for some interconnect paths, can create unwanted cross-connections. The solution lies in a combination of: optimisation of the FLC switching angle to eliminate the zero-order using devices such as the 1DX320; finding a method of breaking the binary hologram replay symmetry; and finding a suitable geometry of the input and output fibres that avoids the

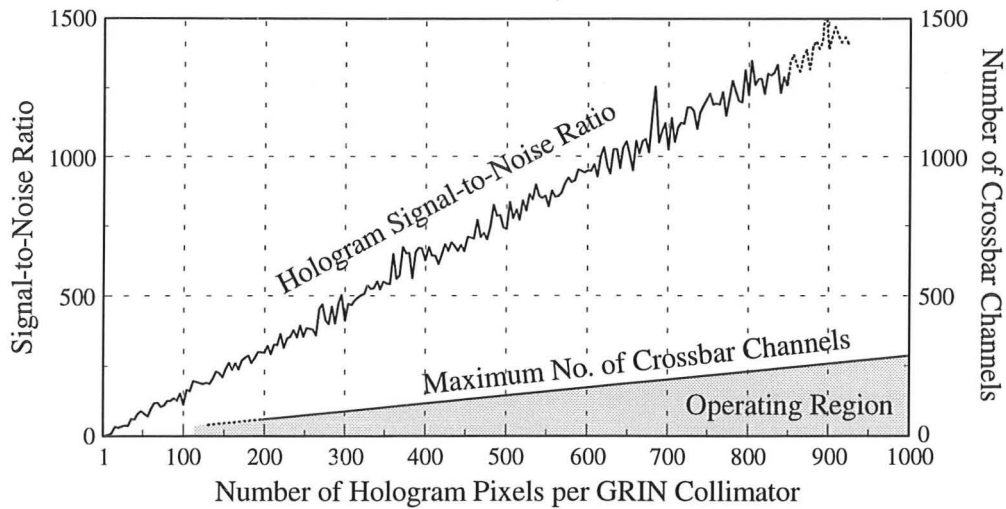


Figure 5.13: Required size of crossbar holograms.

unwanted connections. Of course if polarisation insensitivity is not required, then the SLM polarisers may be reintroduced to remove the zero-order.

A key scaling issue of holographic interconnects is the number of SLM pixels that are required to perform arbitrary switching. A simplistic argument predicts that in order to route any input to any one of M outputs, at least M pixels must be illuminated by each fibre-GRIN collimator, or $2M$ pixels if the binary hologram symmetry is also taken into account. Upon inclusion of the fan-in hologram pixels, a total of $4NM$ SLM pixels are therefore required. In practice, greater than this number of pixels will potentially provide improved signal-to-noise ratios, fewer pixels will lead to an increased level of crosstalk and bit-error-rate, rather than a catastrophic failure of the switch. The upper line in figure 5.13 demonstrates this point as the signal to mean noise power of an interconnect hologram designed with a fractional order replay coordinate of $\sigma = 0.3$. The trend of the curve is linearly increasing with space-bandwidth product of the hologram. It therefore shows that the performance of the crossbar can always be improved by introducing more routing pixels at the expense of greater SLM complexity. Failure of individual SLM pixels will similarly only cause the system to gradually slip back down to the left of the plot. A more rigorous analysis based on (u, v) coordinate permutations from equation (5.7), predicts that there should be $(2\sqrt{N} - 1)^2$ resolvable points in the replay plane to implement an N channel crossbar. This leads to a system total of $(4N^2 - 2N^{1.5} + 1)$ SLM pixels, which is marginally better than the simplistic argument. These expressions are plotted as the top of the shaded

region in figure 5.13.

The hologram frame set can again be designed to compensate for manufacturing tolerances as was demonstrated during the 1-to-15 experiment. As well as compensating for beam offsets (using the hologram splitters) and tilts (using the hologram combiners), the CGHs may be 'exclusive-OR' combined with Fresnel zone-like patterns [116] to counteract experimental differences in lateral positioning or focal length of the GRINs. The net optical effect of the splitting and combining holograms is theoretically almost insensitive to wavelength, and simulations of ideal optical components predict that the full-width at half-maximum channel response is of the order of $\Delta\lambda_{FWHM}=10-20\text{nm}$ for any input. In contrast to the passive fan-in crossbar, this reveals that there is virtually no wavelength dependence, making the crossbar well suited to high capacity, high data-rate applications. In some circumstances it may however be desirable to introduce wavelength dependence in order to create a combined space-wavelength router. This can most conveniently be achieved by incorporating the architectural principles from chapter 4, replacing the spherical interconnect mirror with a high-resolution concave grating for wavelength dispersion between the two FLC-SLM hologram planes.

Ultimately, the most important aspect of the design is to identify which factors limit the eventual realistic size of switch. The density and number of SLM pixels will inevitably be the final consideration, followed by manufacturing issues related to accurate assembly and alignment of the system. Mechanical stability can best be achieved by using miniature optical components and the use of a spherical interconnect mirror has introduced the exciting prospect of compressing the system into a small volume, potentially leading to highly parallel single-stage switches. Small spherically-curved mirrors are very easy to manufacture and align because of their inherent symmetry. A tilt misalignment of the spherical mirror can be easily corrected without the use of tilting positioning stages, by simply shifting the mirror up or down. The effect of small errors in the radius of mirror curvature may also be eliminated by adjusting the distance between the SLM and the bulk Fourier lens. The optical configuration might therefore enable the construction of dense optical switches that have a large enough aperture to simultaneously interconnect several FLC-over-silicon backplane SLMs, encompassing a huge number of interconnect pixels. From an entirely optical point of view, it is not inconceivable to design a system based around an array of 9 or even 16 SLMs, each with over 10^6 hologram pixels.

CHAPTER 6

Conclusions and Future Work

6.1 Conclusions

In the field of high-speed digital telecommunications, optical fibres dominate network transmission but optics is still seeking a role in switching. Free-space optical routing techniques offer several important advantages over purely electronic systems in terms of compactness, transparency, power dissipation and parallelism. The theme of this dissertation has been the investigation and experimental demonstration of new optical switching architectures that use ferroelectric liquid crystal spatial light modulators to diffract optical signals between single-mode fibres. The presented results of the laboratory proof-of-principle systems go a long way towards proving that FLC-SLM fibre switches can be used in certain high-bandwidth network applications. A key step towards enhancing their usefulness has been the demonstration that they may be used in non-polarisation controlled environments.

The results of the one-to-any switching experiments prove for the first time that FLC-SLMs can be used to route optical signals directly and efficiently between single-mode fibres. The polished fibre array used in the 1-to-15 experiment illustrates the demand for new and unusual optical components, but the experiment also vividly demonstrates the versatility of the FLC-SLM approach because the holographic patterns on the SLM can be tailored to compensate for component imperfections.

The crosstalk isolation performance of transmissive FLC-SLM fibre switches was shown to reach a coherent scatter noise limit at about -30dB. This figure seems to be fairly uniform across different SLMs and is probably determined by surface roughness on the pixel electrodes and by the contours of the FLC surface-stabilised alignment layers. The crosstalk performance of FLC-over-silicon devices is not yet known, but is unlikely to differ signifi-

cantly. Future FLC-SLM architectures will rely heavily on the more advanced technology provided by these silicon based SLMs.

Very large optical effects are required for efficient holographic beam steering, but are exhibited by relatively few FLC materials. The experimental replay created by the 1-dimensional SLM in chapter 4 is believed to have the highest diffraction efficiency of any previously operational SLM. The device achieves a first-order diffraction efficiency of 31% when alternate pixels are switched into opposite states. This is an excellent result when compared to the 40.6% theoretical maximum efficiency of perfect binary phase gratings.

The frame rate of the 1DX320 device is comparable with the fastest FLC-over-silicon modulators that have been fabricated to date. Unfortunately, the intrinsic switching speeds of high-tilt FLC materials are unlikely ever to operate faster than about 10-20 μ s. The type of switch structures presented in this dissertation are therefore unlikely to be directly useful for fast packet-switching unless a faster SLM technology can be devised that is capable of achieving binary phase modulation. The transparent FLC-SLM architectures are however well suited to the slower reconfiguration rates of circuit-switched broadband traffic or network load management. An important emerging subset of these applications is the use of wavelength routing techniques. The results of the tuneable wavelength filter show that it is straightforward to adjust the wavelength response of FLC-SLM switches and convert a broadband space-switch into a wavelength-switch by the addition of a high-resolution blazed linear grating. An active wavelength selective component is clearly more versatile than a passive demultiplexer, and FLC-SLMs exhibit an exceptionally simple and repeatable method of wavelength routing. The experimental demonstration of wavelength tuning achieved a channel separation of a few nanometres, but the generic system design is very flexible and could be redesigned to achieve a wide variety of filtered bandwidths, tuning steps and tuning ranges. Extrapolating the design principles demonstrated by the wavelength filter, it is an easy step to imagine exciting possibilities for future integrated space-wavelength switches.

Although the switches described in chapters 3 and 4 were based around bulk optics, more complex architectures must inevitably rely on arrays of micro-optics. The field of micro-lens manufacture is still in its infancy and the number of degrees of alignment freedom between planes of micro-components can be very high. The investigation of graded-index rod lens collimators in chapter 5 showed that GRIN lenses probably offer the best means for optical

interfacing between single-mode fibres and an SLM. The alignment process is simplified into a number of distinct steps and at least two air/glass boundaries are eliminated from the optical path. GRIN collimators were assembled as part of the design of a scalable, fully interconnected optical crossbar switch. A previously known crossbar configuration with passive fan-in was considered, but was rejected because of its $1/N$ insertion loss scaling and because of the \sqrt{N} growth of system length. An alternative single-mode architecture with active fan-in was suggested. This uses a spherical mirror to avoid both scaling limitations, potentially enabling the construction of highly parallel systems.

Building upon the experimental confirmation that FLC-SLMs can be used in the telecommunications wavelength band, an optical model of an 8x8 proof-of-design crossbar was constructed for $\lambda = 1.55\mu\text{m}$. This was based on real and obtainable components including commercially available 4mm diameter GRIN lenses, a standard catalog Fourier lens, and a passively-addressed transmissive FLC-SLM. Even with this non-custom design, the model predicts that it is relatively easy to achieve an optical performance that is limited only by the diffraction efficiency of the FLC holographic elements. The optical signals must pass through two binary CGHs and the theoretical minimum insertion loss is therefore of the order of between 8-12dB. This figure is fairly high, but it is independent of crossbar size. With 16 output fibres or more, the active fan-in architecture outperforms the passive crossbar in terms of insertion loss, and shuttering crossbars such as OCPM are outperformed almost immediately at 4 output fibres or more. The dilated nature of the active fan-in crossbar switch also means that its crosstalk isolation is potentially twice that of the one-to-any switch, i.e., possibly better than -60dB. The crosstalk analysis of coherent switch structures in [117] shows that this degree of isolation is more than sufficient to avoid problems of coherent beat noise between the crossbar input signals.

Although further work is required on system prototypes to demonstrate the full capability of holographic fibre switches, the initial experimental results are very encouraging and show that it is possible to create scalable, programmable, transparent optical interconnects. Future developments to optimise the performance of FLC-SLMs will hopefully lead to architectures of this type being implemented in fibre network systems and related applications.

6.2 Future Work

6.2.1 Devices

There is a considerable need to miniaturise the FLC-SLM switches presented in this dissertation into more compact and rugged structures, suitable for incorporation into actual networks. This can only be achieved by increasing the SLM pixel densities. FLC-over-silicon devices promise to achieve this reduction in scale, but present demand for these SLMs vastly outstrips availability, and transmissive SLMs such as the 2DX320 still have superior optical quality. A method of prototyping optical systems and evaluating new FLC materials would be very valuable, especially if the SLMs were optically compatible with future FLC-over-silicon SLM designs.

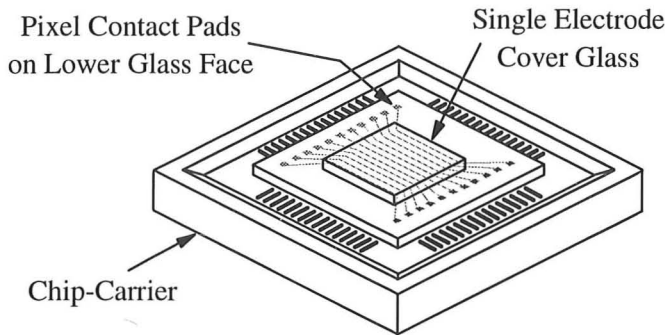


Figure 6.1: Prototyping design for silicon backplane compatible 1-D SLM structures.

Chapter 4 outlined the first application-oriented attempt to use a high-tilt material in a 1-dimensional SLM. This device is bulky and clumsy to use because of the flexible connectors that make electrical contact to the SLM pixels. Figure 6.1 shows a more sensible prototyping approach, designed so that the device can be mounted in a standard silicon chip-carrier. The lower glass SLM face is patterned with reflective metallic pixel stripes instead of ITO, and the pixels end in pads which may be directly wire-bonded to the chip-carrier pins. The whole device is similar in size to silicon SLMs and can sit in a zero-insertion-force socket on top of a printed circuit board. Current PGA chip-carrier packages would allow in excess of 250 SLM pixels, making the SLM suitable for small-scale fibre switching experiments. The pixel pitch is only limited by the photolithography process used to pattern the short metallic stripes, and is comparable with VLSI resolutions. The device manufacture is identical to the assembly of small glass cells and is therefore rapid. The main advantage over silicon

SLMs is that the device does not require circuit design iterations or optical planarisation. Simple generic driving electronics could enable interchangeability between different devices to meet application needs, and the SLM could be fabricated with gold pixel reflectors for very high $\lambda = 1.55\mu\text{m}$ performance.

6.2.2 Hologram asymmetry

The introduction of extra phase levels into the liquid crystal recording medium would improve the performance of all diffractive FLC switches, boosting the hologram efficiencies and removing the problems of replay symmetry. Figure 6.2 shows the change in theoretical first-order diffraction efficiency of a stepped phase grating as the number of phase levels is increased. FLC materials with more than two states are not unknown. Antiferroelectrics for example [118], exhibit a third ‘relaxed’ state in addition to the normal two fully switched states. This third state is obtained by removing the electric field from the pixel and allowing the molecular layers to fall back into their naturally alternating directions, figures 6.3(a)&(b). The alternating alignment generates a mean optical state, but it is achieved at the expense of a more complex tri-stable electronic drive scheme and a slightly slower response.

Unfortunately, no single birefringent FLC device with more than two phase levels can operate in a polarisation independent manner. To produce asymmetric replay fields, the incident light upon the SLM pixel array must be circularly polarised. The handedness of the polarisation determines whether the light is diffracted into the first-order spot or into its symmetry. Thus simple linearly polarised illumination can only ever result in completely symmetric replay fields. Even with circular polarisation, the symmetric order cannot be completely suppressed unless conditions are also met to completely suppress the zero-order. The optimum set of molecular tilt angles for P phase levels is given in degrees by:

$$\theta_q = \frac{180}{P} \left(q - \frac{P+1}{2} \right) \quad \text{where} \quad q = \{1, 2, 3, \dots P\} \quad (6.1)$$

Equation (6.1) implies that the 3-state antiferroelectric SLM must exhibit fully switched tilt angles of $\theta_{1,3} = \pm 60^\circ$ to achieve proper asymmetry. Clearly the $\pm 45^\circ$ optimum tilt angles for binary operation are difficult enough to achieve, and although a 30° material could be optically ‘doubled’ to 60° using clever optics [62], it is unlikely that a single ‘multi-phase’ device will be able to meet the conditions for true asymmetry.

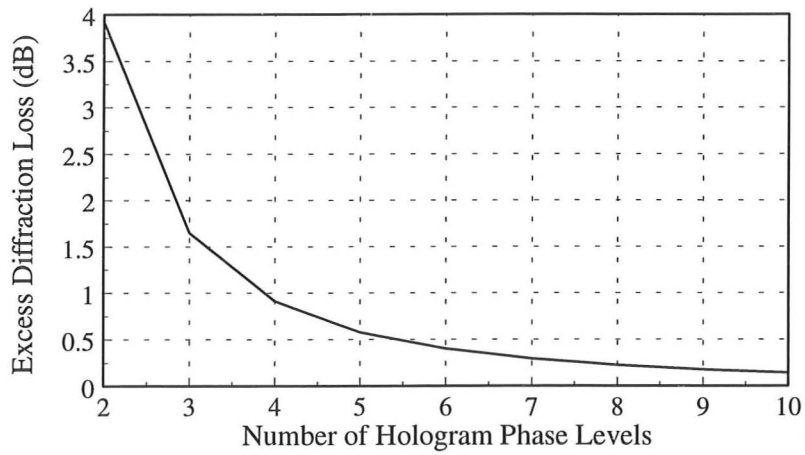


Figure 6.2: Typical holographic loss versus number of phase levels (no dead-space).

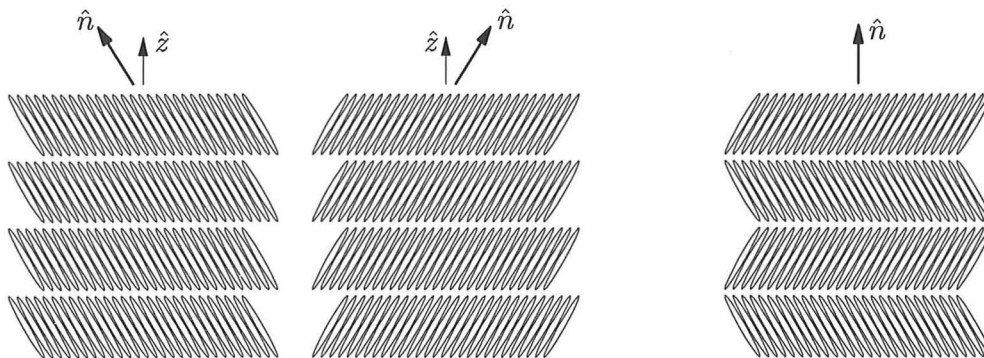


Figure 6.3(a): Normal ferroelectric molecular orientations: Binary states.

Figure 6.3(b): Relaxed antiferroelectric molecular orientation: Third state.

A second method of achieving asymmetric replay fields is to concatenate several binary FLC devices [39]. This technique has the disadvantage of considerably increasing the complexity and cost of the system. A better solution is to use a single binary FLC-SLM followed by a pseudo-random etched glass hologram [119]. The polarisation independent FLC layer effectively provides the dynamic $(0, \pi)$ binary modulation and the etched pattern provides a $(0, \frac{\pi}{2})$ fixed modulation. In isolation, the etched pattern is designed to produce a nearly uniform replay noise field, but in conjunction with the SLM, the FLC holograms contain enough spatial redundancy to produce a useful overall diffraction performance. The replays are genuinely asymmetric, but the combined hologram diffraction efficiencies are found to be little different from those of normal binary holograms. Light in the symmetric-order is therefore simply being suppressed to the level of the quantization noise background, rather than being transferred into the principal spot. This is not true multi-level phase modulation, but it achieves the desired asymmetry for use in diffractive switches [120] and has the advantage that the etch pattern can be written directly into the SLM glass face, hence eliminating some alignment problems.

6.2.3 *Systems*

By constructing the systems presented in this dissertation on an optical bench, it has become clear that more work is required to address the mechanical and thermal stability issues of free-space switches. The extent of the problem may be illustrated by considering that an output single-mode fibre launch efficiency falls by more than 15dB if the output is displaced by only $10\mu\text{m}$ (figure 3.13). This means that anyone bumping into or leaning on the optical bench may severely disrupt the optical signals passing through the switch.

AT&T Bell Laboratories solved many of their mechanical stability problems by designing a slotted metal baseplate with magnetic lens holders [12], but the design principles are still influenced by the need for traditional bulk lens mountings, and their baseplate is cumbersome and heavy. In some circumstances, GRIN lenses may offer a simpler solution by removing the need for machined parts, thereby reducing the system size, weight and complexity. Figure 6.4(a) shows a potential design for a compact tuneable wavelength filter. Air/glass interfaces have now been completely eliminated from the optical path. Thermal expansion is therefore less of a problem than in conventional air-spaced designs, and the whole device may be glued together in a mechanically stable structure using an optical-grade epoxy. The

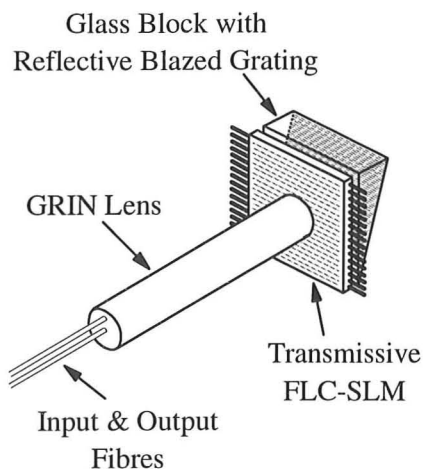


Figure 6.4(a): Compact tuneable wavelength filter using GRIN lenses.

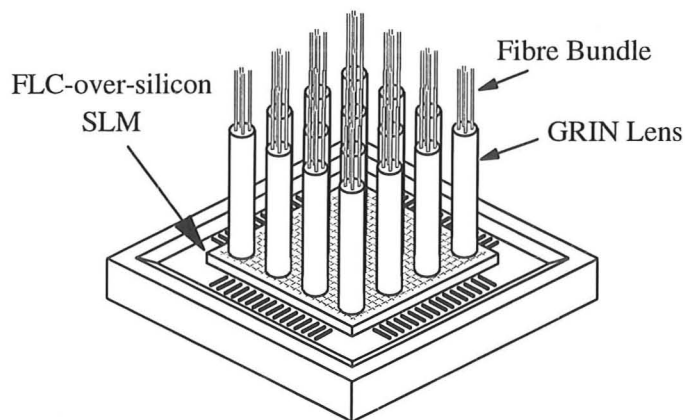


Figure 6.4(b): Compact dilated crossbar using GRIN lenses.

input and output fibres are glued to the end face of a polished GRIN rod which acts as the transfer lens for a $2-f$ wavelength filter. The other end of the GRIN is glued to the front glass of a transmissive 1-dimensional SLM. The rear face of this SLM can either be etched directly with the fixed dispersion grating, or it may be glued to a glass block or wedge that has been patterned with a blazed grating. It is worth noting that removal of the SLM converts the system back into a simple Littrow mount glass-block demultiplexer.

Figure 6.4(b) shows a similar design principle applied to a crossbar. Each GRIN is glued to a fibre bundle and to a reflective SLM. The GRINs therefore form an array of compact one-to-any switches, and a dilated crossbar structure may be created by appropriately splicing the fibres between GRINs using the interconnect pattern from figure 5.1. This crossbar design is particularly attractive because of its simplicity and robustness, and because there is no limit on the number of FLC-over-silicon SLM chips that may be used in the construction of the switch.

Although these GRIN mounting arrangements are yet to be fully tested, they are potentially much better suited to existing 19" rack technology than the large metallic baseplates. The GRIN optics can sit directly on top of printed circuit boards, and their exceptional compactness and modularity makes them ideal basic building blocks for the assembly of much larger space- and wavelength-switch architectures.

Bibliography

- [1] R.J. Mears, L. Reekie, I.M. Jauncey, and D.N. Payne. Low-noise Erbium-doped fiber amplifier operating at $1.54\mu\text{m}$. *Electronics Letters*, 23(19):1026–1028, 1987.
- [2] P. Trischitta, M. Colas, M. Green, G. Wuzniak, and J. Arena. The TAT-12/13 cable network. *IEEE Communications Magazine*, 34(2):24–28, 1996.
- [3] F. Mackenzie, T.G. Hodgkinson, S.A. Cassidy, and P. Healey. Optical interconnect based on a fibre bus. *Optical and Quantum Electronics*, 24(4):491–504, 1992.
- [4] L.R. McAdams, A.M. Gerrish, R.F. Kalman, and J.W. Goodman. Optical crossbar switch with semiconductor optical amplifiers. In *Spatial Light Modulators and Applications*, Palm Springs, March 1993. Optical Society of America.
- [5] A. Matoba, H. Okayama, R. Shibuya, and T. Ishida. Low-drive-voltage 8×8 Ti : LiNbO₃ switch with simplified tree structure. *Electronics Letters*, 25(2):165–166, 1989.
- [6] P. Granstrand, B. Larserström, P. Svensson, H. Olofsson, J.E. Falk, and B. Stoltz. Pigtailed tree-structured 8×8 LiNbO₃ switch matrix with 112 digital optical switches. *IEEE Photonics Technology Letters*, 6(1):71–73, 1994.
- [7] K. Hamamoto, T. Anan, K. Komatsu, M. Sugimoto, and I. Mito. First 8×8 semiconductor optical matrix switches using GaAs/AlGaAs electro-optic guided-wave directional couplers. *Electronics Letters*, 28(5):441–443, 1992.
- [8] K.R. Oh, K.S. Park, D.K. Oh, H.M. Kim, H.M. Park, and K. Lee. A very low operation current InGaAsP/InP total internal reflection optical switch using p/n/p/n current blocking layers. *IEEE Photonics Technology Letters*, 6(1):65–67, 1994.

- [9] K.W. Cheung, D.A. Smith, J.E. Baran, and B.L. Heffner. Multiple channel operation of integrated acousto-optic tunable filter. *Electronics Letters*, 25(6):375–376, 1989.
- [10] P.A. Andrekson, N.A. Olsson, J.R. Simpson, D.J. Digiovanni, P.A. Morton, T. Tanbun-Ek, R.A. Logan, and K.W. Wecht. 64Gb/s all-optical demultiplexing with the nonlinear optical-loop mirror. *IEEE Photonics Technology Letters*, 4(6):644–647, 1992.
- [11] D.A.B. Miller, M.D. Freuer, T.Y. Chang, S.C. Shunk, J.E. Henry, D.J. Burrows, and D.S. Chemla. Field-effect transistor self-electrooptic effect device: Integrated photodiode, quantum well modulator and transistor. *IEEE Photonics Technology Letters*, 1(3):62–64, 1989.
- [12] F.B. McCormick, T.J. Cloonan, A.L. Lentine, J.M. Sasian, R.L. Morrison, M.G. Beckman, S.L. Walker, M.J. Wojcik, S.J. Hinterlong, R.J. Crisci, R.A. Novotny, and H.S. Hinton. Five-stage free-space optical switching network with field-effect transistor self-electro-optic-effect-device smart-pixel arrays. *Applied Optics*, 33(8):1601–1618, 1994.
- [13] D.C. Griffiths and K.R. Preston. Space and wavelength filter for use in WDM-based optical switching networks. *Electronics Letters*, 28(18):1729–1730, 1992.
- [14] H. Yamazaki, M. Yamaguchi, and K. Hirabayashi. Estimation of the possible scale for holographic switches with liquid-crystal displays. *Applied Optics*, 34(8):1333–1340, 1995.
- [15] N. Collings, W.A. Crossland, P.J. Ayliffe, D.G. Vass, and I. Underwood. Evolutionary development of advanced liquid crystal spatial light modulators. *Applied Optics*, 28(22):4740–4747, 1989.
- [16] R.M. Turner, D.A. Jared, G.D. Sharp, and K.M. Johnson. Optical correlation using very-large-scale integrated circuit / ferroelectric-liquid-crystal electrically addressed spatial light modulators. *Applied Optics*, 32(17):3094–3101, 1993.
- [17] D.C. Burns, I. Underwood, A. O'Hara, and D.G. Vass. Electronically addressed ferroelectric liquid crystal over silicon spatial light modulators. In *Optical Computing '94*, Edinburgh, UK, 1994.

- [18] D.C. O'Brien, T.D. Wilkinson, and R.J. Mears. Programmable computer generated holograms with large space bandwidth product. In *Proc. IEE, Holographic Systems Components and Applications*, Neuchatel, Switzerland, 1993.
- [19] F.T.S. Yu. *White-Light Optical Signal Processing*. Wiley series in pure and applied optics, 1985.
- [20] J.L. Horner and J. Leger. Pattern recognition with binary phase-only filters. *Applied Optics*, 24:609–611, 1985.
- [21] T.D. Wilkinson, D.C. O'Brien, and R.J. Mears. Scale invariant binary phase-only matched filter using a ferroelectric liquid crystal spatial light modulator. *Applied Optics*, 33:4452–4453, 1993.
- [22] J.N. Mait and G.S. Himes. Computer-generated holograms by means of a magneto-optic spatial light-modulator. *Applied Optics*, 28(22):4879–4887, 1989.
- [23] D.W. Prather and J.N. Mait. Acousto-optic generation of two-dimensional spot arrays. *Optics Letters*, 16(22):1720–1722, 1991.
- [24] D.O. Harris and A. VanderLugt. Multichannel acousto-optic crossbar with arbitrary signal fan-out. *Applied Optics*, 31(11):1684–1686, 1992.
- [25] W.E. Ross, D. Psaltis, and R.H. Anderson. Two-dimensional magneto-optic spatial light modulator for signal processing. *Optical Engineering*, 22(4):485–490, 1983.
- [26] J.A. Davies, S.W. Connely, G.W. Bach, R.A. Lilly, and D.M. Cottrell. Programmable optical interconnections with large fan-out capability using the magneto-optic spatial light modulator. *Optics Letters*, 14(1):102–104, 1989.
- [27] D.A. Gregory, R.D. Juday, J. Sampsell, R. Gale, R.W. Cohn, and S.E. Monroe, Jr. Optical characteristics of a deformable-mirror spatial light modulator. *Optics Letters*, 13(1):10–12, 1988.
- [28] D.R. Collins, J.B. Sampsell, L.J. Hornbeck, J.M. Florence, P.A. Penz, and M.T. Gately. Deformable mirror device spatial light modulators and their applicability to optical neural networks. *Applied Optics*, 28(22):4900–4907, 1989.
- [29] F. Mok, J. Diep, H.K. Liu, and D. Psaltis. Real-time computer-generated hologram by means of liquid-crystal television spatial light modulator. *Optics Letters*, 11(11):748–750, 1986.

- [30] M.F. Bone, D. Coates, W.A. Crossland, P. Gunn, and P.W. Ross. Ferroelectric liquid crystal display capable of video line address times. *Displays*, pages 115–118, July 1989.
- [31] J.W. Goodman. *Introduction to Fourier Optics*. McGraw-Hill, 1968.
- [32] A.E. Siegman. *Lasers*, chapter 16-17. Oxford University Press, 1986.
- [33] A.W. Snyder and J.D. Love. *Optical Waveguide Theory*. Chapman and Hall, London, 1983.
- [34] D. Marcuse. Loss analysis of single-mode fiber splices. *Bell System Technical Journal*, 56(5):703–718, 1977.
- [35] M.J. Holmes. *Design of non-linear optical fibres*. PhD thesis, Cambridge University, 1992.
- [36] R.N. Bracewell. *The Fourier Transform and its applications*, chapter 18. McGraw-Hill, 1978.
- [37] S.T. Lagerwall, N.A. Clark, J. Dijon, and J.F. Clerc. Ferroelectric liquid crystals: The development of devices. *Ferroelectrics*, 94:3–62, 1989.
- [38] D.C. O'Brien, W.A. Crossland, and R.J. Mears. A holographically routed optical crossbar: theory and simulation. *Optical Computing and Processing*, 1(3):223–243, 1991.
- [39] S.E. Broomfield, M.A.A. Neil, E.G.S. Paige, and G.G. Yang. Programmable binary phase-only optical-device based on ferroelectric liquid-crystal SLM. *Electronics Letters*, 28(1):26–28, 1992.
- [40] M.J. O'Callaghan and M.A. Handschy. Diffractive ferroelectric liquid crystal shutters for unpolarized light. *Optics Letters*, 16(10):770–772, 1991.
- [41] H. Hamam and J.L. de Bougrenet de la Tocnaye. Fractional Talbot four-level phase-only holograms using ferroelectric liquid-crystal spatial light modulators. *Optics Letters*, 19(20):1654–1656, 1994.
- [42] H. Ichikawa, T.H. Barnes, M.R. Taghizadeh, J. Turunen, T. Eiju, and K. Matsuda. Dynamic space-variant optical interconnections using liquid-crystal spatial light modulators. *Optics Communications*, 93(3-4):145–150, 1992.

- [43] D.C. O'Brien, R.J. Mears, and W.A. Crossland. Optical crossbar switching using dynamic holograms written to ferroelectric liquid crystal spatial light modulators. In *IEE Colloquium on Optical Switching*, June 3, 1993.
- [44] S.T. Warr, M.C. Parker, and R.J. Mears. Optically transparent digitally tunable wavelength filter. *Electronics Letters*, 31(2):129–130, 1995.
- [45] T.D. Wilkinson, , D.C. O'Brien, and R.J. Mears. Scale invariant binary phase-only matched filter using a ferroelectric liquid crystal spatial light modulator. *Applied Optics*, 33(20):4452–4453, 1994.
- [46] N.A. Clark and S.T. Lagerwall. Submicrosecond bistable electro-optic switching in liquid crystals. *Applied Physics Letters*, 36(11):899–901, 1980.
- [47] Y. Sato, T. Tanaka, H. Kobayashi, K. Aoki, H. Watanabe, H. Takeshita, Y. Ouchi, H. Takezoe, and A. Fukuda. High quality ferroelectric liquid crystal display with quasi bookshelf layer structure. *Japanese Journal of Applied Physics*, 28(3):483–486, 1989.
- [48] J. Kanbe, H. Inoue, A. Mizutome, Y. Hanyuu, K. Katagiri, and S. Yoshihara. High resolution, large area FLC display with high graphic performance. *Ferroelectrics*, 114:3–26, 1991.
- [49] A. O'Hara, J.R. Hannah, I. Underwood, D.G. Vass, and R.J. Holwill. Mirror quality and efficiency improvements of reflective spatial light modulators by the use of dielectric coatings and chemical-mechanical polishing. *Applied Optics*, 32(28):5549–5556, 1993.
- [50] I. Underwood, D.G. Vass, M.W.G. Snook, W.J. Hossack, L.B. Chua, J.R. Brocklehurst, M.J. Birch, W.A. Crossland, R.J. Mears, T.C.B. Yu, M.R. Worboys, S. Radcliffe, and N. Collings. Smart pixels using liquid-crystal-over-silicon. In *IEEE/LEOS Topical Meeting on Smart Pixels*, Lake Tahoe, Nevada, July 11, 1994.
- [51] R.A. Gabel and B. Liu. Minimization of reconstruction errors with computer generated binary holograms. *Applied Optics*, 9(5):1180–1191, 1970.
- [52] R.W. Gerchberg and W.O. Saxon. A practical algorithm for the determination of phase from image and diffraction plane pictures. *Optik*, 35(2):237–246, 1972.
- [53] J.R. Fienup. Iterative method applied to image reconstruction and to computer-generated holograms. *Optical Engineering*, 19(3):297–305, 1980.

- [54] M.A. Seldowitz, J.P. Allebach, and D.W. Sweeney. Synthesis of digital holograms by direct binary search. *Applied Optics*, 26(14):2788–2798, 1987.
- [55] M.R. Feldman and C.C. Guest. Iterative encoding of high-efficiency holograms for generation of spot arrays. *Optics Letters*, 14(10):479–481, 1989.
- [56] S. Weissbach, F. Wyrowski, and O. Bryngdahl. Digital phase holograms: Coding and quantization with an error diffusion concept. *Optics Communications*, 72(1):37–41, 1989.
- [57] Z. Bahri and B.V.k. Vijaya Kumar. Fast algorithms for designing optical phase-only filters (POFs) and binary phase-only filters (BPOFs). *Applied Optics*, 29(20):2992–2996, 1990.
- [58] M.P. Dames, R.J. Dowling, P. McKee, and D. Wood. Efficient optical elements to generate intensity weighted spot arrays: design and fabrication. *Applied Optics*, 30(19):2685–2691, 1991.
- [59] E. Merck, Postfach 41 19, D-6100 Darmstadt 1, Germany. *Ferroelectric Smectic Mixtures*.
- [60] Chisso Corporation, 7-3 Marunouchi 2-Chome, Chiyoda-Ku, Tokyo, Japan. *Ferroelectric Smectic Mixtures*.
- [61] J. Newton, H. Coles, H. Owen, and T. Hodge. A new series of low molar organosiloxanes with unusual electro-optic properties. *Ferroelectrics*, 148:379–387, 1993.
- [62] M.A.A. Neil and E.G.S. Paige. Improved transmission in a two-level phase-only, spatial light modulator. *Electronics Letters*, 30(5):445–446, 1994.
- [63] S.T. Warr and R.J. Mears. Polarisation insensitive operation of ferroelectric liquid crystal devices. *Electronics Letters*, 31(9):714–716, 1995.
- [64] S.T. Warr and R.J. Mears. Polarisation insensitive diffractive FLC systems. Accepted for *Ferroelectrics*, 1995.
- [65] E. Hecht. *Optics*, pages 321–326. Addison-Wesley, 1987.
- [66] A.P. Sparks, R.C. Chittick, W.A. Crossland, and J.R. Brocklehurst. A 128 x 128 matrix electrically addressed ferroelectric liquid crystal spatial light modulator. In *IEE Tech. Digest 1988/121*, 1988.

- [67] N.C. Roberts, A.G. Kirk, and T.J. Hall. Binary phase gratings for hexagonal array generation. *Optics Communications*, 94(6):501–505, 1992.
- [68] G.M. Proudley, C. Stace, and H. White. Fabrication of 2-D fibre-optic arrays for an optical crossbar switch. *Optical Engineering*, 33(2):627–635, 1994.
- [69] RS Components Ltd. *Electronic and Electrical components: Data sheet no. 842-472*.
- [70] M.J. Holmes, F.P. Payne, P. Dainty, T.J. Hall, and W.A. Crossland. Low crosstalk devices for wavelength-routed networks. In *IEE Colloquium on Guided Wave Optical Signal Processing*, June 8, 1995.
- [71] F.M. Dickey and B.D. Hansche. Quad-phase correlation filters for pattern recognition. *Applied Optics*, 28(9):1611–1613, 1989.
- [72] S.E. Broomfield, M.A.A. Neil, and E.G.S. Paige. A 4-level, phase-only, spatial light modulator. *Electronics Letters*, 29(18):1661–1663, 1993.
- [73] M.A. Neil and E.G.S. Paige. Breaking of inversion symmetry in 2-level, binary, Fourier holograms. In *Proc. IEE, Holographic Systems Components and Applications*, Neuchatel, Switzerland, 1993.
- [74] H. Dammann. Blazed synthetic phase-only holograms. *Optik*, 31(1):95–104, 1970.
- [75] P.J. Smith, D.W. Faulkner, and G.R. Hill. Evolution scenarios for optical telecommunication networks using multiwavelength transmission. *Proceedings of the IEEE*, 81(11):1580–1587, 1993.
- [76] I.C. Khoo. *Liquid Crystals: Physical Properties and Nonlinear Optical Phenomena*, page 5. John Wiley & Sons, New York, 1995.
- [77] J.E. Midwinter, editor. *Photonics in Switching II*, chapter 1: Multiwavelength switching and interconnection networks. Academic Press, 1993.
- [78] E.E. Basch, editor. *Optical-Fiber Transmission*, pages 250–251. Macmillan, 1987.
- [79] H.J. Masterson, G.D. Sharp, and K.M. Johnson. Ferroelectric liquid-crystal tunable filter. *Optics Letters*, 14(22):1249–1251, 1989.
- [80] J. Stone and L.W. Stulz. FiEnd filters: passive multilayer thin-film optical filters deposited on fibre ends. *Electronics Letters*, 26(16):1290–1291, 1990.

- [81] J. Frangen, H. Herrmann, R. Ricken, H. Seibert, and W. Sohler. Integrated optical, acoustically tunable wavelength filter. *Electronics Letters*, 25(23):1583–1584, 1989.
- [82] T.L. Koch, F.S. Choa, F. Heismann, and U. Koren. Tunable multiple-quantum well distributed-Bragg reflector lasers as tunable narrowband receivers. *Electronics Letters*, 25(14):890–892, 1989.
- [83] M.C. Parker. *Dynamic Holograms for WDM*. PhD thesis, Cambridge University. To be submitted.
- [84] Optical Research Associates. *The CODE V reference manual*, 1990.
- [85] W.J. Smith. *Modern Lens Design: A resource manual*. McGraw-Hill, 1992.
- [86] M.C. Parker, S.T. Warr, and R.J. Mears. Tunable holographic wavelength filter. In *OSA Topical Meeting on Spatial Light Modulators and Applications*, Salt Lake City, Utah, March 12, 1995.
- [87] E.K. Murthy. Laser scanning lens configurations. *Proc. SPIE*, 1333:145–158, 1990.
- [88] B. Brixner and M.M. Klein. Optimization to create a four-element laser scan lens from a five-element design. *Optical Engineering*, 31(6):1257–1258, 1992.
- [89] A.A. Sawchuk, B.K. Jenkins, C.S. Raghavendra, and A. Varma. Optical crossbar networks. *Computer*, 20(6):50–60, 1987.
- [90] A.R. Dias, R.F. Kalman, J.W. Goodman, and A.A. Sawchuk. Fiber-optic crossbar switch with broadcast capability. *Optical Engineering*, 27(11):955–960, 1988.
- [91] H.S. Hinton. Photonic switching using directional couplers. *IEEE Communications Magazine*, 25(5):16–26, 1987.
- [92] JDS Fitel Inc., Ontario, Canada. *SG Series M × N Singlemode Matrix Switch*.
- [93] J.W. Goodman, A.R. Dias, and L.M. Woody. Fully parallel, high-speed incoherent optical method for performing discrete Fourier transforms. *Optics Letters*, 2(1):1–3, 1978.
- [94] H.J. White, G.M. Proudley, C. Stace, N.A. Brownjohn, A.C. Walker, M.R. Taghizadeh, B.R. Robertson, C.P. Barrett, W.A. Crossland, J.R. Brocklehurst, M.J. Birch, M. Snook, and D. Vass. Development of an optical free-space crossbar. In *Institute of Physics Conference Series No. 139: Part II*, pages 183–186, 1994.

- [95] D.C. O'Brien, R.J. Mears, T.D. Wilkinson, and W.A. Crossland. Dynamic holographic interconnects that use ferroelectric liquid-crystal spatial light modulators. *Applied Optics*, 33(14):2795–2803, 1994.
- [96] B. Robertson, E.J. Restall, M.R. Taghizadeh, and A.C. Walker. Space-variant holographic optical elements in dichromated gelatin. *Applied Optics*, 17(30):2368–2375, 1991.
- [97] F. Sauer, N. Craft, J. Avins, M. LaValva, and J. Turlip. Multistage sorting module with VCSEL based free-space optical interconnects. In *IEEE/LEOS Topical Meeting on Smart Pixels*, Lake Tahoe, Nevada, July 11, 1994.
- [98] S.M. Shank, F.T. Chen, M. Skvarla and H.G. Craighead, P.Cook, R. Bussjager, F. Haas, and D.A. Honey. Multiple-level phase gratings fabricated using focused ion-beam milling and electron-beam lithography. *Journal of Vacuum Science and Technology B*, 12(6):3643–3647, 1994.
- [99] D. Daly, R.F. Stevens, M.C. Hutley, and N. Davies. The manufacture of microlenses by melting photoresist. *Measurement Science and Technology*, 1(8):759–766, 1990.
- [100] D.C. O'Brien and D.J. McKnight. A compact holographically routed optical crossbar using a ferroelectric liquid-crystal over silicon spatial light modulator. In *Optical Computing '94*, Edinburgh, UK, August 22, 1994.
- [101] H. Karstensen and K. Drögemüller. Loss analysis of laser diode to single-mode fiber couplers with glass spheres or silicon plano-convex lenses. *Journal of Lightwave Technology*, 8(5):739–747, 1990.
- [102] Y. Lu, J.C. Palais, and Y. Chen. Coupling efficiency of single-mode fiber components using GRIN-rod lenses. *Fiber and Integrated Optics*, 7(2):85–107, 1988.
- [103] I. Kitano, H. Ueno, and M. Toyama. Gradient-index lens for low-loss coupling of a laser diode to single-mode fiber. *Applied Optics*, 25(19):3336–3339, 1986.
- [104] Y. Makita, I. Yamauchi, and K. Sono. GRIN lenses for high efficiency coupling of laser diodes to single mode fiber. *Fiber and Integrated Optics*, 7(1):27–33, 1988.
- [105] T. Sakamoto. Coupling characteristic analysis of single-mode and multimode optical-fiber connectors using gradient-index-rod lenses. *Applied Optics*, 31(25):5184–5190, 1992.

- [106] M.S. Sodha and A.K. Ghatak. *Inhomogeneous Optical Waveguides*, chapter 5. Plenum Press, New York, 1977.
- [107] R. Falciai and T. Pascucci. Geometrical model for the design of gradient-index-rod lens coupling devices. *Applied Optics*, 31(25):5211–5215, 1992.
- [108] NSG Europe, Belgium. *SELFOC Product Guide*.
- [109] Gradient Lens Corporation, New York. *BIG GRINS: Large Diameter GRIN Rod Lenses*.
- [110] Meteor Optics, Inc., 4710 Juneau Lane N. Plymouth, MN 55446, USA.
- [111] Spindler & Hoyer. *Optics/Mechanics*. Pigtailed Gradient-Index Lens Collimators.
- [112] P.L. Chu and T. Whitbread. Measurement of refractive-index profile of optical-fibre preform. *Electronics Letters*, 15(10):295–296, 1979.
- [113] I. Sasaki, D.N. Payne, and M.J. Adams. Measurement of refractive-index profiles in optical-fibre preforms by spatial-filtering technique. *Electronics Letters*, 16(6):219–221, 1980.
- [114] W.J. Stewart. Optical fiber and preform profiling technology. *IEEE Journal of Quantum Electronics*, 18(10):1451–1466, 1982.
- [115] The MathWorks, Inc. *MATLAB: High-Performance Numeric Computation and Visualization Software*, 1993.
- [116] S.E. Broomfield, M.A.A. Neil, E.G.S. Paige, R.H. Scarbrough, and G.G. Yang. Programmable diffractive optics with a ferroelectric liquid crystal SLM in a binary phase-only mode. *Proc. SPIE*, 1732:287, 1992.
- [117] D.J. Blumenthal, P. Granstrand, and L. Thylen. A comparison of coherent crosstalk induced BER floors in four types of $N \times N$ space photonic switches. In *Proc. Third International Conference on Holographic Systems, Components and Applications*, Salt Lake City, Utah, March 15, 1995. OSA.
- [118] H. Takezoe, A. Fukuda, A. Ikeda, Y. Takanishi, T. Umemoto, J. Watanabe, H. Iwane, M. Hara, and K. Itoh. On the appearance of the antiferroelectric phase. *Ferroelectrics*, 122:167–176, 1991.

- [119] T.D. Wilkinson, D.C. O'Brien, and R.J. Mears. Dynamic asymmetric binary holograms using a ferroelectric liquid crystal spatial light modulator. *Optics Communications*, 109:222–226, 1994.
- [120] T.D. Wilkinson, S.T. Warr, and R.J. Mears. Holographic crossbar switch using asymmetric binary holograms. In *IEEE/LEOS Topical Meeting on Smart Pixels*, Lake Tahoe, Nevada, July 11, 1994.

APPENDIX A

Associated Publications

Papers:

T.D. Wilkinson, W.A. Crossland, S.T. Warr, T.C.B. Yu, A.B. Davey, and R.J. Mears. "New applications for ferroelectric liquid crystals." *Liquid Crystals Today*, 4(3), 1994.

S.T. Warr, M.C. Parker, and R.J. Mears. "Optically transparent digitally tunable wavelength filter." *Electronics Letters*, 31(2):129-130, 1995.

S.T. Warr and R.J. Mears. "Polarisation insensitive operation of ferroelectric liquid crystal devices." *Electronics Letters*, 31(9):714-716, 1995.

S.T. Warr and R.J. Mears. "Polarisation insensitive diffractive FLC systems." Accepted for *Ferroelectrics*, 1995.

Conferences:

T.D. Wilkinson, S.T. Warr, and R.J. Mears. "Holographic crossbar switch using asymmetric binary holograms." In *IEEE/LEOS Topical Meeting on Smart Pixels*, Lake Tahoe, Nevada, July 11, 1994.

W.A. Crossland, S.T. Warr, R.J. Mears, and R.W.A. Scarr. "Spatial-light-modulator based routing switches." In *Optical Computing '94*, Edinburgh, UK, August 22, 1994.

W.A. Crossland, S.T. Warr, R.J. Mears, and R.W.A. Scarr. "Spatial light modulator based routing switches." In *CLEO*, Amsterdam, August 1994.

M.C. Parker, S.T. Warr, and R.J. Mears. "Tunable holographic wavelength filter." In *OSA Topical Meeting on Spatial Light Modulators and Applications*, Salt Lake City, Utah, March 12, 1995.

S.T. Warr and R.J. Mears. "Polarisation insensitive one-to-any single-mode fibre switch." In *FLC '95*, Cambridge, UK, July 23, 1995.

R.J. Mears, S.T. Warr, M.C. Parker, T.D. Wilkinson, W.A. Crossland, and A.B. Davey. "Polarisation insensitive ferroelectric liquid crystal devices." In *FLC '95*, Cambridge, UK, July 23, 1995.

APPENDIX B

Glossary

AC	Alternating current,	WDM	Wavelength division multiplex,
AM	Amplitude modulation,	VLSI	Very large scale integration.
CCD	Charge coupled device,		
CGH	Computer generated hologram,		
CIF	Caltech information format,		
CMOS	Complementary metal-oxide-silicon,		
CTF	Coherent transfer function,		
dB	Decibels,		
DC	Direct current,		
DRAM	Dynamic random access memory,		
EASLM	Electrically addressed spatial light modulator,		
FET	Field effect transistor,		
FFT	Fast Fourier transform,		
FLC	Ferroelectric liquid crystal,		
FM	Frequency modulation,		
FWHM	Full-width at half-maximum,		
GRIN	Graded-index lens,		
ITO	Indium tin oxide,		
LC	Liquid crystal,		
LED	Light emitting diode,		
PSF	Point-spread function,		
RAM	Random access memory,		
SEED	Self electro-optic device,		
SLM	Spatial light modulator,		
SNR	Signal-to-noise ratio,		
SRAM	Static random access memory,		
TEM	Transverse electromagnetic,		

CAMBRIDGE
UNIVERSITY LIBRARY

Attention is drawn to the fact that the copyright of this dissertation rests with its author.

This copy of the dissertation has been supplied on condition that anyone who consults it is understood to recognise that its copyright rests with its author. In accordance with the Law of Copyright no information derived from the dissertation or quotation from it may be published without full acknowledgement of the source being made nor any substantial extract from the dissertation published without the author's written consent.